UNIVERSITY OF CALIFORNIA, SAN DIEGO

A study of the Southern Ocean: Mean state, eddy genesis & demise, and energy pathways

A dissertation submitted in partial satisfaction of the
requirements for the degree
Doctor of Philosophy

in

Oceanography

by

Uriel Zajaczkovski

Committee in charge:

Sarah T. Gille, Chair
Teresa K. Chereskin
Jennifer A. MacKinnon
Matthew R. Mazloff
Keiko Nomura
Dean Roemmich

2017

The dissertation of Uriel Zajaczkovski is approved, and it is acceptable in quality and form for publication on microfilm and electronically:

_____

_____

_____

_____

_____

_____
Chair

University of California, San Diego

2017

TABLE OF CONTENTS

LIST OF FIGURES

LIST OF TABLES

ACKNOWLEDGEMENTS

I would like to acknowledge my advisor Sarah T. Gille. Thank you for your guidance throughout all these years. Your advice on both research as well as on my career have been invaluable. It was truly a pleasure to be your mentee.

I would like to thank my thesis committee: Dr. Matthew Mazloff, Prof. Jennifer MacKinnon, Dr. Teresa Chereskin, Prof. Dean Roemmich and Prof. Keiko Nomura, your insightful comments and questions made this a better PhD thesis.

I would like to thanks Myrl Hendershott, Clint Winant, Bill Young, Rob Pinkel, Glenn Ierley, Rick Salmon and Peter Franks. You were a constant source of inspiration during all these years.

I would like to thank my cohort: Andrew Delman, Bonnie Ludka, Caitlin Whalen, Kai Hally-Rosendahl, Magdalena Carranza, Nick Pizzo, Roy Barkan, Ruth Musgrave and Sam Billheimer. I was lucky to be part of such a wonderful group. Late nights discussing homework and countless hiking and camping trips are memories I will treasure for life.

And finally I would like to thank my wife, Ruth. Your constant encouragement and support was vital during all these years.

Chapter 3 is currently being prepared for submission for publication of the material to Geophysical Research Letters. Zajaczkovski, U.; Gille, Sarah T.; Mazloff, Matthew R. The dissertation author was the primary investigator and author of this paper.

Chapter 4, in full, has been submitted for publication of the material as it may appear in Journal of Physical Oceanography, 2017. Zajaczkovski, U.; Gille, Sarah T.; Mazloff, Matthew R. The dissertation author was the primary investigator and author of this paper.

VITA

2009	Licenciatura en Oceanografia Fisica, Universidad de Buenos Aires, Buenos Aires, Argentina
2011	M.Sc. in Oceanography, University of California, San Diego
2017	Ph.D. in Oceanography, University of California, San Diego

PUBLICATIONS

Zajaczkovski, U., S.T. Gille and M.R. Mazloff. On eddy generation and decay in the Southern Ocean. To be submitted to J. Phys. Oceanogr.

Zajaczkovski, U., S.T. Gille and M.R. Mazloff. Downgradient heat transport in the ACC due to reverse meridional eddy migration. To be submitted to Geophys. Res. Lett.

Zajaczkovski, U. and S.T. Gille. Four-dimensional structure of the Southern Ocean: Impact of eddies and frontal displacements on the background fields. Manuscript in prep.

Saraceno, M., C. Provost and **U. Zajaczkovski**, 2009. Long-term variation in the anticyclonic ocean circulation over the Zapiola Rise as observed by satellite altimetry: Evidence of possible collapses. Deep Sea Research Part I: Oceanographic Research Papers, Volume 56, Issue 7, July 2009, Pages 1077-1092.

Piola, A.R., S.I. Romero and **U. Zajaczkovski**, 2008. Space-time variability of the Plata plume inferred from ocean color. Continental Shelf Research, Volume 28, Issue 13, 30 July 2008, Pages 1556-1567.

Campagna, C., A.R. Piola, M.R. Marin, M. Lewis., **U. Zajaczkovski** and T. Fernndez, 2007. Deep divers in shallow seas: southern elephant seals on the Patagonian shelf. Deep-Sea Research I 54, 1792-1814.

ABSTRACT OF THE DISSERTATION

A study of the Southern Ocean: Mean state, eddy genesis & demise, and energy pathways

by

Uriel Zajaczkovski

Doctor of Philosophy in Oceanography

University of California, San Diego, 2017

Sarah T. Gille, Chair

The Southern Ocean (SO), due to its deep penetrating jets and eddies, is well-suited for studies that combine surface and sub-surface data. This thesis explores the use of Argo profiles and sea surface height (SSH) altimeter data from a statistical point of view. A linear regression analysis of SSH and hydrographic data reveals that the altimeter can explain, on average, about 35% of the variance contained in the hydrographic fields and more than 95% if estimated locally. Correlation maxima are found at mid-depth, where dynamics are dominated by geostrophy. Near the surface, diabatic processes are significant, and the variance explained by the altimeter is lower. Since SSH variability is associated with eddies, the regression of SSH with temperature (T) and salinity (S) shows the relative

importance of S vs T in controlling density anomalies. The Antarctic Intermediate Water (AAIW) salinity minimum separates two distinct regions; above the minimum density changes are dominated by T, while below the minimum S dominates over T. The regression analysis provides a method to remove eddy variability, effectively reducing the variance of the hydrographic fields.

We use satellite altimetry and output from an assimilating numerical model to show that the SO has two distinct eddy motion regimes. North and south of the Antarctic Circumpolar Current (ACC), eddies propagate westward with a mean meridional drift directed poleward for cyclonic eddies (CEs) and equatorward for anticyclonic eddies (AEs). Eddies formed within the boundaries of the ACC have an effective eastward propagation with respect to the mean deep ACC flow, and the mean meridional drift is reversed, with warm-core AEs propagating poleward and cold-core CEs propagating equatorward. This circulation pattern drives downgradient eddy heat transport, which could potentially transport a significant fraction (24 to 60 $\times$ 10^{13} W) of the net poleward ACC eddy heat flux.

We show that the generation of relatively large amplitude eddies is not a ubiquitous feature of the SO but rather a phenomenon that is constrained to five isolated, well-defined "hotspots". These hotspots are located downstream of major topographic features, with their boundaries closely following f/H contours. Eddies generated in these locations show no evidence of a bias in polarity and decay within the boundaries of the generation area. Eddies tend to disperse along f/H contours rather than following lines of latitude. We found enhanced values of both buoyancy (BP) and shear production (SP) inside the hotspots, with BP one order of magnitude larger than SP. This is consistent with baroclinic instability being the main mechanism of eddy generation. The mean potential density field estimated from Argo floats shows that inside the hotspots, isopycnal slopes are steep, indicating availability of potential energy. The hotspots identified in this thesis overlap with previously identified regions of standing meanders. We provide evidence that hotspot locations can be explained by the combined effect of topography, standing meanders that enhance baroclinic instability, and availability of potential energy to generate eddies via baroclinic instabilities.

Chapter 1

Introduction

1.1 Background

1.1.1 The Southern Ocean and its role in the climate system

The ocean forms a major constituent of the climate system, sequestering climatically critical properties such as heat and carbon at depth, and modulating their inter- and intra-hemispheric transport around the globe (e.g., *Siedler et al.*, 2013). Observing and quantifying the ocean's variability, and understanding the processes driving it are topics of on-going study. The Southern Ocean plays a central role in governing the ocean's impact on climate (e.g., *Toggweiler and Samuels*, 1995; *Marshall and Speer*, 2012). In particular, the Southern Ocean plays a unique role in the global ocean's uptake and storage of anthropogenic carbon dioxide and heat redistribution; these are key aspects of the climate system (e.g., *Ito et al.*, 2010; *Frölicher et al.*, 2015). With the increased attention that the Southern Ocean has received in recent decades, a three-dimensional picture of the circulation in the Southern Ocean has emerged. This complex circulation is now understood to be composed of four major components: (1) the exchange of buoyancy with the atmosphere, (2) the momentum imparted by the wind at the surface (3) water mass modification, and (4) eddy fluxes of heat and momentum modulated by the interaction between the flow and topographic obstacles.

The Southern Ocean's most prominent feature is the eastward flowing Antarctic Circumpolar Current (ACC). The ACC is the longest and most energetic current in the world ocean. It follows a 25,000 km long circumpolar path around Antarctica. Its volume transport relative to the bottom, as measured in the narrowest section of its path (the Drake Passage), is roughly $173 \pm 7 \times 10^6$ m^3 s^{-1} (e.g., *Donohue et al.*, 2016). The circumpolar nature of the ACC due to the lack of continental barriers, has profound implications for its dynamics. As a consequence of the lack of meridional boundaries to support a zonal pressure gradient, no net geostrophic meridional flow can occur above the sill depth of Drake Passage (*Munk and Palmén*, 1951). The ACC is composed of several narrow-band, vigorous currents or jets (e.g., *Nowlin and Klinck*, 1986). Each of these jets is associated with sharp cross-stream gradients of density, temperature, salinity and other properties. Historically three main fronts have been identified: the Subantarctic Front, the Polar Front, and the southern ACC front (e.g., *Orsi et al.*, 1995). However more modern studies have refined this picture of the ACC by suggesting that each of the fronts exists as multiple filamented structures (e.g., *Sokolov and Rintoul*, 2009b; *Thompson and Richards*, 2011). Fronts are important in defining distinct regions with different properties. For example, when characterizing ocean-atmosphere CO_2 fluxes, fronts are commonly used as boundaries that divide regions with different rates of CO_2 fluxes (e.g., *Marinov et al.*, 2006).

Observational evidence of changes in the Southern Ocean are well documented. A significant warming of the upper layer of the Southern Ocean over the last 70 years has been identified by comparing temperature profiles collected during the 1990s with historical measurements starting in the 1930s (*Gille*, 2008). An understanding of the interplay between key aspects of the Southern Ocean dynamics, such as eddy - mean flow interaction and the response to changes in wind stress forcing is fundamental to a better understanding of the role that the Southern Ocean plays in the global climate. A critical part, therefore, is the definition and estimation of baseline mean hydrographic properties, and how these mean properties evolve with time. Chapter 2 of this dissertation is dedicated to the estimation of the mean density, temperature and salinity fields of the South-

ern Ocean, with a particular focus on a the impact of eddies on these fields. We address the following issues:

i. The presence of time variability arising from eddies in the Southern Ocean means that simple time averaging of the hydrographic fields can lead to bias in the mean state. The altimeter provides information about the anomalous density field that can be used to remove some of the eddy variability. The complementary nature of the two observing systems allows improved estimates of the time-averaged hydrographic fields. We estimate the mean upper ocean hydrographic fields of the Southern Ocean by combining in situ Argo float measurements and altimeter data. The removal of eddy variability allow us to compare mean fields estimated solely using Argo floats with mean fields estimated using Argo floats and altimeter data.

ii. The combined analysis of Argo floats and altimeter data can provide insight into the impact of eddies on the background fields. We quantify the relative importance of salinity and temperature anomalies on the density field. We show that there is a geographical pattern that can be explained by the distribution of the well-known water masses that traverse the Southern Ocean.

1.1.2 The role of the eddies in the Southern Ocean

The quasi-mean state of the Southern Ocean can be described as a vigorous current flowing around Antarctica (e.g., *Sokolov and Rintoul*, 2009a). Energy imparted by the wind drives the ACC by steepening density surfaces (e.g., *Marshall and Speer*, 2012). The details of the momentum balance are still a topic of active research- however, the general consensus is that instabilities of the current act to flatten out the density surfaces, counterbalancing the steepening of density surfaces by the wind (e.g., *Meredith and Hogg*, 2006; *Marshall and Speer*, 2012). This instability process results in the generation of mesoscale eddies. Eddies, vortex-like structures with a diameter of roughly 20 to 100 km, are a ubiquitous feature of the global ocean - the ocean analogy to atmospheric storms. Just as in the atmosphere, they tend to form in regions of strong shear and jets, and are extremely energetic

in the Southern Ocean (e.g., *Chelton et al.*, 2011).

Eddies play two key roles in the Southern Ocean. First, they are a fundamental component of the heat balance. The Southern Ocean transfers heat to the atmosphere at polar latitudes (a negative buoyancy flux for the upper ocean). This heat loss is mainly compensated by eddies that transport heat poleward across the mean zonal ACC flow (e.g., *Volkov et al.*, 2010). Secondly, eddies play a role in the momentum balance of the Southern Ocean, fluxing momentum both horizontally and vertically from the surface to the deep layers of the Southern Ocean (e.g., *Thompson*, 2008). Ultimately deep bottom currents interact with topographic features giving rise to bottom form stress, and transferring the momentum imparted by the wind to the ocean to the solid earth (e.g., *Masich et al.*, 2015). The transport of momentum is mediated by both transient eddies and standing eddies (defined as anomalies of the zonally averaged flow). Chapters 3 and 4 of this dissertation are dedicated to the study of these transient eddies in Southern Ocean. In particular we consider:

i. The Southern Ocean has a vigorous and dense eddy population. However no attempt to map the generation and decay locations of eddies in the literature. This is of particular importance as it provides information on the locations where energy is converted from the mean to the turbulent field.

ii. In the Southern Ocean, instabilities are the mechanism to counterbalance the energy imparted by the wind. It is believed that the main energy pathway is the transfer of mean potential energy to eddy kinetic energy via baroclinic instabilities (e.g., *Treguier et al.*, 2007). We test this hyphothesis by quantifying the transfer terms of the turbulent kinetic energy equation. The estimation of the buoyancy and shear production provides a quantitative way to measure the relative importance of baroclinic and barotropic instabilities. A dominance of the former would indicate that energy is mainly transferred to the turbulent kinetic energy field from the potential energy field, while a dominance of the latter would indicate a transfer from the mean kinetic energy field.

1.2 Outline of the Dissertation

1.2.1 Chapter 2: 4-D structure of the Southern Ocean

1.2.1.1 Mean field estimation

Chapter 2 of this dissertation focuses on the estimation of mean temperature, salinity and density fields of the Southern Ocean. The Southern Ocean, due to its deep penetrating jets and eddies, is well-suited for studies that combine surface and sub-surface data. The chapter explores the usage of Argo profiles in combination with sea surface height (SSH) altimeter data to remove eddy variability from Argo observations. The temporal variability associated with the mesoscale eddy field can increase the uncertainty of the mean density field estimated from float profiles. Therefore by removing eddies, a more accurate estimation of the mean state can be achieved. The combination of altimetry and Argo float data has proved successful for reconstructing the density field of the North Atlantic (*Willis and Fu*, 2008). As shown by previous studies in other regions of the world ocean (e.g., *Gilson et al.*, 1998; *Willis et al.*, 2004; *Willis and Fu*, 2008), upper ocean density anomalies and SSH anomalies (SSH') are strongly correlated. We show that this holds in the Southern Ocean, and we extend the methodology to the temperature and salinity fields.

1.2.1.2 Impact of eddies on the background field and reconstruction of the time-varying component

The combined analysis of SSH altimetry with temperature and salinity observations provides insight into the impact of eddies on the background field. By mapping the iso-surface displacements due to eddies, we are able to distinguish regions where density anomalies are controlled by salinity variations rather than temperature variations. The regression analysis between SSH' and hydrographic variables also provides a means to reconstruct the eddy-component of the fields, and hence the four-dimensional structure of the Southern Ocean. The regression coefficients derived from the linear regression, a function of latitude, longitude

and depth can be used as a proxy in combination with the altimeter signal to reconstruct the sub-surface variability captured by the altimeter. We present the time-varying field reconstructed using the regression coefficients and discuss its potential applications.

1.2.2 Chapter 3: Downgradient heat transport in the ACC due to reverse meridional eddy migration

Chapter 3 focuses on eddy kinematics in the Southern Ocean. We study the motion of eddies in the Southern Ocean using satellite altimetry and output from an assimilating numerical ocean model. We show that the Southern Ocean has two distinct eddy motion regimes. Outside the boundaries of the ACC, eddies propagate westward with a mean meridional drift directed poleward for cyclonic eddies (CEs) and equatorward for anticyclonic eddies (AEs). This result is consistent with eddy observations in other regions of the world ocean. However eddies formed within the boundaries of the ACC present an effective eastward propagation with respect to the mean deep ACC flow, and the mean meridional drift is reversed, with warm-core AEs propagating poleward and cold-core CEs propagating equatorward. We present an explanation of this "reversed" meridional drift based on consevation of potential vorticity (PV) and discuss the implications of these findings on the meridional eddy heat flux in the Southern Ocean.

1.2.3 Chapter 4: Eddy generation and decay in the Southern Ocean

The final chapter of this dissertation is dedicated to mapping the generation and decay locations of the eddies identified in the previous chapter. Output from an assimilating numerical ocean model and the density field derived in Chapter 2 are used to assess the energy sources and the generation mechanism associated with eddies. We find that relatively large amplitude eddies are generated in well-defined isolated regions. These areas of high probability of eddy generation are located downstream of major topographic features with their boundaries closely

following f/H contours. The estimation of the buoyancy and shear production shows enhanced values of both terms inside the generation areas. However, buoyancy production is two orders of magnitude larger than shear production. This result is consistent with eddy generation via baroclinic instability. Finally, we show that eddy hotspot locations can be explained by the combined effect of prominent topographic features and standing meanders, with wind-steepened isopycnal slopes providing available potential energy for baroclinic instability.

Chapter 2

Four-dimensional structure of the Southern Ocean: Impact of eddies and frontal displacements on the background fields

The Southern Ocean, due to its deep penetrating jets and eddies, is well-suited for studies that combine surface and sub-surface data. This chapter explores the use of Argo profiles and sea surface height (SSH) altimeter data from a statistical point of view. A linear regression analysis of SSH and hydrographic data reveals that the altimeter can explain, on average, about 35% of the variance contained in the hydrographic fields and more than 95% if estimated locally. Correlation maxima are found at mid-depth (500-2000 dbar), where dynamics are dominated by geostrophy. Near the surface, diabatic processes are significant, and the variance explained by the altimeter is lower. Since SSH variability is associated with eddies, the regression of SSH with temperature (T) and salinity (S) shows the relative importance of S vs T in controlling density anomalies. The AAIW salinity minimum separates two distinct regions; above the minimum density changes are dominated by T, while below the minimum S dominates over T. The regression analysis provides a method to remove eddy variability, effectively

reducing the variance of the hydrographic fields. Comparison of the mean fields with and without the altimeter signal shows that differences can be significant along the path of the Antarctic Circumpolar Current, with maximum differences occuring at intermediate depths but extending from the surface to 1500 dbar. The regression coefficients, a function of latitude, longitude and depth can be used as a proxy in combination with the altimeter signal to reconstruct the sub-surface variability captured by the altimeter.

2.1 Introduction

Observations of the Southern Ocean during the past 5-6 decades have shown signficant warming (*Gille*, 2008; *Purkey and Johnson*, 2010) and freshening (*Böning et al.*, 2008; *Meijers et al.*, 2011b) throughout the water column. A poleward shift in the ACC frontal structure (*Sokolov and Rintoul*, 2009b), driven by a poleward intensification of the westerly winds (*Thompson and Richards*, 2011), could partially explain the observed trends. These changes have numerous implications, ranging from the amount of heat that reaches the Antarctic continent (*Meijers et al.*, 2011b) to the distribution of organisms (*Cubillos et al.*, 2007). *Jacobs* (2006) provides an in-depth review of these changes.

Changes in ocean properties are most easily characterized with respect to mean hydrographic fields and their temporal variability. Studies mapping the mean fields of the Southern Ocean are scarce and there have been comparatively few attempts to reconstruct the time-varying component (*Meijers et al.*, 2011a). Until recently, sparse observations limited our ability to map temperature, salinity and density distributions in the Southern Ocean. Historically the Southern Ocean was undersampled compared with other regions of the world ocean, especially during the Southern Hemisphere winter. With the advent of the Argo program, the summer bias of observations has decreased steadily (*Roemmich et al.*, 2009). The combined use of Argo and satellite altimetry data provides an unprecedented opportunity to estimate the mean and time-varying components of the ocean. This has been exploited in numerous regions around the globe (e.g., *Willis and Fu*,

2008).

In this chapter we present estimates of the mean temperature, salinity and density fields of the Southern Ocean, obtained by combining in situ Argo float measurements and altimetric measurements of sea surface height (SSH). This technique has proved successful for reconstructing the density field of the North Atlantic (*Willis and Fu*, 2008). The basic premise is that temporal variability associated with the mesoscale eddy field can increase the uncertainty of the mean density field estimated from float profiles. Therefore by removing eddies, we can produce a more accurate estimation of the mean state. As shown by previous studies in other regions of the world ocean (e.g., *Gilson et al.*, 1998; *Willis et al.*, 2004; *Willis and Fu*, 2008), upper ocean density anomalies and SSH anomalies (SSH') at these scales are strongly correlated. We show that this holds in the Southern Ocean, and we extend the methodology to the temperature and salinity fields.

The regression analysis also provides a means to reconstruct the eddy-component of the fields, and hence the four-dimensional structure of the Southern Ocean. In addition, the combined analysis of SSH altimetry with temperature and salinity observations provides insight into the impact of eddies on the background field. By mapping the iso-surface displacements due to eddies, we are able to distinguish regions where density anomalies are controlled by salinity variations rather than temperature variations.

This chapter is organized as follows. Section 2.2 describes the data, quality-control procedure, and methodology used in the analysis. Section 2.3 discusses the use of altimeter data to minimize the mesoscale signal inherent in the in situ measurements. The analysis of the variance explained by the altimeter and the impact of eddies on the background field is also discussed. Section 2.4 presents the decorrelation scales, objectively mapped mean fields and the reconstruction of the time-varying fields. Finally conclusions and potential uses of this novel dataset are presented in section 2.5.

2.2 Data and Methods

2.2.1 Argo floats: methodology

This analysis relies on data from the on-going Argo array of profiling floats. Argo profiles for the region south of 30°S were retrieved from the U.S. Global Ocean Data Assimilation Experiment Global Data Assembly Center (USGODAE GDAC). Profiles are used if they extend to depths of 500 m or deeper and were collected from January 2001 to December 2013. Only delayed-mode profiles were retained since real-time profiles, i.e. data available within 24 hours of the float reaching the surface, are not corrected for sensor drifts or offsets (*Wong et al.*, 2015). In addition pressure, salinity, temperature, float location and date measurements were omitted if they did not pass the quality control routine for delayed-mode data (quality flag not set to 1, see *Wong et al.* (2015) for details about the quality control process). As a final quality-control step, profiles were grouped in 144 geographic bins of 10° latitude × 10° longitude, and a visual inspection was made for each bin in order to remove gross outliers. Once the outliers were removed the standard deviation for each bin was computed, and all profiles with observations outside three standard deviations were also removed. These quality control criteria eliminated approximately 8.5% of the 222,083 delayed-mode profiles available within the study domain.

All the analyses performed in this study were done both in pressure (P) and neutral density coordinates (γ). The two coordinate systems provide complementary information, as will be shown in section 2.3. For the pressure level grid, the spacing between levels is 10 dbar above 200 dbar and 50 dbar from 200 dbar to 2000 dbar: This produces 56 levels in total. In neutral density coordinates, a total of 50 levels were defined, from 24.2 to 28.5 kg m^{-3} with a variable spacing of 0.1 and 0.05 kg m^{-3}. For each observation, Conservative Temperature (Θ) and Absolute Salinity (S_A) were computed using the thermodynamic equation of state (*IOC et al.*, 2010). Since Argo profiles do not measure at fixed standard depths, a piecewise cubic Hermite scheme (*De Boor*, 2001) was used to interpolate Θ and

S_A onto the defined pressure levels. Potential density (σ_θ) was estimated from the interpolated fields. No significant differences were found by computing σ_θ before interpolating in the vertical direction. For the neutral-density-coordinate analysis, the neutral surfaces were fit to the Argo profiles using the routines developed by *Jackett and McDougall* (1997). Finally, the pressure for all γ surfaces P_γ was computed. As will be shown later, pressure anomalies on γ surfaces (P'_γ) can be correlated with the altimeter signal to yield information about the instantaneous displacement of the neutral density surfaces.

2.2.2 Argo floats: spatial and temporal distribution

The temporal and meridional distribution of quality-controlled Argo profiles is not homogeneous (Figure 2.1). A significant bias toward the second half of the record (2007 to 2013) is evident, with 75% of the profiles measured after 2006. The time required to complete quality control is reflected in the significantly lower number of profiles available for 2013. The spatial distribution shows sampling asymmetry in the meridional direction and, to a lesser extent, in the zonal direction (Figure 2.2). A rapid decrease in the number of profiles per zonal band south of 56°S stems from the challenges of deploying floats at high latitudes; most Argo floats are not designed to return data under ice, so they are deliberately deployed sufficiently far north to avoid seasonal ice cover. As a result, the Southern Ocean is under-sampled south of the Polar Front (Figure 2.2). Although the zonal distribution is more uniform than the meridional distribution, heterogeneous sampling is also evident. Due to the nature of this type of measurement, regions where the flow is more energetic tend to be less well sampled (in the core of the ACC throughout the Southern Ocean, the Agulhas recirculation region in the Indian Ocean, the Brazil-Malvinas confluence in the Atlantic) than regions of slow flow or convergence, such as the southern limbs and interior regions of the subtropical gyres. The Pacific Ocean and the eastern side of the Indian basin are the best sampled regions, with the Atlantic basin being the least well sampled.

2.2.3 Altimeter data

For this work we use gridded SSH' fields from the SSALTO/Duacs multi-mission altimeter products (*Ssalto/Duacs*, 2011). Anomalies for the study period (2001-2013) were computed using the delayed mode product (DT-MSLA, "Upd", Duacs version 11.0.0) gridded at daily intervals on a $1/3^\circ \times 1/3^\circ$ Mercator grid. The combination of four satellites (Jason-1&2, T/P, Envisat, GFO, ERS-1 & 2 and Geosat) improves the mesoscale structure resolving 100-km wavelengths in the Southern Ocean (*Pascual et al.*, 2006).

To study the relation between the SSH' field measured by the altimeter and the Argo observations, a space-time interpolation scheme was applied to the SSH' fields. The gridded SSH' fields were linearly interpolated in space to the location of each Argo profile, and then a cubic spline temporal interpolation was performed for each SSH' within a 10-day window centered at the time of each Argo profile. For the spatial interpolation, a 1000 km^2 area centered in the location of the Argo profile was used in order to capture the eddy variability.

2.3 Ocean surface topography and sub-surface variability

Changes in SSH can be driven by a horizontal redistribution of mass, i.e. barotropic processes, or due to density changes associated with baroclinic processes. The small surface displacements detected by the altimeter can be used to reconstruct hydrostatic baroclinic modes in the ocean (*Wunsch*, 2013). These surface displacements, a small fraction of the interior isopycnal displacements, are related to the stratification of the water column. The regression of altimetric SSH' with interior in situ observations provides a means to reconstruct the interior isopycnal displacements and infer the stratification of the water column. Section 2.3.1 explains the methodology for constructing spatial functions that relate σ_θ, Θ and S_A anomalies, in pressure level coordinates, to surface displacements measured by the altimeter. In neutral density coordinates, the instantaneous displacement of γ

surfaces (P'_γ) can be related to surface displacements. The methodology is based on the assumption that to leading order the background stratification of the water column is only a function of space, and time variations are sufficiently small to be neglected; hence a given isopycnal displacement would produce the same surface displacement at different times.

2.3.1 Methodology

To test whether a significant linear relationship exists between SSH' and a given hydrographic variable (ϕ), the domain was subdivided into three-dimensional cells of 4° longitude by 2° latitude, with a vertical resolution defined by the grid used to interpolate the Argo profiles (see section 2.2.1). The horizontal area of the cells was chosen as a compromise between the need for high spatial resolution to resolve mesoscale features and the need for large number of observations in each cell to achieve statistical significance. On average, each regression cell contains 126 pairs of observations (with a maximum of 521 pairs). For each cell, the linear regression of SSH' with ϕ was computed in P and γ coordinates (Θ', S'_A and σ'_θ for P level coordinates and Θ', S'_A and P'_γ for γ coordinates). The squared correlation coefficient (R^2) statistic and its significance (p) were also computed (see for example *Draper and Smith* (2006)).

2.3.2 Variance explained by the altimeter

In order to justify the assumption of a linear relationship between SSH' and hydrographic variables, two criteria must be evaluated: First, is the regression significant in a statistical sense? Second, is this regression related to any physical process that links the two variables? Around 76% of the 3.6 million grid cells in the three-dimensional array of mapped values have regression coefficients that are statistically significant at the 95% level for SSH' and S'_A. For σ'_θ and Θ' percentages drop to 73%. The regression analysis performs particularly well at the core of the ACC (38°S - 52°S, 700 - 1300 dbar), where higher values of R^2 are found. This can be illustrated by computing the zonal average fraction of statistically

significant cells per pressure level as a function of latitude band (Figure 2.3). The lower percentages of significant cells, and also smaller R^2 values, are concentrated in the southern section of the domain (south of 62°S) and in the mixed layer (pressure levels above 100 - 200 dbar). The poor performance of the linear regression at latitudes poleward of 60°S is mainly due to the low number of observations (Figure 2.2). In contrast, near the surface the low values of R^2 are likely explained by processes not related to dynamic topography. Air-sea fluxes that drive upper-ocean variability are the primary candidates. To test whether the seasonal signal degrades the regression near the surface, the analysis was also performed using only observations collected during winter months or summer months, but the seasonal results show no significant increase in the explained variance.

The correlation coefficient, R^2, between SSH' and ϕ varies with depth. While one might hypothesize that correlations should be largest in the upper ocean relative to the mid-depth ocean, in reality we find that the maximum R^2 averaged over isobars for γ' and Θ' occurs at 1000 dbar (Figure 2.4). Interestingly S'_A has a local minimum at that pressure level and peaks at 1350 dbar. The equivalent barotropic nature of the ACC has been pointed out in several studies based on observations (e.g., *Gordon et al.*, 1978; *Phillips and Rintoul*, 2000), as well as numerical models (e.g., *Ivchenko and Richards*, 1996; *Killworth and Hughes*, 2002). Although recent studies showed a nonequivalent barotropic behavior in some regions of the ACC (*Phillips and Bindoff*, 2014), an equivalent barotropic assumption is valid to first order since the mean rotation is zero (*Phillips and Bindoff*, 2014). The uniformly high values of R^2 below 400 dbar might be a consequence of the relatively unidirectional flow of the ACC. The domain-averaged R^2 between SSH' and γ' is 0.39, and it can be significantly higher if it is estimated locally. A similar R^2 is obtained by regressing SSH' and Θ', while a smaller value (0.28) is obtained for S'_A.

In neutral density coordinates, R^2 depends on the displacement (P'_γ) of the neutral density surfaces with respect to the average pressure level P_γ. On average, high values of R^2 between SSH' and P'_γ are confined to the 27.2 - 28.0 kg m^{-3} neutral density range (Figure 2.4, red thick solid line). Not surprisingly,

no significant signal is seen in the regression between SSH' and S'_A or Θ' when the analysis is done in neutral density coordinates (Figure 2.4, red thin solid and dash-dot lines respectively). These low R^2 values of S'_A and Θ' suggest that the main source of SSH' seen with the altimeter is the displacement of isopycnals, which conserve their Θ and S_A properties as they are displaced.

2.3.3 Three-dimensional structure of the regression slope

2.3.3.1 Sources of sea surface height variability

Current satellite altimeters measure ocean surface topography at 6 or 7 km resolution in one dimension along the satellite ground tracks, which are separated by gaps of 200 to 300 km. Merged satellite products reduce the gap between tracks, increasing the effective resolution, and wavelengths larger than about 150 km can be identified (*Ducet et al.*, 2000). At this resolution limit, the major sources of mesoscale features seen by the altimeter are planetary Rossby waves, quasi-geostrophic eddies and steric height effects due to diabatic changes near the surface. In addition, regions with strong jets like the ACC or western boundary currents have a strong signal in SSH' associated with the horizontal displacements of jets.

Historically, planetary Rossby waves and quasi-geostrophic eddies have proven difficult to distinguish because eddy propagation velocities observed by the altimeter are similar to non-dispersive Rossby waves (*Chelton et al.*, 2007). Early interpretations of SSH' as seen by the TOPEX/Poseidon altimeter favored a Rossby wave interpretation (*Chelton and Schlax*, 1996). However high-resolution SSH' fields produced by the merging of several altimeters (*Ducet et al.*, 2000) suggest that most of the observed mesoscale features are non-linear eddies (*Chelton et al.*, 2007). Further evidence was provided by *Early et al.* (2011), who compared the spectral characteristics of the mesoscale features as seen by altimeter with those of a linear and non-linear quasigeostrophic model; they found that the non-linear case showed better agreement with observations. Therefore, the primary candidates to explain the strong correlation in the hydrographic fields with SSH' seen by the

altimeter are vertical displacements of isopycnals due to quasi-geostrophic eddies and horizontal water mass displacements due to the natural variability of the ACC jets. To leading order eddies and meanders are equivalent, making it difficult to isolate one from the other. In the next section we will show that meridional water mass displacements (due to meandering of fronts), and vertical isopycnal displacements (due to quasi-geostrophic eddies) have the same effect on the anomalies, making both processes virtually indistinguishable from each other.

2.3.3.2 Regression slopes: the effect of quasi-geostrophic eddies

Geostrophic balance links the sub-surface density field with the SSH. Cyclonic eddies correspond to uplifted isopycnals, which increase the average density of the water column, decreasing SSH. Conversely, anticyclonic eddies depress isopycnals and produce positive SSH'. Therefore we expect the linear regression between SSH' and σ'_θ to have negative regression slopes, as we found in Figure 2.5a, for a cell located at 400 dbar in the southwest Atlantic region of the ACC (55°S, 314°E). The sign of the regression slopes between SSH' and Θ' (Figure 2.5b) or S'_A (Figure 2.5c) cannot be derived a priori from dynamical arguments, since both depend on the properties of the water mass carried by the eddies and the structure of the mean background field.

The regression of SSH' with σ'_θ, Θ' and S'_A varies with depth and latitude, and to a lesser extent with longitude. Meridional sections of the regression slope east of Drake Passage (45°W) are analyzed here, but the same conclusions can be drawn from meridional sections at other longitudes as well. The regression between the altimeter signal and the density field (Figure 2.6a) follows the relationship explained above. Negative slopes are found everywhere except for a few areas (mainly south of 60°S) with positive slopes but not statistically significant (as denoted by hatched areas in Figure 2.6). A constant pressure section at 1000 dbar shows the expected negative values throughout the whole domain (Figure 2.7a).

The regression with Θ' (Figure 2.6b) shows positive slopes throughout the water column. Mean temperature (marked as black solid lines in Figure 2.6b) decreases monotonically with depth; therefore a depression of the isopycnals asso-

ciated with an anticyclone (positive SSH') would produce positive Θ anomalies, resulting in positive regression slopes. By the same argument, positive regression slopes are also obtained when the isopycnals are uplifted by cyclonic eddies. The magnitude of the regression slopes can be up to 0.3°C cm^{-1}, with higher values occurring where the temperature gradient is largest. A constant pressure section at 1000 dbar shows positive values throughout the whole domain (Figure 2.7b). As with density, this result is not surprising, since the sign of the regression slope is driven by the stratification of the water column and the monotonic decrease of Θ with depth.

Salinity shows the most interesting regression patterns (Figure 2.6c). Positive regression slopes are found above the neutral density surface of 27.3 kg m^{-3}, and negative regression slopes below this surface. The background mean S_A field (shown as black solid lines in Figure 2.6c) shows a minimum at the level of zero regression slope (coincident with the neutral density surface of 27.3 kg m^{-3}), values of S_A increase toward the surface and toward deeper levels. Therefore above the salinity minimum, cyclonic eddies produce negative SSH', while anticyclonic eddies produce positive SSH'; implying a positive regression slope. Below the salinity minimum, the same argument implies negative regression slopes. Figure 2.7c shows the regression slope between SSH' and S'_A at 1000 dbar; positive values are found north of the SAF in the Indian Ocean and in the Southwest Atlantic and Pacific Oceans.

Antarctic Intermediate Water (AAIW) is characterized by a salinity minimum at densities of 27.0 to 27.3 kg m^{-3} and at about 500 to 1000 m depth (see for example *Talley* (2008)). AAIW is formed in the Southeast Pacific (*Sloyan et al.*, 2010), but it becomes a global Southern Hemisphere water mass as it is transported by the ACC to other basins. The transition of the S'_A regression slope occurs at the depth of AAIW. The structure of the regression slope for S'_A can be observed everywhere in the Southern Ocean except in the southeast Pacific, where the signal of the AAIW is weaker, and the salinity minimum is not noticeable (not shown). The domain average regression slopes per pressure level (Figure 2.8) summarize the results observed in the meridional sections. Both σ'_θ and Θ' have positive slope

signs, and a sign reversal occurs for S'_A at 800 dbar due to non-monotonic behavior of the background S_A field with pressure.

2.3.3.3 Regression slopes: the effect of meandering jets

The ACC comprises several jets; both obervations and numerical studies show that these jets are characterized by low-frequency variability on time-scales of months to years (e.g., *Sokolov and Rintoul*, 2009b; *Thompson and Richards*, 2011). The inherent variability of the system leads to strong meridional displacements of water masses. Hence anomalies in the σ_θ, Θ and S_A fields can also be produced by the meanderings of jets.

The regression between SSH' and sub-surface anomalies due to the meridional displacements of jets produces the same three-dimensional structure of the regression slope that the eddies produce via vertical displacements of isopycnals. The mean background σ_θ field is characterized by a strong poleward gradient (Figure 2.12). Therefore poleward displacements of frontal structures produce $\sigma'_\theta < 0$ and $SSH' > 0$, while equatorward displacements produce $\sigma'_\theta > 0$ and $SSH' < 0$. Hence the regression slope is negative for both directions and has the same sign as that produced by vertical displacements of isopycnals due to eddies (see previous section).

The analysis of the regression between SSH' and Θ' is analogous to σ'_θ except that the background Θ field has a strong equatorward gradient instead (Figure 2.13), resulting in positive regression slopes for both horizontal and vertical water mass displacements. Lastly the regression slope between SSH' and S'_A changes sign due to the salinity minimum associated with AAIW (Figure 2.14). Figure 2.9 illustrates the effect of the meandering of jets and the eddies. Anticyclonic eddies and poleward displacements of fronts produce negative regression slopes ($S'_A < 0$ and $SSH' > 0$) below and south of the AAIW axis and positive regression slopes ($S'_A > 0$ and $SSH' > 0$) above and north of the AAIW axis. The same spatial structure of the regression slope is obtained for cyclonic eddies and northward displacements of frontal structures.

2.3.4 Impact of eddies and fronts displacements on the background fields

The relative contribution of S'_A and Θ' to density changes can be quantified by assuming a linear equation of state and computing the ratio between the relevant terms:

$$\sigma = \sigma_0 \ + \ \rho_{ref} \ (\beta_S \ (S_A \ - \ S_A^0) \ - \ \alpha_T \ (\Theta \ - \ \Theta^0)). \tag{2.1}$$

We define the density ratio:

$$\pi = \frac{\alpha_T \ \Theta'}{\beta_S \ S'_A}, \tag{2.2}$$

where $\alpha_T = -\rho^{-1}(\partial\rho/\partial\Theta)$ and $\beta_S = \rho^{-1}(\partial\rho/\partial S)$ are the thermal expansion and saline contraction coefficients respectively. The horizontal density ratio has been used previously, for example to study the relative effect of temperature and salinity on density in the mixed layer (*Rudnick and Martin*, 2002). Here we compute the vertical density ratio to measure the potential relative effect of temperature and salinity on density. The ratio quantifies the relative contribution of temperature and salinity anomalies to density changes in pressure level coordinates. Figure 2.6d shows a meridional section (45°W) of $\log_{10}(\pi)$. Positive values indicate locations where density changes are dominated by temperature, while negative values denote density changes dominated by salinity. Salinity anomalies dominate below the salinity minimum associated with AAIW (Figure 2.6c) and can be up to two orders of magnitude bigger than density changes due to temperature anomalies. Above the salinity minimum, density changes are dominated by temperature anomalies. Temperature anomalies contributions to density changes can be up to three orders of magnitude bigger than salinity anomalies contributions. Figure 2.7d shows the relative contribution of each term at 1000 dbar. At this pressure level the salinity contribution dominates in between the PF and SAF, except in the Southwest Atlantic where the region extends north to the STF. The dominance of salinity below the AAIW salinity minimum can be attributed to the relatively weak vertical temperature gradients, although cabbeling effects might contribute as well. Above the AAIW salinity minimum strong vertical temperature gradients (Figure 2.6b) explain the dominance of temperature over salinity.

2.4 Mean and time-varying fields

2.4.1 The covariance matrix and decorrelation scales

Objective mapping, a best linear unbiased estimator in the least-square sense, provides a way to estimate gridded fields and associated errors from irregularly spaced data (*Bretherton et al.*, 1976). Objective mapping relies on a priori knowledge of the mesoscale statistics. As *Bretherton et al.* (1976) formally showed, if the statistics are estimated from the data themselves, bias is introduced in the mapping procedure. Since the dataset used to compute the decorrelation scales should be independent of the dataset to be mapped, we tested two different independent datasets: the extended CSIRO Atlas of Regional Seas (CARS) climatology (*Ridgway et al.*, 2002) and the World Ocean Circulation Experiment (WOCE) climatology (*Gouretski and Koltermann*, 2004). In both cases we found that the data covariance matrix did not converge for large spatial lags (> 500 km) and significant oscillations were present at intermediate lags (100-300 km) for all pressure levels. Studies based on an eddy-permitting coupled climate model (*Downes et al.*, 2011), and on observations (*Dong et al.*, 2006; *Sokolov and Rintoul*, 2009b) suggest that the intensification of the Southern Hemisphere westerlies over the past decades (*Marshall*, 2003) could have shifted the ACC fronts south, though this remains a subject of debate (e.g., *Graham et al.*, 2012; *Gille*, 2014). Since both climatologies comprise hydrographic observations taken before the year 2000, and this study focuses on observations from 2001 to 2013 (with most of the observations taken after 2006, see Figure 2.1), the shifting of the fronts could possibly explain the inadequate removal of the mean field and, consequently, the observed divergence of the data covariance matrix for large spatial lags. The recent warming of the Southern Ocean (*Gille*, 2002; *Levitus et al.*, 2005) could be another contributing factor.

In light of the possible climate shifts in the Southern Ocean, and since in practice the bias may be a minor consideration when large quantities of data are available, we estimated the covariance matrix, spatial decorrelation scale (L) and

signal-to-noise ratio (SNR) from the Argo dataset itself. These quantities can be sensitive to how anomalies are estimated. For each Argo observation a local mean value was estimated by averaging all the available observations contained in an ellipse centered at the location of the observation. Radii ranging from 100 km to 400 km were tested, and the optimum ellipse (semi-minor axis 200 km and semi-major axis 400 km) was chosen to minimize the mean square error between the estimated covariance function and the analytical fit. A Gaussian function and a two-scale function as defined by *Willis and Fu* (2008) were fit to the data covariance matrix; for all cases the Gaussian function had a lower misfit. This procedure was applied to each subdomain (as defined in section 2.4.2) and for all pressure levels.

The zonal (L_x) and meridional (L_y) decorrelation scales are uniform throughout the water column, except for the upper 100 dbar, which has somewhat smaller values (Figure 2.10). Similar values (100-150 km) were obtained for σ_θ, Θ and S_A. Previous estimates are in general agreement with our results. *Sciremammano* (1980) reported a spatial decorrelation length scale of 80-100 km for temperature estimated from moorings at Drake Passage. *Gille and Kelly* (1996) estimated L in the Southern Ocean to be 85 km using SSH from the Geosat altimeter data. *Lutjeharms and Baker* (1980) analyzed hydrographic data from the Southern Ocean and reported length scales of 150 km. Larger L values (110-1100 km), not estimated from observations due to the sparseness of historical data, were used in the literature for mapping purposes (e.g., *Gille*, 2003a; *Purkey and Johnson*, 2010). No significant anisotropy is evident in comparing L_x and L_y, in agreement with previous studies that evaluated isotropy in the decorrelation scales estimated from SSH observations (*Gille and Kelly*, 1996). However negative lobes are evident in most of the covariance matrices of the zonal component (figure not shown). These negative correlation values, which are not captured by the Gaussian fit, are likely spurious due to the fact that the ACC is not strictly zonal, but a large-scale anti-correlation cannot be fully discarded.

Uncertainties due to temporal and sub-mesoscale variability as well as instrument noise are represented by SNR. The noise level was defined as the variance difference between the analytical fit and the estimated covariance, both at zero

lag. The signal is defined as the estimated covariance at zero lag. On average SNR ranges from 0.4 near the surface ($P < 100$ dbar) to 1 at deeper levels (Figure 2.11). Variability of SNR among subdomains can be significant (as shown by the red and blue envelopes in Figure 2.11). Here Θ shows more variability (Figure 2.11b) than σ_θ or S_A (Figures 2.11a and 2.11c), with values ranging from 0.4 to 2 at pressure levels of 1000 to 1400 dbar. Previous studies of the Southern Ocean used SNR from 1 to 4 (e.g., *Gille*, 2003a; *Purkey and Johnson*, 2010).

2.4.2 Objective mapping of mean fields

The classical objective mapping (*Gandin*, 1965; *Bretherton et al.*, 1976) should only be applied to anomalies, i.e. an a priori knowledge of the mean field is required. Here we applied the method developed by *Davis* (1985), where objective mapping and basis function fitting (e.g., *Armi and Stommel*, 1983; *Davis*, 1998) are combined to avoid the need to specify a priori knowledge of the mean field. For the error budget we followed the method developed by *Le Traon* (1990) which takes into account the additional error due to the lack of knowledge of the mean field.

Objective mapping of large spatial domains involves the inversion of large matrices, and computational complexity grows as the cube of the matrix size (e.g., *Cormen et al.*, 2009). Since the goal is to map temperature, salinity and density for the Southern Ocean at 56 P levels and 50 γ levels, some steps need to be taken to make the problem tractable on a modern workstation. The computational cost was reduced by subdividing the horizontal domain into 18 subdomains each spanning the full latitude range (30°S to 70°S) but only 40° in longitude. Adjacent subdomains overlap by 10° in longitude. This overlap is at least twice as big as the decorrelation scale at high latitudes and several times bigger at lower latitudes. The chosen overlap assures no discontinuities when the full domain is reconstructed by patching the subdomains. The anomalies for each variable to be mapped were averaged in $1/4° \times 1/4°$ bins and the geographic center of the average was computed. The objective mapping for each subdomain and for each vertical level were computed using the bin averages with the mean geographic locations. Mean fields

and error estimates were output on a $1/4^\circ \times 1/4^\circ$ Cartesian grid.

Figures 2.12, 2.13 and 2.14 show objectively mapped three-dimensional mean fields of σ_θ, Θ and S_A respectively. The altimeter signal was removed from the Argo observations prior to objectively mapping the fields. A meridional section of the Atlantic at 30°W, Pacific (160°W) and a circumpolar section along 55°S show the well-known mean structure of the ACC. The characteristic frontal structure of the ACC can be seen at the surface (10 dbar) all along the circumpolar path. The climatological positions of the STF, SAF and PF, as defined by *Orsi et al.* (1995), are shown as white contours for reference. The meridional sections show the vertical structure of the fronts, extending from the surface all the way down to 2000 dbar. Particularly clear is the outcropping of isopycnals (Figure 2.12) and the salinity minimum intrusion of AAIW (Figure 2.14) flowing northward in the Atlantic and Pacific Ocean. Mean fields of σ_θ, Θ and S_A with and without the altimeter signal removed, as well as the error estimates, are available for download at http://somean.ucsd.edu.

2.4.3 Impact of removing the eddy signal on the mean fields

A significant fraction of the sub-surface variability is reflected in the altimeter signal. The domain-averaged variance explained by the altimeter is close to 40% (see section 2.3.2), and can be as high as 95% when estimated locally. Eddy variability can introduce significant biases to the mean fields. Here we assess the impact of removing the eddy signal from the σ_θ, Θ and S_A fields. We quantify the difference by computing the objectively interpolated maps with and without the altimeter signal removed.

Figure 2.15a-c shows the differences for each variable at 300 dbar. Angular brackets $\langle\ .^*\ \rangle$ denote variables with the altimeter signal removed. For clarity, and to emphasize regions where maximum differences occur, differences less than 0.03 kg m^{-3} for σ_θ, 0.04 g kg^{-1} for S_A and 0.4°C for Θ are not shown. In general, maximum differences occur along the path of the ACC, bounded by the STF and PF. North of the ACC, areas with strong eddy activity such as the Brazil-Malvinas

confluence and the Agulhas recirculation region also show significant differences in all variables. Density differences at this pressure level can be up to 0.2 kg m^{-3} (Figure 2.15a), but values up to 0.7 kg m^{-3} were found. Temperature and salinity differences tend to compensate each other, attenuating density differences. This effect is clear in the Brazil-Malvinas confluence region and the Agulhas recirculation region (Figure 2.15b-c), where the sign of temperature and salinity differences is in phase. At this pressure level, density differences in the Atlantic and Indian Ocean sectors of the ACC are mainly driven by temperature differences (Figure 2.15b), while density differences in the Pacific sector of the Southern Ocean are mainly driven by salinity differences (Figure 2.15c).

Figures 2.15d-f show the pressure level at which maximum differences are found averaged in 2° longitude × 1° latitude bins. Density presents a very clear pattern: along the path of the ACC, maximum density differences are found in the 400-800 dbar range (Figure 2.15d). North of the ACC, density differences peak at much shallower depths (<200 dbar). Temperature (Figure 2.15e) and salinity (Figure 2.15f) also show maximum differences at the 400-800 dbar range along the path of the ACC. In contrast to what the density differences show, north of the ACC, the Atlantic and Indian Oceans show regions where maximum differences in S_A and Θ occur at pressure levels greater than 400 dbar. The compensatory effect between Θ and S_A (Figures 2.15b-c) explains the discrepancy in the pressure level at which maximum differences occur. The subsurface maxima along the path of the ACC for all variables is in agreement with the correlation analysis, which shows that R^2 values between SSH' and hydrographic variables peak below 400 dbar (Figure 2.4).

Figure 2.16 shows a circumpolar vertical section (denoted by the green dash-dot line in Figure 2.15a-c) of the difference between the mean fields computed from Argo floats with and without the use of the altimeter to remove the eddy signal. Differences in the density field (Figure 2.16a) have sub-surface maxima (as shown by Figure 2.15d) and coherent vertical structure, evidence of the the deep penetration of eddies in the water column. Temperature differences (Figure 2.16b) can be up to -2°C, with maximum values at shallower depths (< 400 dbar).

Salinity differences (Figure 2.16c) show a change in sign at mid-depth, associated with the AAIW salinity minimum.

2.4.4 Reconstruction of the time-varying fields

Sub-surface time-series observations in the Southern Ocean are scarce, often confined to very small areas and a limited time-span. Large-scale time-space analyses are therefore difficult to perform without the aid of additional information, such as numerical modeling. The regression analysis between the altimeter signal and the Argo profiles provides a means to reconstruct the four-dimensional fields of σ_θ, Θ and S_A. For each variable ϕ, the altimeter signal can be projected on the water column using the regression coefficients $\alpha(\phi)$ and the SSH' (see section 2.3.1):

$$\phi_p(x, y, z, t) = \alpha(\phi(x, y, z)) \times SSH'(x, y, t), \tag{2.3}$$

where x,y,z and t represent the space and time coordinates. Each variable, ϕ, can then be objectively mapped (represented by curly brackets in equation 2.4) after removing the altimeter signal:

$$\hat{\phi}(x, y, z) = \{\phi(x, y, z, t) - \phi_p(x, y, z, t)\}. \tag{2.4}$$

Finally the full 4-dimensional field (Φ) for each variable can be reconstructed by adding the objectively mapped mean field, $\hat{\phi}$, to the projected variables, ϕ_p:

$$\Phi(x, y, z, t) = \hat{\phi}(x, y, z) + \phi_p(x, y, z, t). \tag{2.5}$$

An animation of the four-dimensional Θ field is available as supplementary material. The regression coefficients to reconstruct the four-dimensional field of σ_Θ, Θ and S_A are available for download at http://somean.ucsd.edu. Previous attempts to reconstruct the time-varying component of the hydrographic fields in the Southern Ocean are limited to *Meijers et al.* (2011a). The main difference between this and the *Meijers et al.* (2011a) approach is that the latter used a single empirical relation between SSH and dynamic height anomalies for the whole Southern Ocean. In this work we attempt to reconstruct the spatial variability of the regression functions for each hydrographic variable.

2.5 Discussion and conclusions

The goal of this chapter has been to develop a best estimate of the mean and time varying properties of σ_θ, Θ and S_A for the Southern Ocean, by simultaneously using Argo floats and altimeter data. Following the approach of *Willis and Fu* (2008), we have shown that the Southern Ocean, due to its deep penetrating jets and eddies, is well-suited for this technique. The altimeter can explain, on average, about 35% of the variance contained in the hydrographic fields. If estimated locally, more than 95% of the variance can be accounted by the altimeter at the core of the ACC.

The linear regression model implies a dynamical link between SSH and σ_θ anomalies based on geostrophic balance. Near the surface, adiabatic processes are a source of a significant fraction of the observed variance. This explains why the model does a relatively poor job in the upper ocean. At high latitudes (south of 60°S) the relatively low number of observations results in regressions with statistical significance below the 95% standard threshold. Below the partially adiabatic upper layer and north of 60°S, close to 50% of the variance is captured by the altimeter. The residual variance not captured by the altimeter is associated with the barotropic component and the deep baroclinic contribution to the SSH that is below the sampling region of the Argo floats.

The dynamical link between SSH and σ_θ anomalies sets the spatial structure of the regression function $\alpha(\sigma'_\Theta)$. For $\alpha(\Theta')$ and $\alpha(S'_A)$, the mean background fields of Θ and S_A set the spatial structure of the regression functions. The monotonic decrease of the Θ field with depth implies a positive regression between Θ and SSH anomalies, regardless of the nature of the perturbation. The S_A field however, with a minimum at mid-depth associated with low salinity AAIW, yields a positive regression above the axis of AAIW and a negative below it.

The relative contribution of S_A and Θ to density changes shows that below the AAIW salinity minimum, S'_A contributions can be up to two orders of magnitude bigger than Θ' contributions. Above the AAIW minimum, vertical Θ gradients are significant, and density changes are dominated by the Θ field. The

linear regression between the SSH' and Θ and S_A anomaly fields depends on the coordinate system. On isobaric coordinates, the regression analysis accounts for a signficant fraction of the variance of the Θ and S_A anomaly fields, and follows the same geographic pattern described for density. On neutral density coordinates, the linear regession fit fails to account for the variance observed in the Θ and S_A fields (R^2 values range from 0.1 near the surface to 0.2 at the core of the ACC). The difference in the amount of variance explained by the altimeter using isobaric versus neutral density coordinates is consistent with displacements of isopycnals conserving their Θ and S_A properties.

Two mechanisms were identified as sources for the in situ anomalies correlated with the altimeter signal: quasi-geostrophic eddies and the meandering of the ACC jets. The regression analysis between SSH' and in situ anomalies shows that eddies and frontal displacements produce the same regression pattern, making it diffcult to isolate individual contributions. Although to leading order, meanders of the jets and eddies are the same, the mechanism that generates the regression pattern in each case is different: quasi-geostrophic eddies are associated with vertical displacements of isopycnals while the meandering of the ACC jets generate horizontal water mass displacements.

Spatial decorrelation scales were found to be short (less than 200 km everywhere, and in most cases within the 125 - 150 km range). These short scales are consistent with the presence of a vigorous eddy field. Previous estimations of decorrelation scales in the Southern Ocean are in general agreement with our findings (e.g., *Lutjeharms and Baker*, 1980; *Sciremammano*, 1980; *Gille and Kelly*, 1996). The homogeneity of the decorrelation scales thoughout the water column was not previously reported in the literature. The rapid decorrelation scales found at deep water is an indication of the deep penetration of the eddies in the Southern Ocean.

The linear regression between the altimeter and the Θ, S_A and σ_θ fields provides a method to remove eddy variability captured by the altimeter, effectively reducing the variance of the fields. Since one of the largest sources of error in estimates of mean fields is caused by temporal variability related to the eddy field,

there is also an improvement of the error estimate of the mean fields. The comparison of the mean fields with and without the removal of the altimeter signal shows significant differences all along the path of the ACC, with maximum differences occuring at intermediate depths but extending from the surface to 1500 dbar. The signs of temperature and salinity differences seem to be in-phase with spatially varying temperature and salinity anomalies of the same sign. The compensating behavior of Θ and S_A anomalies tends to attenuate density differences.

The complementary nature of the Argo and altimeter observations was also exploited to reconstruct the time-varying fields of Θ, S_A and σ_θ. The altimeter signal was regressed with Θ, S_A and σ_θ. The regression coefficients, a function of latitude, longitude and depth can be used, in combination with the altimeter signal, to reconstruct the sub-surface variability captured by the altimeter.

A substantial improvement of the signal to noise ratio suggests that when altimeter data are used in combination with in situ Argo float measurements, fewer observations are required to produce a stable estimate of time-averaged density field. Removing the eddy signal from the mean fields improves the scale separation of the mean and eddy fields.

2.6 Acknowledgments

This work was supported by NASA Headquarters under the NASA Earth and Space Science Fellowship Program - Grant NNX11AL55H. Additional support was provided by NSF awards OCE 06-22740 and OCE-1234473, and by NASA award NNX13AE44G. The altimeter products were produced by SSALTO/Duacs and distributed by Aviso, with support from CNES. Argo data were collected and made freely available by the International Argo Program and the national programs that contribute to it. The Argo Program is part of the Global Ocean Observing System.

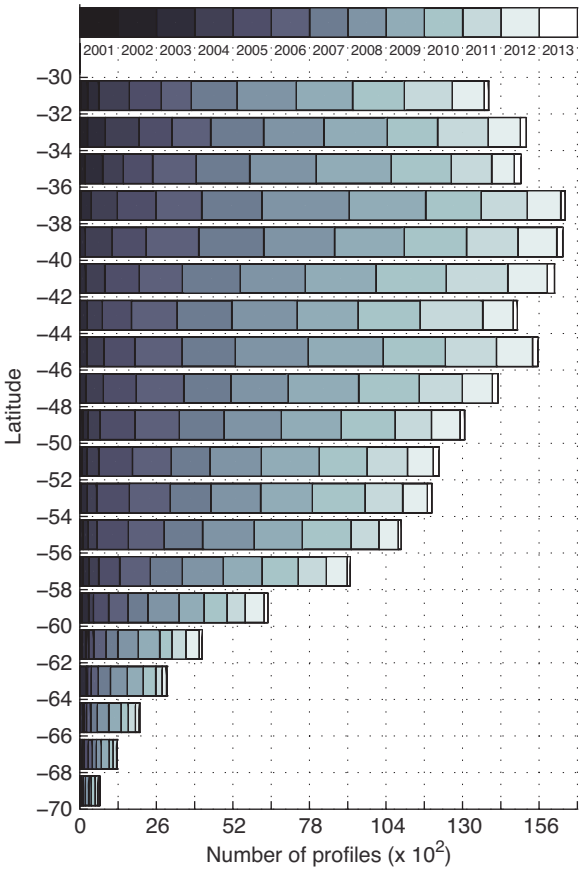

Figure 2.1: Meridional distribution of Argo profiles per year (2001-2013) averaged over 2° latitude bands (30°S - 70°S). Only quality-controlled Argo profiles are shown (see section 2.2.1).

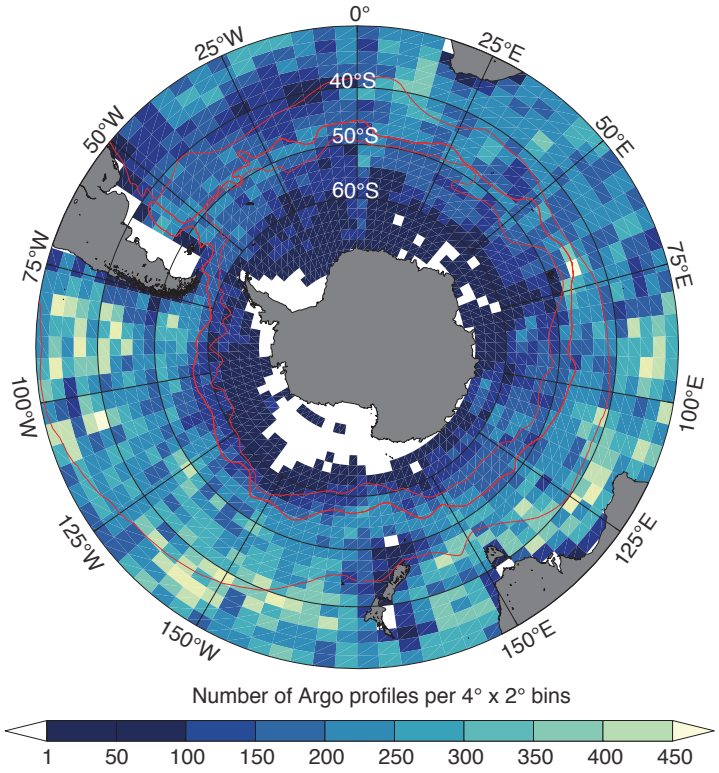

Figure 2.2: Horizontal distribution of Argo profiles per 4° zonal x 2° meridional bins for January 2001 to December 2013. Only quality-controlled Argo profiles are shown (see section 2.2.1). Climatological positions of fronts as defined by *Orsi et al.* (1995) are shown in red.

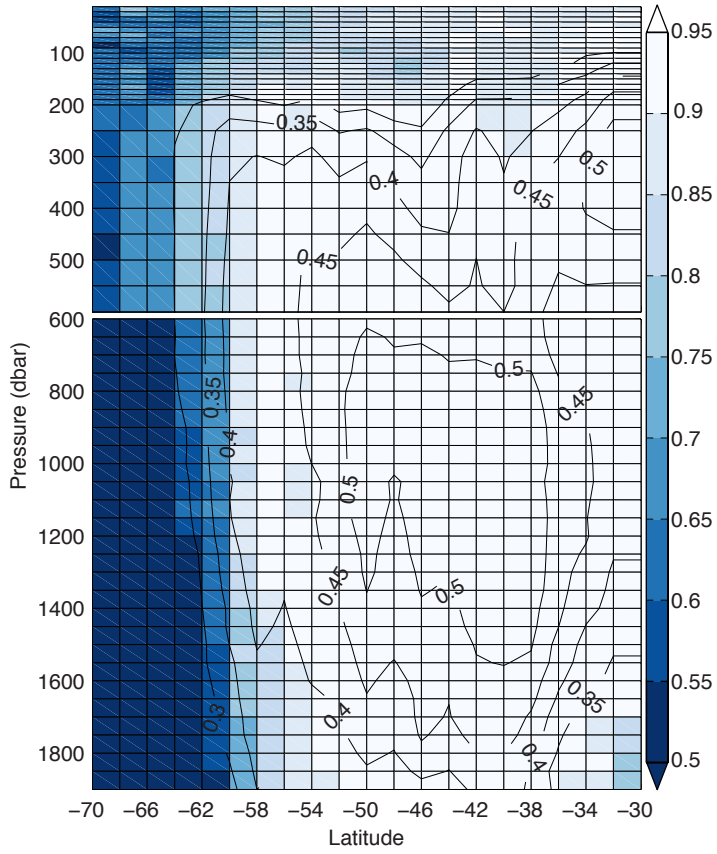

Figure 2.3: Regression between SSH' and σ'_θ. The colorscale shows the zonal average fraction of cells, per pressure level and 2° latitude bands, with regression coefficients statistically significant at the 95% level. Black contours show the fraction of variance explained by the altimeter.

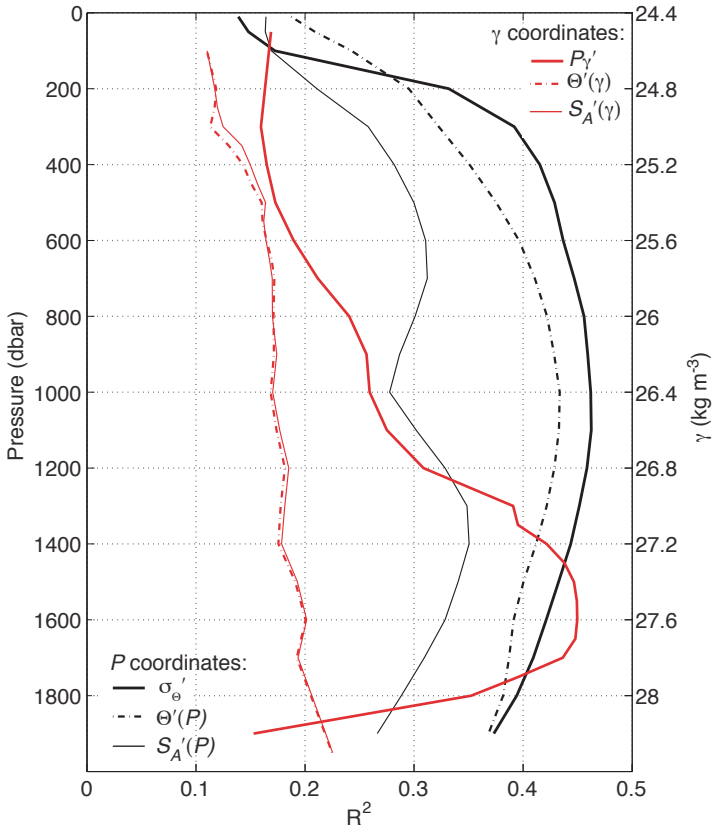

Figure 2.4: Domain averaged R^2 between SSH' and hydrographic variables in pressure level coordinates (black lines, left vertical axis) and neutral density level coordinates (red lines, right vertical axis): σ_θ' and P_γ' (solid lines), Θ' (dash-dot lines) and S_A' (thin solid lines).

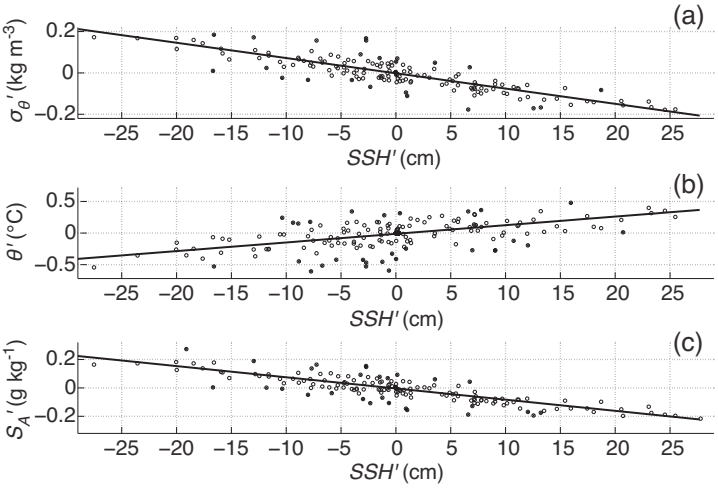

Figure 2.5: Example of linear regression between SSH' and σ'_Θ (a), Θ' (b) and S'_A (c) for a cell at 400 dbar located on the Southwest Atlantic region of the ACC (55°S, 45°W). Location is shown as a red dot in figure 2.6.

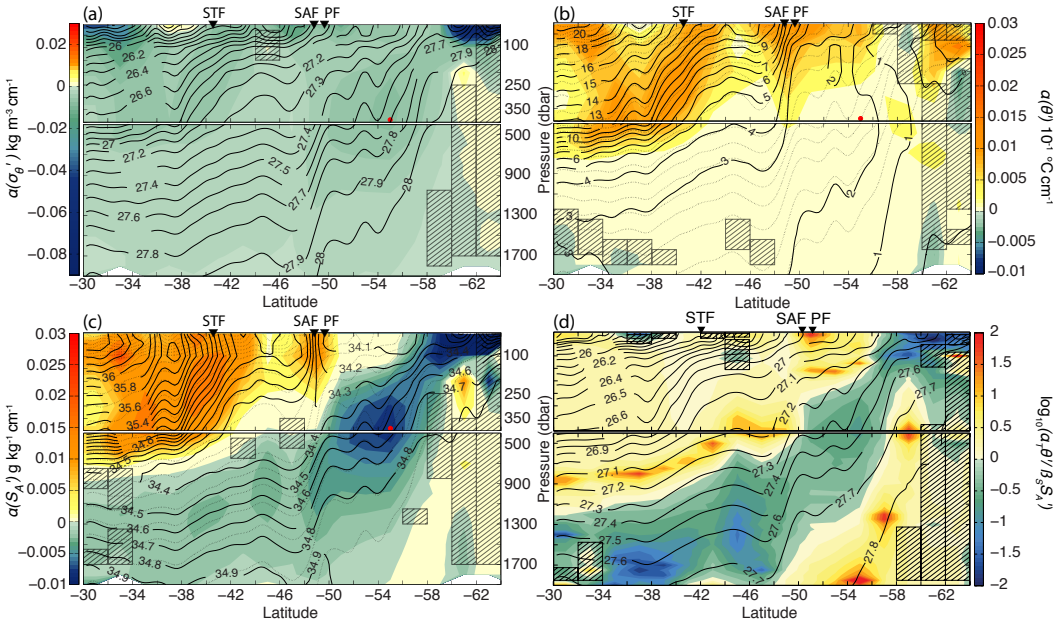

Figure 2.6: Meridional section in the southwest Atlantic sector of the Southern Ocean (45°W). (a)-(c): Linear regression slope between SSH' and σ'_θ (a), Θ' (b) and S'_A (c). (d): Relative contribution of salinity and temperature anomalies to density changes on pressure level coordinates. Location of mean neutral density surfaces is shown by black solid lines in (a) and (d), and dotted lines in (b) and (c). Mean temperature and salinity fields are denoted by black solid lines in (b) and (c) respectively. Climatological positions of fronts are marked by triangles at the surface. Hatched areas are not significant at the 95% level. Red dots show the location of the regression fit shown in figure 2.5.

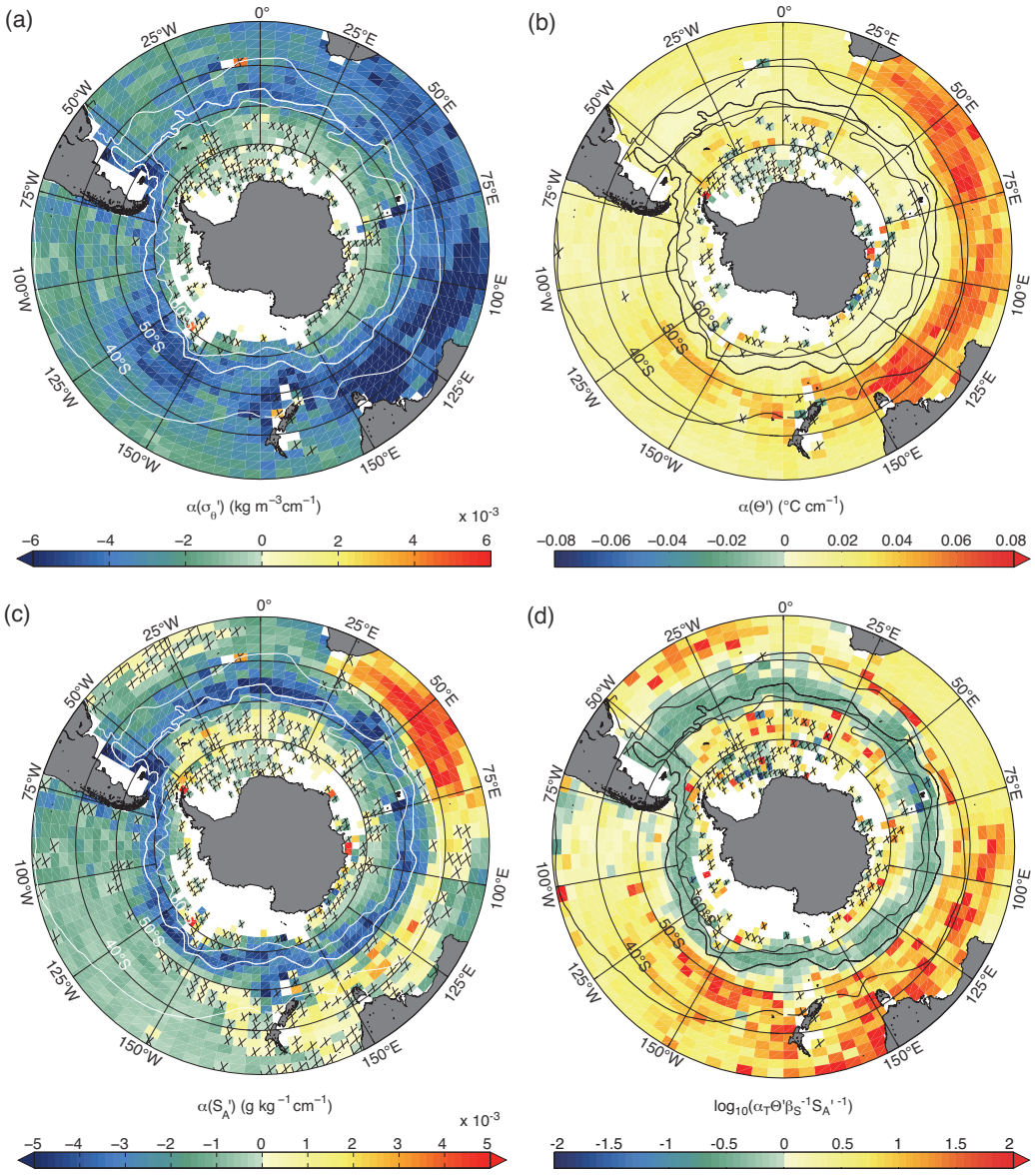

Figure 2.7: (a)-(c): Linear regression slope between SSH' and σ'_θ (a), Θ' (b) and S'_A (c) in 4° zonal x 2° meridional bins at 1000 dbar. Hatched bins are not significant at the 95% level. (d): Relative contribution of salinity and temperature anomalies to density changes on pressure level coordinates. Mean position of fronts as defined by *Orsi et al.* (1995) are shown in white for (a) and (c) and in black for (b) and (d).

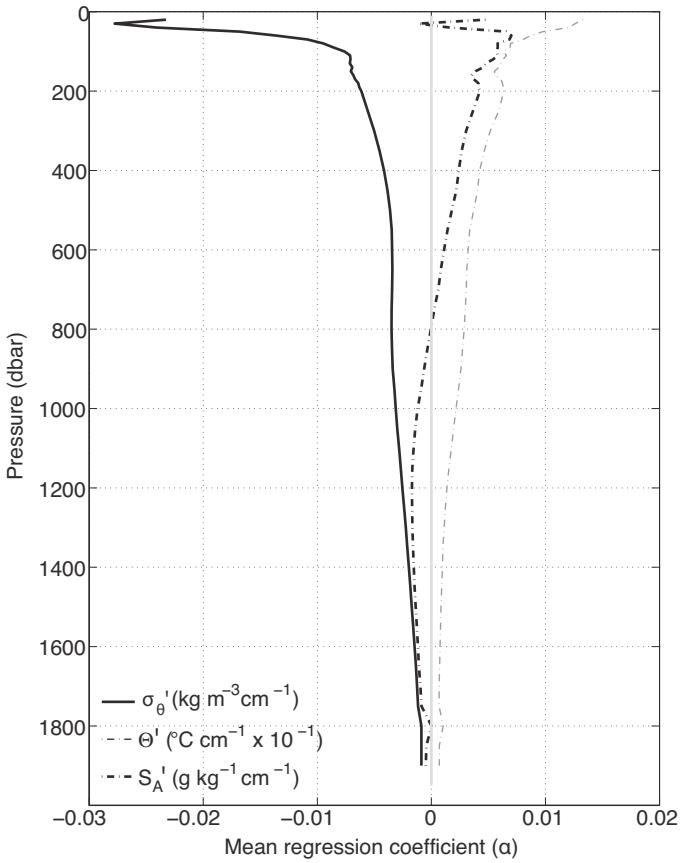

Figure 2.8: Spatially averaged regression slope (α) between SSH' and σ'_θ (black solid line), Θ' (black dash-dot line) and S'_A (gray dash-dot line) as a function of pressure.

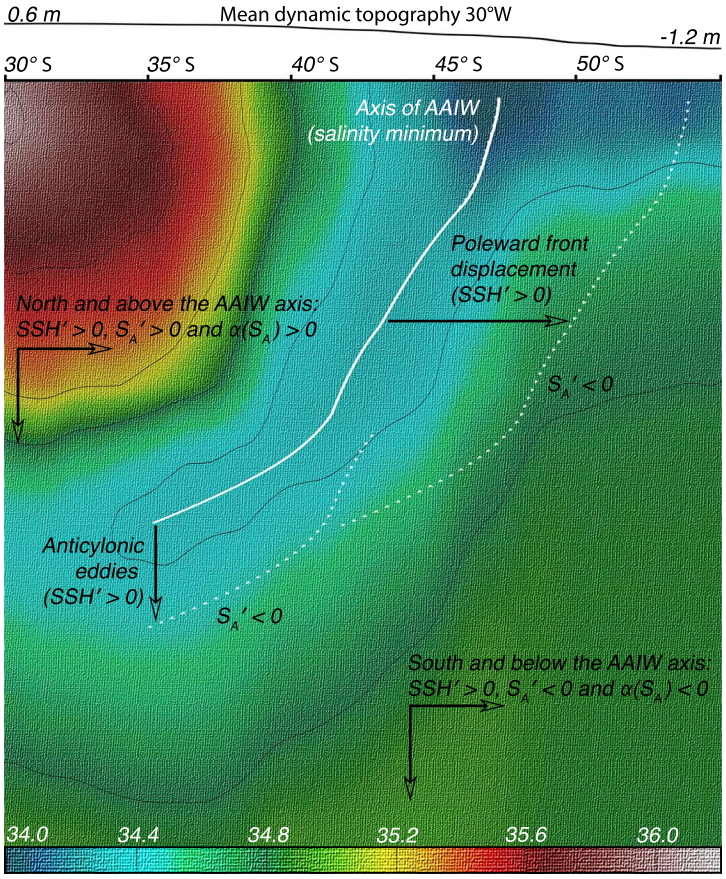

Figure 2.9: Schematic summarizing the impact of anticylonic eddies and poleward front displacements on the background salinity field. Figure shows a meridional section (30°W) of the mean S_A field. The position of the S_A minimum associated with AAIW is shown by the white solid line. Dash white lines and arrows depict the isohalines movement associated with anticyclonic eddies and poleward front displacements. For reference, the mean dynamic topography is shown by the solid black line at the top.

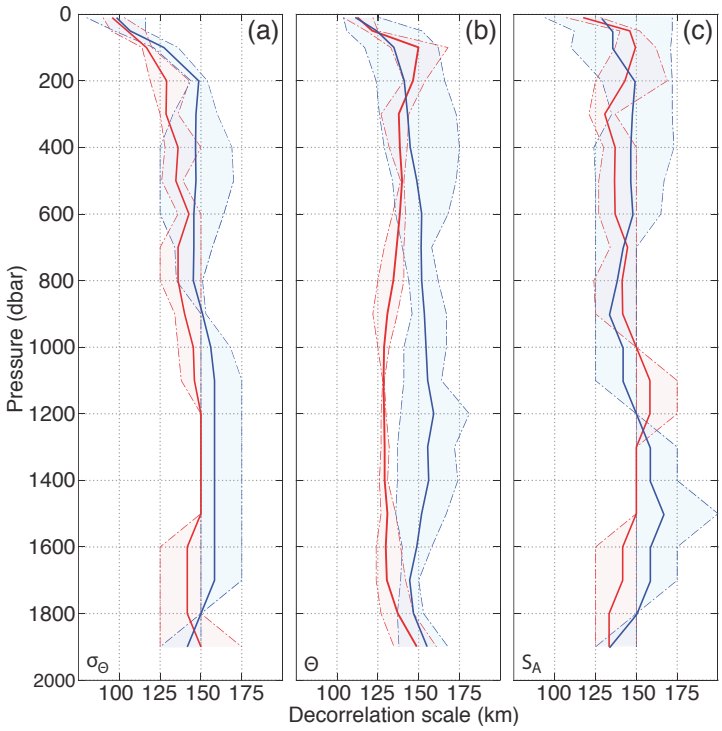

Figure 2.10: Spatially averaged zonal (solid red line) and meridional (solid blue line) decorrelation scales as a function of pressure for σ_Θ (a), Θ (b) and S_A (c). Shaded areas denoted the range of L values in all subdomains. Maximum and minimum zonal (red) and meridional (blue) L values found are shown by dash-dot lines.

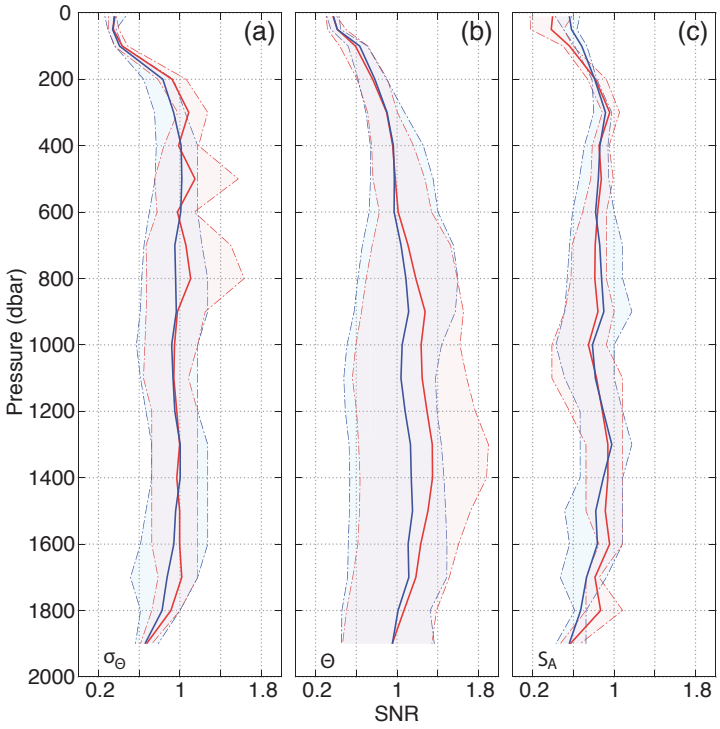

Figure 2.11: Spatially averaged zonal (solid red line) and meridional (solid blue line) SNR as a function of pressure for σ_Θ (a), Θ (b) and S_A (c). Shaded areas denoted the range of SNR values in all subdomains. Maximum and minimum zonal (red) and meridional (blue) SNR values found are shown by dash-dot lines.

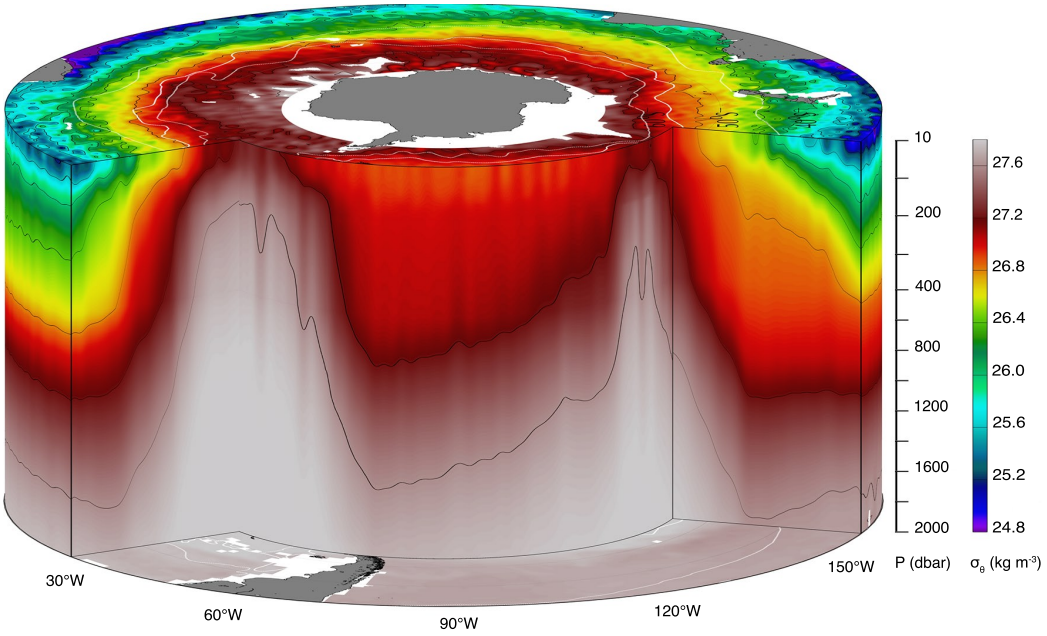

Figure 2.12: Three-dimensional view of the mean Potential Density field showing a vertical section of the Atlantic (30°W), Pacific (160°W) and a circumpolar section along 55°S. Vertical scale is stretched for the upper 400 dbar. Isopycnals are shown as black solid lines and climatological positions of fronts as defined by *Orsi et al.* (1995) are shown in white.

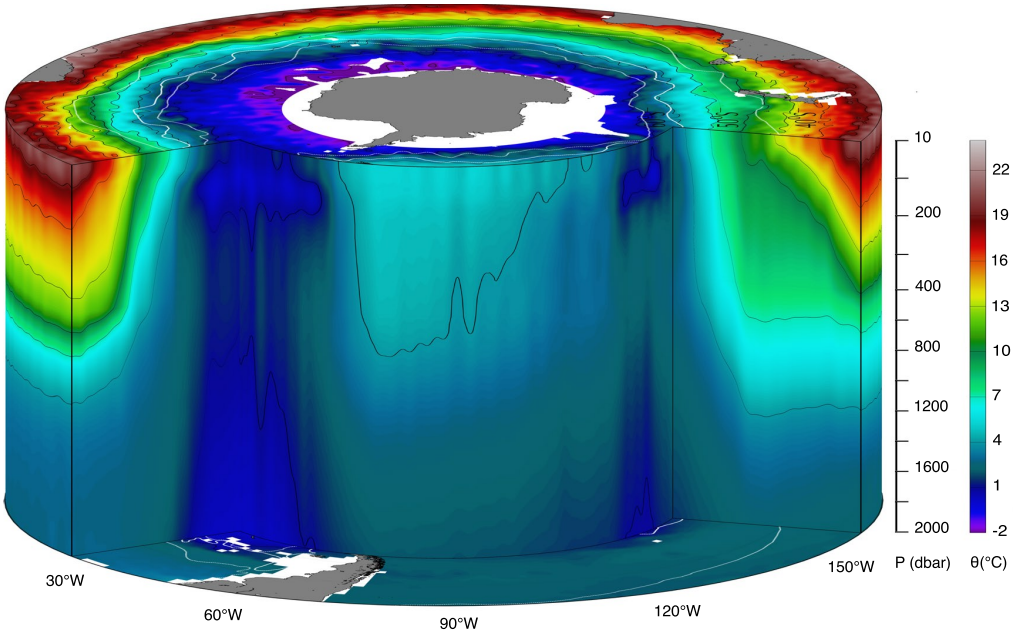

Figure 2.13: Three-dimensional view of the mean Conservative Temperature field showing a vertical section of the Atlantic (30°W), Pacific (160°W) and a circumpolar section along 55°S. Vertical scale is streched for the upper 400 dbar. Isotherms are shown as black solid lines and climatological positions of fronts as defined by *Orsi et al.* (1995) are shown in white.

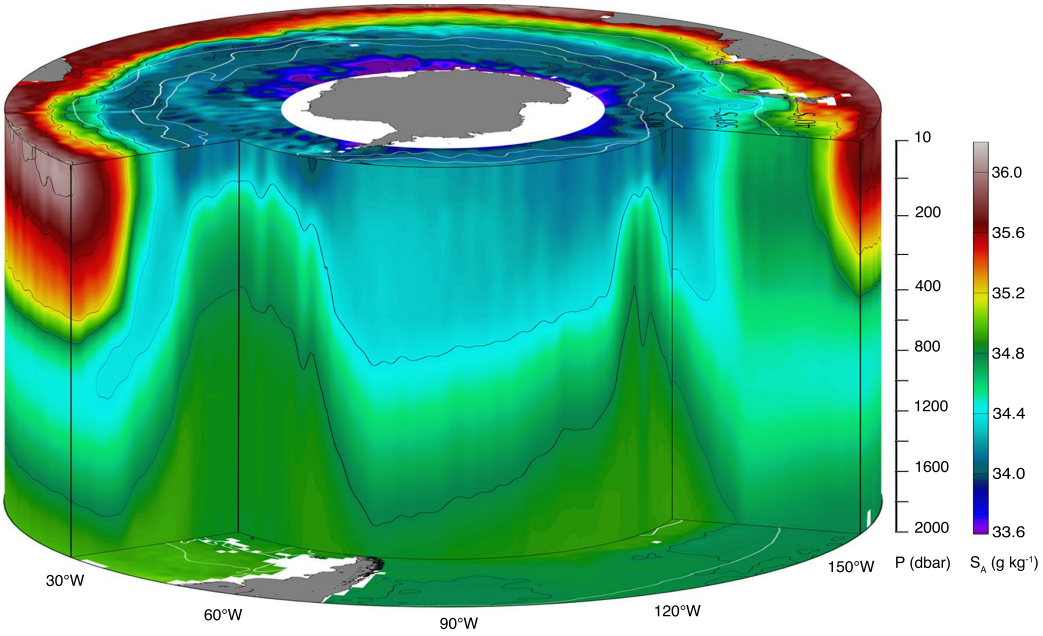

Figure 2.14: Three-dimensional view of the mean Absolute Salinity field showing a vertical section of the Atlantic (30°W), Pacific (160°W) and a circumpolar section along 55°S. Vertical scale is streched for the upper 400 dbar. Isohalines are shown as black solid lines and climatological positions of fronts as defined by *Orsi et al.* (1995) are shown in white.

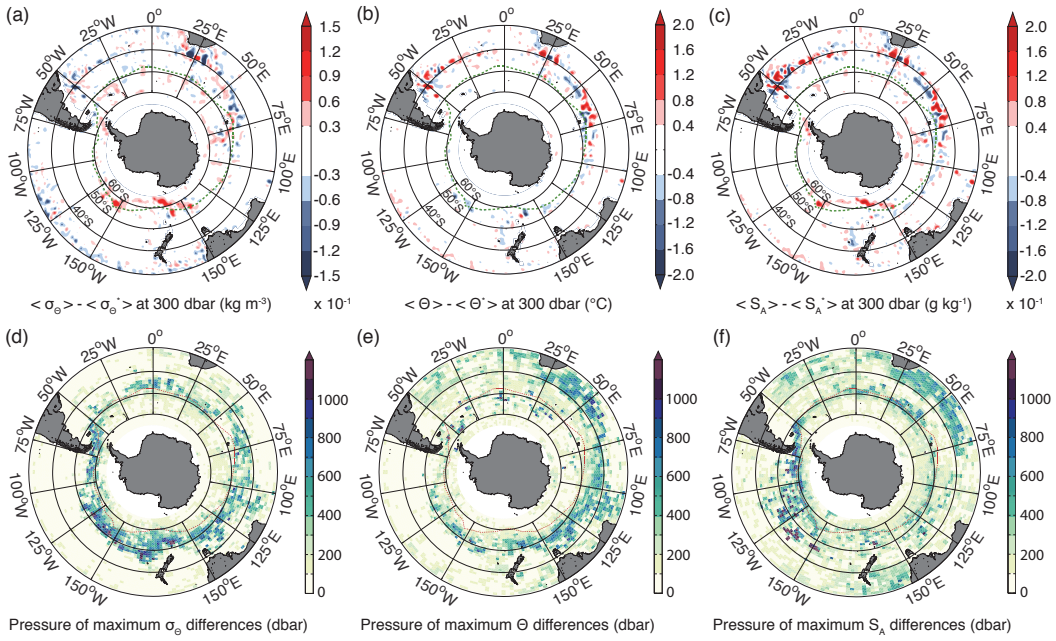

Figure 2.15: (a)-(c): Impact of removing the eddy signal on the mean fields at 300 dbar for σ_θ (a), Θ (b) and S_A (c). Variables without the altimeter signal are denoted by $\langle\ .^*\rangle$. (d)-(f): Pressure level of the maximum difference ($\langle\ .\ \rangle$ - $\langle\ .^*\ \rangle$) for σ_θ (d), Θ (e) and S_A (f) average over 2° longitude × 1° latitude bins. The dashed line encircling Antarctica marks the circumpolar path used in Figure 2.16.

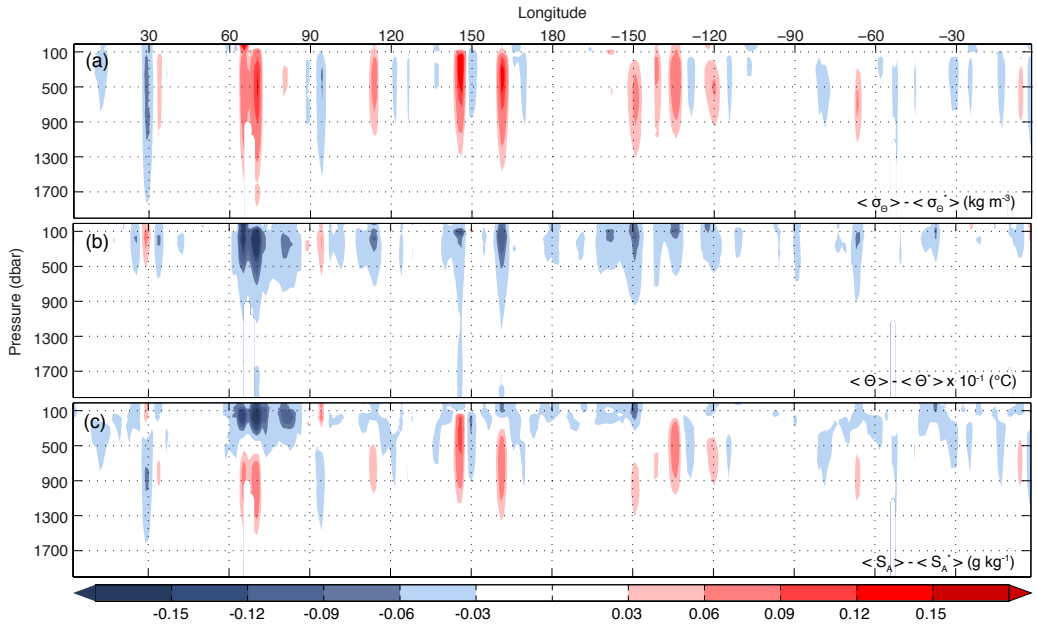

Figure 2.16: Circumpolar section of the difference between the mean fields computed from Argo floats with ($\langle\ .\ \rangle$) and without ($\langle\ .^*\ \rangle$) the altimeter signal for σ_θ (a), Θ (b) and S_A (c). The circumpolar path, denoted by the dashed line in Figure 2.15, lies between the SAF and the PF.

Chapter 3

Downgradient heat transport in the ACC due to reverse meridional eddy migration

Eddy motion in the Southern Ocean is studied using satellite altimetry and output from an assimilating numerical ocean model. Results show that the Southern Ocean has two distinct eddy motion regimes. North and south of the Antarctic Circumpolar Current (ACC), eddies propagate westward with a mean meridional drift directed poleward for cyclonic eddies (CEs) and equatorward for anticyclonic eddies (AEs). Eddies formed within the boundaries of the ACC have an effective eastward propagation with respect to the mean deep ACC flow, and the mean meridional drift is reversed, with warm-core AEs propagating poleward and cold-core CEs propagating equatorward. This circulation pattern of semi-coherent eddies in the ACC, drives downgradient eddy heat transport, which could potentially transport a significant fraction (24 to 60 $\times$ 10^{13} W) of the net poleward ACC eddy heat flux (30 to 70 $\times$ 10^{13} W, as inferred in previous studies).

3.1 Introduction

Satellite measurements of sea surface height (SSH) have allowed the systematic study of oceanic mesoscale variability on a global scale (e.g., *Zlotnicki et al.*,

1989; *Pascual et al.*, 2006). In particular, altimetric measurements (*Chelton et al.*, 2007) and numerical experiments (*Early et al.*, 2011) have shown that a significant fraction of the mesoscale variability observed with altimetry can be interpreted as semi-coherent or coherent vortices. These vortices, commonly referred to as eddies, propagate westward (e.g., *Chaigneau and Pizarro*, 2005; *Chelton et al.*, 2011). The westward propagation of eddies is well understood from theoretical grounds: regardless of their sense of rotation, eddies have a self-induced westward motion, which can be attributed to the planetary vorticity gradient (e.g., *Nof*, 1983).

Eddies also undergo a smaller secondary drift in the meridional direction. Irrespective of the hemisphere, cyclonic eddies (CEs) and anticyclonic eddies (AEs) have divergent meridional pathways: in most parts of the ocean, CEs are displaced poleward while AEs are displaced equatorward. This secondary drift has been documented in observational studies (e.g., *Morrow et al.*, 2004a; *Chelton et al.*, 2011) and numerical experiments (e.g., *Chassignet and Cushman-Roisin*, 1991). *Flierl* (1984) showed that in a quasi-geostrophic (QG) two-layer model the meridional displacement can be attributed to form drag on the lower layer. *Cushman-Roisin et al.* (1990) explained the meridional drift by invoking conservation of potential vorticity (PV) in the lower layer of a two-layer QG model.

The divergent meridional eddy pathways have consequences for the global meridional heat transport. Studies have shown that coherent eddies tend to result in upgradient heat transport (e.g., *Boebel et al.*, 2003; *Morrow et al.*, 2004b). The regions of the Southern Ocean containing the Antarctic Circumpolar Current (ACC) stand in stark contrast to most of the global ocean, with both the zonal and meridional displacements of eddies reversed. The eastward zonal displacement of eddies within the ACC has been shown in previous studies (e.g., *Chelton et al.*, 2011; *Klocker and Marshall*, 2014), and evidence of the reversed meridional displacement is presented in this work. The reversed displacement results in downgradient heat transport, a potentially significant component of the ACC heat budget that has not been addressed before in a direct manner.

In this study we present evidence showing that eddies formed within the boundaries of the ACC have a reverse meridional drift (CEs drift equatorward,

and AEs drift poleward) and an effective eastward propagation velocity relative to the mean deep eastward flow of the ACC. Several methodologies to automatically identify semi-coherent structures as seen from altimetry have been developed over the past decade (e.g., *Isern-Fontanet et al.*, 2003; *Chaigneau and Pizarro*, 2005; *Chelton et al.*, 2011). For this study we use the eddy identification and tracking procedure of *Chelton et al.* (2011). The identification is based on defining eddies as closed contours of SSH anomalies and finding the outermost closed contour of SSH. See Appendix B2 of *Chelton et al.* (2011) for a detailed description of the algorithm. This methodology was applied to 21 years (1992-2013) of gridded SSH' fields from the SSALTO/Duacs multi-mission altimeter products (*Ssalto/Duacs*, 2011). The resulting eddy displacements are presented in section 3.2. We use output from an assimilating model, the Southern Ocean State Estimate (SOSE) (*Mazloff et al.*, 2010), for the analysis of the eddy propagation velocities with respect to the mean ACC flow. Eddy propagation velocities were computed by applying the Radon Transform (*Radon*, 1917; *Dean*, 1983) to one-year-long Hovmöller diagrams of potential temperature anomalies (θ') from SOSE. The details of the calculation and results are presented in section 3.3. The implications of these findings for the meridional heat budget of the Southern Ocean are discussed in section 3.4. Finally, concluding remarks are presented in section 3.5.

3.2 Eddy displacement in the Southern Ocean

3.2.1 Zonal motion

The Southern Ocean is one of the few locations in the world ocean where eddies have a net eastward displacement (*Hughes et al.*, 1998; *Chelton et al.*, 2011). This occurs because the ACC advects eddies eastward, arresting the eddy self-induced westward propagation. In contrast, north and south of the ACC, eddy displacement is westward. For this study, eddies were identified and tracked following the *Chelton et al.* (2011) methodology. A threshold of 2 cm for the eddy amplitude was chosen to filter small amplitude eddies. In principle, eddies with smaller amplitudes could be identified; however, a 2-cm threshold was chosen to

avoid incorrect identification of mesoscale variability not associated with eddies (see Appendix B of *Chelton et al.* (2011)). The results presented in this section are not sensitive to the cut-off amplitude.

One way to summarize the zonal motion of eddies in the Southern Ocean is to map the net zonal displacement of eddies over their lifetimes as a function of the formation location. In this study, the formation location is used to indicate the first identification of eddies within the global gridded altimeter product, which provides mapped fields with an effective temporal resolution no better than 7 days (*Pascual et al.*, 2006). Hence the initial location of eddies, as seen from altimetry, is an approximation of the actual formation location. Figure 4.1a shows the ratio of the number of eddies with a net westward displacement versus eddies with a net eastward displacement, averaged in cells of 3° longitude × 1° latitude corresponding to the eddy initial locations. All along the ACC, 90 to 97% of the eddies have a net eastward displacement over their lifetimes (blue cells, with logarithmic ratios between -1.5 and -1). Eddies formed north and south of the boundaries of the ACC (red cells) show a net westward displacement over their lifetimes.

The analysis of the global eddy population shows a slight preference for CEs over AEs (*Chelton et al.*, 2011). This is also true in the Southern Ocean, with 2% more CEs than AEs. *Chelton et al.* (2011) found a dependence of eddy polarity with eddy lifetime, with more CEs with lifetimes of 60 weeks or less and more AEs with lifetimes over 72 weeks. We found that in the Southern Ocean this results holds north and south of the ACC jets. But the region of the Southern Ocean with strong eastward propagation has no clear dependence of eddy polarity with eddy lifetime.

3.2.2 Meridional motion

The meridional motion of eddies in the Southern Ocean depends on the formation location and sense of rotation. The relative displacements of all eddies formed south of 30°S (approximately 23,000 CEs and 22,000 AEs over the study period) were used to compute the average relative displacement for westward and eastward propagating eddies. Figure 4.1b summarizes displacements as a function

of time for anticyclones (red) and cyclones (blue). Eddies formed outside the ACC, travel westward and can generally be tracked for longer periods of time than eddies formed within the boundaries of the ACC. For AEs, the averaged trajectories are 23 months long for non-ACC eddies, and 18 months long for ACC-eddies. In the case of CEs, the averaged trajectories are 25 months long for non-ACC eddies, and 21 months long for ACC-eddies. The averaged trajectories shown in Figure 4.1b are composed of at least 100 individual eddy trajectories.

Eddies with a net westward displacement (formed outside the ACC) have a meridional drift that is directed poleward for CEs (red) and equatorward for AEs (blue). The mean meridional excursion ranges from 50 km for CEs to 200 km for AEs over the course of 18 months. In contrast, eddies formed in the ACC travel eastward with a reverse meridional drift (CEs drift equatorward, and AEs drift poleward) and have a mean meridional excursion of approximately 130 km (for both CEs and AEs) over 18 months. Interestingly, Figure 1b indicates that westward propagating CEs initially move equatorward before veering poleward, typically after 6 months and about 300 km of zonal displacement. This result seems to be consistent with the analysis of westward propagating eddies by *Chelton et al.* (2011). They found that irrespective of eddy polarity, eddy trajectories initially tend to rotate equatorward of due west with a median angle of 1.5°. This equatorward drift could result from the influence of ambient currents on eddy motions: *Chelton et al.* (2011) reported that the equatorward drift is more noticeable in eddies with large horizontal scales, which are likely to be more influenced by the background flow. Whether the source of the equatorward drift is the influence of the background flow or some other effect, overall it is negligible, as this drift is transient and small (less than 20 km) when compared to the total average poleward displacement of around 200 km.

The meridional displacement of eddies can be explained by invoking conservation of PV. This argument was used to explain the meridional displacement of westward propagating eddies in a two-layer QG model (*Cushman-Roisin et al.*, 1990). A schematic view of a westward propagating cyclonic eddy in the Southern Hemisphere is shown in Figure 3.2a. The surface is depressed with respect to the

mean surface position ($SSH' < 0$), and isopycnals inside the eddy are uplifted with respect to the surrounding fluid. This setup creates a local minimum of PV in the lower layers with respect to the ambient fluid surrounding the eddy. As the eddy propagates westward, the fluid in the lower layers is partially flushed and renewed by ambient fluid. Hence as fluid columns of relatively lower PV leave the eddy on its eastern flank, they are squeezed, and they acquire positive relative vorticity (ζ) in order to conserve PV. At the same time, fluid columns entering the eddy on its western flank are stretched and acquire negative ζ to compensate for changes in PV. The overall effect is that both on the western and eastern sides of the eddy, the local acquired ζ of the squeezed/stretched water columns, induces a poleward drift of the eddy core irrespective of the hemisphere.

Can the same mechanism based on PV conservation be used for eddies formed in the ACC? The answer is yes, as long as the zonal direction of propagation is reversed. A hypothetical eastward propagating anticyclonic eddy in the Southern Hemisphere (Figure 3.2b) would stretch fluid columns on the western flank of the eddy and squeeze fluid columns on the eastern flank. The acquired ζ due to PV conservation would induce a meridional drift directed poleward, in accordance with the observed eddy motion in the ACC. The satellite tracking of eddies shows that eddies formed within the boundaries of the ACC move eastward with respect to the bottom. However in order to invoke conservation of PV as in *Cushman-Roisin et al.* (1990), eddies need to be effectively propagating eastward with respect to the mean background ACC flow. This is certainly not the case near the surface, where the ACC mean speed exceeds 20 cm s^{-1} (e.g., *Sokolov and Rintoul*, 2009a). What remains to be seen is whether eddies propagate eastward with respect to the mean ACC flow at deeper levels. The next section discusses this possibility by examining eddy propagation velocities inferred from altimetry data and model output.

3.3 Eddy propagation velocity

Vortex velocity and displacement in the ocean have been studied under a range of different regimes (e.g., *McWilliams and Flierl*, 1979; *Nof*, 1983; *Cushman-Roisin et al.*, 1990; *Early et al.*, 2011). Ultimately the zonal speed of vortices in the ocean is intimately related to the speed of long planetary waves. *McWilliams and Flierl* (1979) showed that in highly idealized conditions (infinite domain, 1-layer reduced gravity model) both cyclonic and anticyclonic vortices propagate westward at the speed of linear Rossby waves. Deviations from the Rossby wave speed arise for finite-amplitude eddies. Under these conditions, the eddy amplitude affects the zonal speed: AEs move faster, and CEs move more slowly for increasing amplitudes (*Cushman-Roisin et al.*, 1990). Eddies in the ACC, however, propagate eastward with respect to the bottom of the ocean (Figure 4.1), and hence they do not seem to follow linear Rossby wave theory. Eddy zonal speed in the ACC and linear Rossby wave theory can be reconciled to a certain extent by recognizing that there is a Doppler shift due to the background flow. *Klocker and Marshall* (2014) showed that by Doppler-shifting the eddy zonal speed by the depth-mean flow of the ACC, they achieved a better agreement between observed eddy zonal speeds and linear Rossby wave theory.

In this work we estimate the eddy propagation velocity via two different methodologies. The tracking of closed SSH contours provides a direct estimation of the eddy propagation velocity, with the caveat that this approach is only formally valid near the surface. Previous studies have nevertheless used the surface expression as an estimate of the eddy velocity through the water column (e.g., *Klocker and Abernathey*, 2014). A complementary approach involves the use of θ' to track the eddy evolution in time. This is an indirect estimate of the eddy propagation velocity, since θ' propagation velocities can only be treated as a proxy for eddy velocities (as they also contain potential temperature fluctuations not associated with coherent eddies). However, this approach has the advantage of giving a complete picture of the velocity structure throughout the water column.

3.3.1 Altimeter-inferred surface eddy velocities

The average speed inferred from satellite eddy tracking (estimated from the mean eddy displacement in Figure 4.1b) ranges from 1.8 to 2.7 cm s^{-1} for westward propagating eddies and 0.9 to 2.5 cm s^{-1} for eastward propagating eddies. The smaller speeds for eastward propagating eddies are a consequence of two competing effects: the self-induced westward propagation and the eastward advection by the ACC. These speed ranges reflect the variability in the average eddy speed observed during the first 6 months of the eddy lifetimes. The larger speed values are observed during the first 4 weeks of the eddy lifetimes, with speed values converging to the lower end of the range at longer timescales. Speed estimates after 12 months tend to be more variable and outside of the speed ranges discussed above. The higher variability is most likely due to the fact that fewer eddy trajectories are available, and hence the average is less smooth. No significant speed differences between cyclonic and anticyclonic propagating eddies were detected. These results are in good agreement with past studies (e.g., *Klocker and Marshall*, 2014). A breakdown of the velocity by components reveals that the zonal component closely follows the average speed, while the meridional component is weaker (0.1 to 0.7 cm s^{-1}) and more variable with no asymptotic value at long timescales.

3.3.2 The vertical structure of the eddy velocities

To study the vertical structure of the eddy speeds we make use of SOSE, an assimilating, eddy-permitting, numerical model of the Southern Ocean (*Mazloff et al.*, 2010). SOSE has a horizontal resolution of 1/6° and 42 vertical levels of varying thickness. An ocean state estimate for the 2005 -2010 time period is available for use (http://sose.ucsd.edu). Numerous studies have made use of SOSE output to examine a wide range of ocean processes: for example, *Cerovečki et al.* (2011) analyzed optimized forcing fields, and *Firing et al.* (2011) analyzed the ACC velocity structure in Drake Passage. Here we use the SOSE potential temperature field to construct Hövmoller diagrams of daily θ'. Propagating features appear as striped patterns in Hövmoller diagrams. The angle of these patterns (Θ) is

related to the propagation speed (C), the spatial resolution (ΔX) and the time step (ΔT) of the sampling: $C = \Theta \times \Delta X \times \Delta T^{-1}$. To illustrate the propagation of Θ', figure 3.3 shows Hovmöller diagrams for a region of the eastern Pacific at 30°S (left column) and 55°S (right column). The direction of propagation (indicated by the dashed lines) reverses from west at 30°S to east at 55°S, no significant change in propagation speed with depth is detected. The implications of the vertical coherence of the propagation speed is discussed later in this section.

The Radon Transform (*Radon*, 1917; *Dean*, 1983), an automated procedure to find Θ, has been successfully applied to altimeter observations to estimate the phase speed of Rossby waves (e.g., *Chelton and Schlax*, 1996; *Polito and Cornillon*, 1997; *Lecointre et al.*, 2007) and eddy propagation speeds (*Chelton et al.*, 2011). To gain some insight into the vertical structure of the eddy velocity, we applied the Radon Transform to a year-long (2010) Hövmoller diagram of daily θ' from SOSE. Here θ' fields were filtered with a 3° zonal high-pass filter to remove low-frequency variability that could bias the eddy speed estimations (*Chelton et al.*, 2011).

The Radon Transform was applied to all vertical levels of SOSE along the circumpolar path denoted as a yellow line in Figure 4.1a. For each θ' value along the path, the Radon Transform was applied over a 10° longitude window centered at the value. Different window sizes were tested, and no significant variations were discerned in the speed estimates. The path closely follows the Subantarctic Front (SAF) in SOSE as defined by *Orsi et al.* (1995), except that the front was smoothed to ensure that the path is single-valued as a function of longitude.

The propagation speed of θ', as estimated by the Radon Transform, is shown in Figure 3.4a. Temperature anomalies can propagate as fast as 20 cm s^{-1} in regions with strong mean flow and eddy activity, such as downstream of Drake Passage, but in most regions the propagation speed lies between 2 to 4 cm s^{-1}. No significant variability is observed in the vertical, with surface propagating speeds extending to 2000 to 4000 m depth. This vertical coherence in the propagation speed of θ' suggests that eddy speeds estimated from the altimeter can be extended in the vertical. Evidence of increasing vertical coherence of propagation speeds with increasing non-linearity has been found by *Lecointre et al.* (2007). This is

consistent with the notion that propagating features in the Southern Ocean are likely to be associated to non-linear eddies, as previously suggested by *Chelton et al.* (2011) by computing different non-linearity parameters.

In contrast, the mean flow of the ACC (Figure 3.4b), also computed from SOSE and along the same circumpolar path, does not present the same vertical coherence: ACC jets reach deep levels, but the mean flow speed tends to be smaller than the eddy speed at sufficiently deep levels. For the case of the SAF, eddy propagation speeds exceed the mean flow speed below 3000 m depth almost everywhere along the path. This implies that along the circumpolar path there is a depth at which the eddy speed matches the mean flow speed (denoted by the boundary of the hatched area in Figures 4.1a and 4.1b). This level is commonly refereed to as the steering level (e.g., *Abernathey et al.*, 2010; *Ferrari and Nikurashin*, 2010; *Klocker et al.*, 2012). To illustrate the differences between the eddy propagation speed and the mean flow speed, Figure 3.4c shows the speed difference 200 m below the steering level. Almost everywhere along the circumpolar path, eddy speeds exceed the mean flow speeds by 1 to 2 cm s^{-1}. This suggests that eddies have an effective eastward propagation speed with respect to the mean ACC flow in the lower layers of the fluid. This effective eastward propagation explains the reverse in meridional displacement discussed in section 3.2.2.

3.4 Implications for the meridional heat transport

We have shown that coherent eddies in the Southern Ocean can propagate both eastward and westward, with eastward propagating eddies typically originating in the ACC. This effective eastward propagation has consequences for the meridional displacement of eddies: warm-core AEs drift poleward and cold-core CEs drift equatorward, opposite to what has been observed in other regions of the world ocean. Here we discuss the implications of this reverse meridional migration for the meridional heat budget in the Southern Ocean.

Eddies play an important role in the meridional heat transport of the ocean.

de Szoeke and Levine (1981) suggested that a poleward eddy heat flux of 45 ± 30 × 10^{13} W is needed to close the meridional heat budget south of the Polar Front. *Gille* (2003b) estimated a poleward eddy heat flux across the ACC of 30 ± 10 to 60 ± 10 × 10^{13} W using Lagrangian float observations. Other studies (*Keffer and Holloway*, 1988; *Stammer*, 1998; *Sloyan and Rintoul*, 2000) also reported poleward eddy fluxes in the ACC within the 30 to 70 × 10^{13} W range. These estimates are all based on the traditional definition of eddy fluctuations as departures from a mean state. Here we explore how much of that eddy heat flux could be associated with coherent eddies.

The eddy heat contained by a single coherent eddy is defined as $Q_e = \int_V T' C_p \rho \, dV$. Where T' is the temperature anomaly, C_p is the heat capacity of sea water at constant pressure and ρ is the density of sea water. The total heat transport due to the coherent eddy field can then be estimated as $Q = \langle \sum_N Q_e \rangle$, where N is the total number of eddies during the observation period and $\langle \cdot \rangle$ is the time average over that period. The total eddy heat transport Q can be approximated by simplifying the geometry of the eddies to a cylindrical shape ($Q \approx \langle T' C_p \rho R_e^2 \pi H_e N \rangle$), and assuming typical values for T', the eddy radius (R_e) and the eddy height (H_e). An average of 1120 (N) eastward propagating AEs per year were identified during the study period, with an average radius R_e of 35 km. Figure 3.4a shows that eddies along the SAF can go as deep as 3500 m, but the temperature signal at those levels is small ($\theta' < 0.03$°C), therefore an eddy height (H_e) of 2500 m was chosen as representative of eddies in the vicinity of the SAF. Finally T' is perhaps the most challenging parameter to estimate. The analysis of SOSE temperature anomalies associated with propagating features shows that the signal can range from 1 to 1.5°C at the surface and decreases rapidly with depth, reaching values of 0.05°C or less at 2500 m depth. Hence a characteristic value for T' depends how T' decays with depth and away from the center of the eddy. Q varies from 24 × 10^{13} W if $T' = 0.2$°C, to 60 × 10^{13} W if $T' = 0.5$°C. This idealized calculation suggests that the eddy heat carried by coherent eddies could be a significant fraction of the total poleward eddy heat flux inferred from observations in the ACC (30 to 70 × 10^{13} W).

3.5 Final remarks

In most regions of the world ocean eddies propagate westward and drive upgradient heat transport, but in the ACC both of these traits are reversed. We explain this from theoretical grounds by invoking conservation of PV and hypothesizing an effective eastward propagation of coherent eddies with respect to the mean ACC flow. Evidence of the latter is supported by the analysis of T' propagation speeds from an ocean state estimate model of the Southern Ocean. The presence of eastward propagating eddies with downgradient heat transport is potentially a key component to the meridional heat budget of the Southern Ocean. An idealized calculation suggests that a significant fraction of the poleward eddy heat flux could be transported by coherent eddies.

3.6 Acknowledgments

This work was supported by NASA Headquarters under the NASA Earth and Space Science Fellowship Program - Grant NNX11AL55H. Additional support was provided by NSF awards OCE 06-22740 and OCE-1234473, and by NASA award NNX13AE44G. The altimeter products were produced by SSALTO/Duacs and distributed by Aviso, with support from CNES. Computational resources for the SOSE were provided by NSF XSEDE resource grant OCE130007 and NSF grant PLR-1425989. SOSE was produced using the Extreme Science and Engineering Discovery Environment (XSEDE), which is supported by National Science Foundation grant number MCA06N007.

Chapter 3 is currently being prepared for submission for publication of the material to Geophysical Research Letters. Zajaczkovski, U.; Gille, Sarah T.; Mazloff, Matthew R. The dissertation author was the primary investigator and author of this paper.

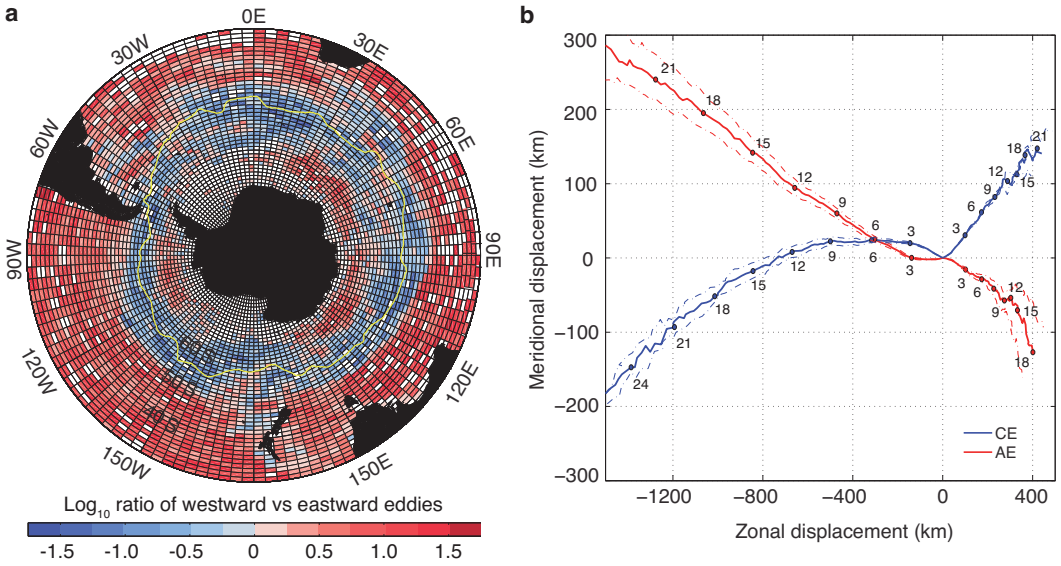

Figure 3.1: Geographical distribution of eddies and their relative displacements. (a) Ratio of the number of eddies with a net westward longitudinal displacement versus eddies with a net eastward longitudinal displacement averaged in 3° longitude × 1° latitude bins, with eddies identified geographically by their initial location. A logarithmic scale is used for the color bar in order to emphasize equally the ratios r and $1/r$. The yellow line denotes the circumpolar path used in Figure 3.4. (b) Average relative displacement of anticyclonic eddies (solid red) and cyclonic eddies (solid blue). Blue and red dots and associated numbers denote the time evolution in months of cyclonic and anticyclonic eddies respectively. Averages are composed with at least 100 trajectories. Standard error is shown as thin dash-dot lines assuming that 50% of the eddy trajectories are statistically independent.

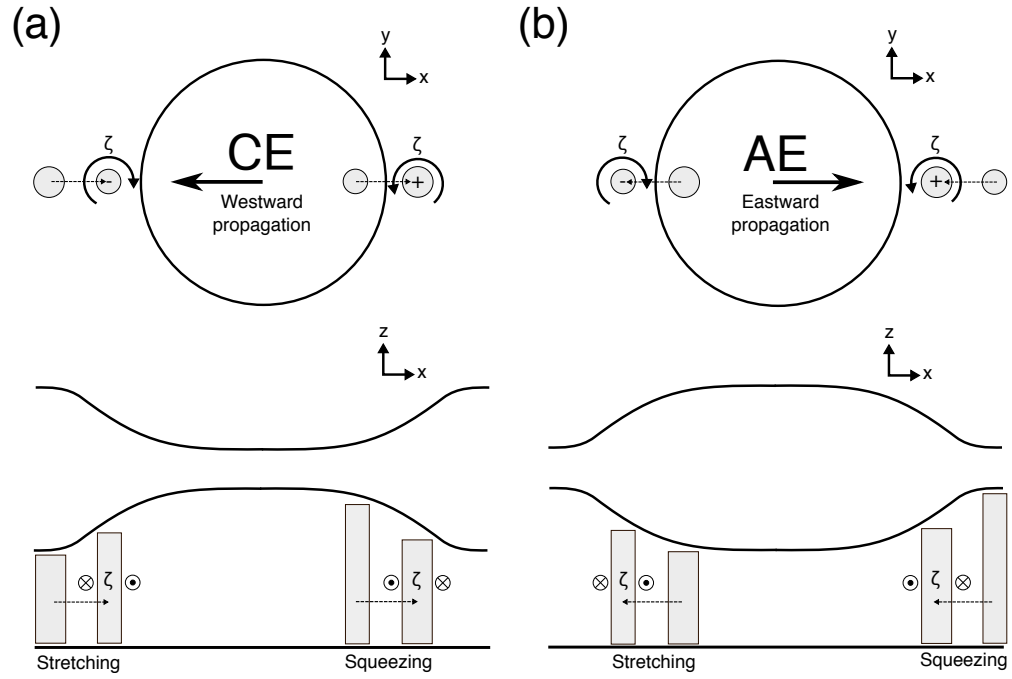

Figure 3.2: Schematic diagram of the induced meridional motion of eddies due to conservation of potential vorticity adapted from *Cushman-Roisin et al.* (1990). (a) Westward propagating cyclonic eddy in the Southern Hemisphere and the induced relative vorticity. In both hemispheres the induced meridional motion for cylonic westward propagating eddies is poleward. (b) Same for an eastward propagating anticyclonic eddy formed in the ACC. See section 3.2.2 for a discussion of the figure.

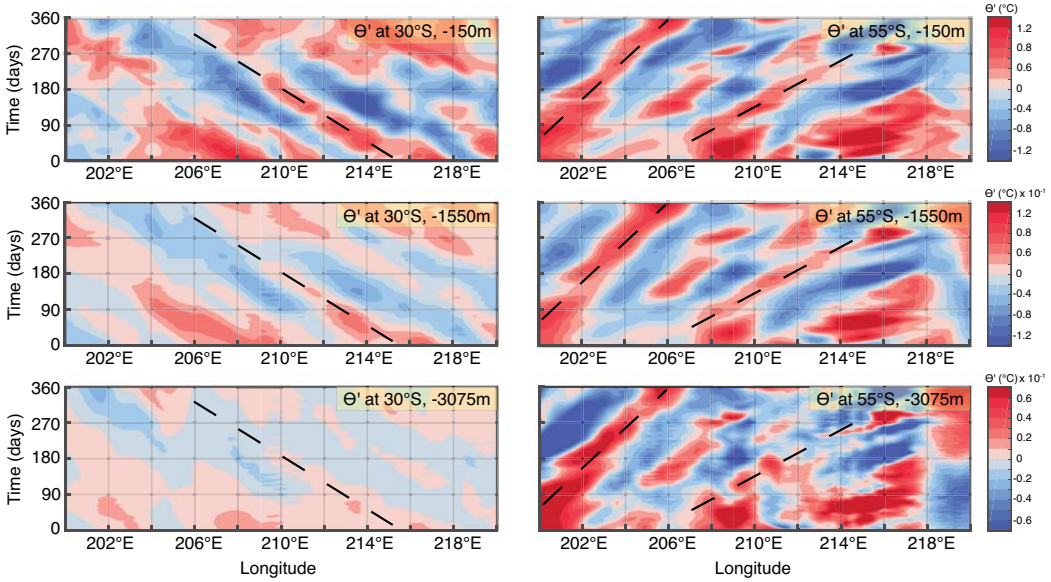

Figure 3.3: One-year-long Hovmöller diagrams (2010) of θ' from SOSE at 30°S (left column) and 55°S (right column) for three different depths: 150m (top), 1550m (center) and 3075m (bottom). Slope of black dashed lines indicate approximate propagation speeds.

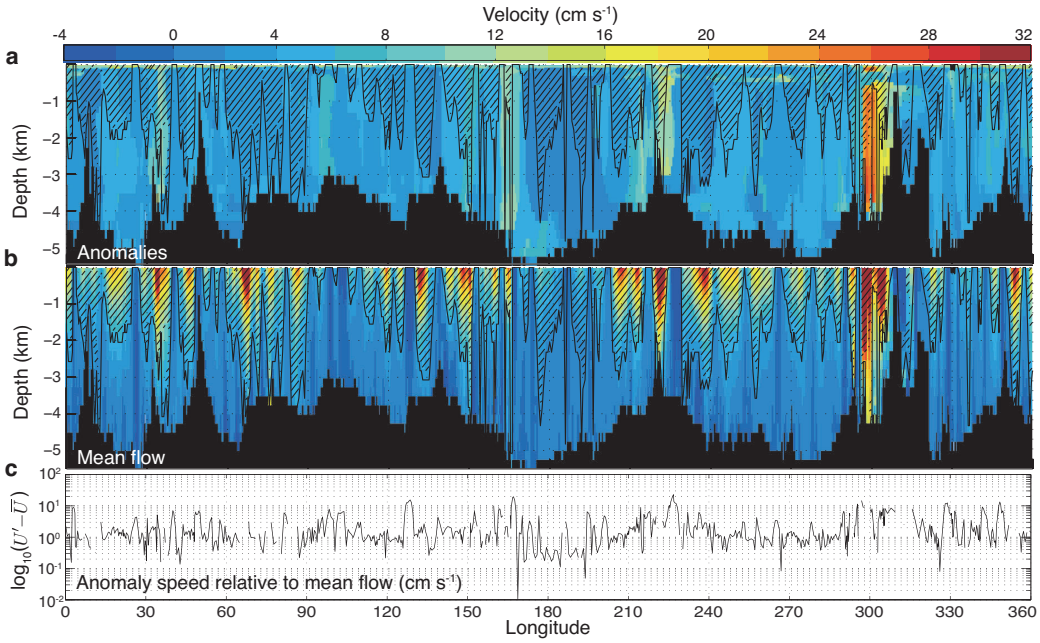

Figure 3.4: Comparison of anomalies (a) and mean flow (b) speed along the circumpolar path denoted in Figure 4.1a. Hatched areas denote locations where the mean flow speed is greater than the anomalies speed. Lower boundary of the hatched areas denotes the level of the steering level, where mean flow speed matches anomaly speed. (c) Anomaly speed relative to the mean flow speed 200 m below the steering level.

Chapter 4

Eddy generation and decay in the Southern Ocean

The Southern Ocean features high eddy kinetic energy, identifiable in satellite altimetry along the entire length of the Antarctic Circumpolar Current. However, analysis of altimeter data and an ocean state estimate show that the generation of relatively large amplitude eddies is not a ubiquitous feature of the Southern Ocean but rather a phenomenon that is constrained to five isolated, well-defined "hotspots". These hotspots, identified using altimeter data, are located downstream of major topographic features, with their boundaries closely following f/H contours. Eddies generated in these locations show no evidence of a bias in polarity and decay within the boundaries of the generation area rather than propagating. Eddies tend to disperse along f/H contours rather than following lines of latitude (or f). A state estimate shows enhanced values of both buoyancy and shear production inside the hotspots, with buoyancy production one order of magnitude larger than shear production. This is consistent with baroclinic instability being the main mechanism of eddy generation. The mean potential density field estimated from Argo floats shows that inside the hotspots, isopycnal slopes are steep, indicating availability of potential energy and providing further evidence of the main generation mechanism. The hotspots identified in this chapter overlap with previously identified regions of standing meanders. We provide evidence that hotspot locations can be explained by the combined effect of topographic features,

standing meanders that enhance baroclinic instability, and availability of potential energy to generate eddies via baroclinic instabilities.

4.1 Introduction

Mesoscale eddies, ubiquitous features of the world ocean, play a fundamental role in the Southern Ocean. The strength of the meridional overturning circulation (MOC) is in part set by eddies (e.g., *Marshall and Radko*, 2003). Eddies also provide a link between the momentum and buoyancy budgets (*Hallberg and Gnanadesikan*, 2006), thus playing a key role in the dynamics of the Southern Ocean. Due to its circumpolar geometry, the Southern Ocean is particularly well suited for zonally-averaged studies. The zonally averaged framework was successfully applied to study average properties of the MOC (e.g., *Olbers and Visbeck*, 2005; *Nikurashin and Vallis*, 2011). However, the zonally averaged approach has limitations and can hide important local dynamics. This is particularly true in regions of the Southern Ocean with prominent topographic features. *Thompson and Salle* (2012) showed that zonal asymmetries in the topography can impact the global flow structure and transport properties of the Antarctic Circumpolar Current (ACC). Eddy kinetic energy (EKE) variations along the ACC are also related to topographic features (e.g. *Sokolov and Rintoul*, 2009a). Evidence of enhanced eddy mixing due to the interaction of ACC jets and topographic features was found by *Lu and Speer* (2010). The geographical distribution of productivity is also influenced by topography: *Sokolov and Rintoul* (2007), found persistent blooms of chlorophyll downstream of islands and bathymetric features. These studies show the significant role of zonal asymmetries in setting distinct local dynamics that alter the ACC structure and transport properties.

In the Southern Ocean, mesoscale eddies are thought to arise by the interaction of the multiple jets embedded in the ACC either via barotropic instability or via instabilities in the vertical mean shear, i.e. baroclinic instabilities (e.g., *Treguier et al.*, 2007). A significant part of the energy extracted from the mean state by the baroclinic eddies is believed to contribute to bottom-enhanced diapycnal mixing

over regions of rough topography (*Marshall and Plumb*, 2008). Although the details of how energy is extracted from the eddies are still a subject of open debate, a primary candidate is the generation of lee waves over topographic features (e.g., *Chapman and Haidvogel*, 1993; *Aguilar and Sutherland*, 2006; *Nikurashin and Vallis*, 2012). In the Southern Ocean, this conjecture is supported by observational evidence, which shows that dissipation estimates are higher over rough topography (e.g., *Naveira Garabato et al.*, 2004; *St. Laurent et al.*, 2012; *Whalen et al.*, 2012). Observational and modeling studies also suggest that eddies can interact with topographic features (e.g., *Treguier et al.*, 2007).

The term "eddy" is used in the literature with widely different meanings (e.g., *Nof*, 1983; *Fu*, 2006; *Morrow et al.*, 2010). In this study we will refer to eddies as semi-coherent vortices. Vortices are usually thought of as isolated regions of high vorticity, but an unambiguous identification of a vortex is not trivial. In the ocean, attempts to identify semi-coherent structures include the use of sea surface height (SSH), geostrophic velocity, relative vorticity, or variables derived from these quantities to isolate rotating structures with closed shapes. A summary of these methodologies can be found in Appendix B1 of *Chelton et al.* (2011). Most of these methodologies were applied to altimeter measurements to identify eddies in the world ocean (e.g., *Isern-Fontanet et al.*, 2003; *Chaigneau and Pizarro*, 2005; *Chelton et al.*, 2011). These approaches, though relatively simple to implement, are subject to threshold parameters and are frame-dependent (*Haller*, 2005). A frame independent approach is more appropriate in cases where the ability of vortices to act as transport barriers is important. Attempts to overcome these limitations and to unambiguously define vortices can be found in the literature (e.g., *Haller and Yuan*, 2000; *Haller*, 2005; *Bremer et al.*, 2015). Some of these definitions were applied to the ocean: for example *Beron-Vera et al.* (2008) used Lagrangian coherent structures (LCSs) defined from finite-time Lyapunov exponent fields to identify vortices in the global ocean.

A number of parameters have been proposed to measure the non-linearity of eddies (e.g., *Chelton et al.*, 2011). In particular, the ratio of the rotational speed to the translation speed, U/c, can be regarded as a measure of the efficiency

with which a vortex can trap fluid. *Samelson* (1992) showed that for Gaussian eddies, $U/c > 1$ implies that the vortex traps fluid that is advected as the vortex translates. However, if U/c is derived from a frame-dependent definition of vortices, then the non-linearity does not necessarily imply that the vortex is effectively trapping fluid (e.g., *Beron-Vera et al.*, 2013). For the purposes of this study, the distinction between semi-coherent vortices defined via a frame-dependent method, such as closed SSH contours, or LCS is not crucial, as our results do not rely on fluid trapped by vortices. Nevertheless, the Southern Ocean has a relatively high population of non-linear vortices as measured by the U/c ratio, which ranges from 8 to 10, among the highest found in the global ocean (*Chelton et al.*, 2011).

Motivated by previous studies (*Sokolov and Rintoul*, 2009a; *Lu and Speer*, 2010; *Thompson and Salle*, 2012) that emphasized the significant role of zonal asymmetries and the role of eddies in the energy budget and transport of properties, this study aims to characterize the geographic distribution of the eddy population and its energy sources. In particular we focus on the spatial distribution of generation and decay locations, and their relation with topographic features. We present additional evidence of the close relation between prominent topographic features and high eddy activity. As we will show, eddy generation is spatially inhomogeneous. We elucidate this phenomenon by examining the relationship between the baroclinic structure of the background flow, the major topographic features of the Southern Ocean, and the wind stress field. We use satellite observations to track the mesoscale eddy field. The energy sources are examined using output from numerical simulations. Argo floats are used to study the baroclinic structure of the background flow, and to support the conclusions drawn from the numerical model.

The chapter is organized as follows. Section 4.2 discusses the eddy identification methodology and presents the geographical distribution of eddy generation and decay. The relation of the generation and decay regions with topographic features is discussed in section 4.3. The analysis of eddy trajectories, their relative displacements, and an overview of the statistical properties is given in section 4.4. The eddy energy sources and their associated instability processes are discussed in

section 4.5. An attempt to relate eddy generation locations, topographic features and energy sources is presented in section 4.6. Finally conclusions are presented in section 4.7.

4.2 Geographical distribution of eddy generation and decay

The identification and tracking procedure used in this study is based on defining eddies as closed contours of sea surface height anomalies (SSH′) and finding the outermost closed contour of SSH′. The details of the method and a description of the algorithm can be found in Appendix B2 of *Chelton et al.* (2011). The SSH fields were smoothed with a Gaussian high-pass filter to remove variability with scales larger than 20° in the longitudinal direction and 10° in the latitudinal direction. This large-scale variability, not associated with eddies, is mainly due to steric effects (e.g., *Roemmich and Gilson*, 2009). The eddy identification procedure was applied to 21 years (1992-2012) of gridded weekly SSH′ fields from the SSALTO/Duacs multi-mission altimeter products (*Ssalto/Duacs*, 2011). Our results were compared to the *Chelton et al.* (2011) dataset version 3, which is available at http://wombat.coas.oregonstate.edu/eddies_May2013/. Rare differences were found for cases for which the automated algorithm failed and a human judgment was required. Overall no significant differences between the two datasets were found.

In this work we focus on large amplitude eddies, which are likely to have a larger impact than small eddies on eddy-driven dynamics (e.g., *Gill et al.*, 1974). The eddy amplitude is defined as the difference between the large-scale ambient SSH outside the eddy boundary and the maximum absolute value inside the eddy. Eddy amplitudes defined this way are smaller than eddy amplitudes referenced to the time-mean SSH. An eddy amplitude threshold of 4 cm was chosen to screen out small amplitude eddies. Eddies that do not reach at least 4 cm in amplitude at any given stage of their lifetimes are removed. This threshold, at least twice the noise level of the merged altimeter product, which can range from 1 to 1.5 cm

depending on the location (*Ssalto/Duacs*, 2011), prevents incorrect identification of mesoscale variability not associated with eddies. Incorrect identification could be a significant issue for eddies with amplitudes of 1 cm or less (see Appendix B of *Chelton et al.*, 2011).

For the purposes of this study, the Southern Ocean is defined as the region of the world ocean south of 30°S. The analysis is limited to the region north of 65°S due to the limited availability of altimetry measurements south of that latitude. Fig. 4.1a shows the initial centroid locations of eddies, i.e. the locations where closed SSH′ contours are spotted for the first time, summed in bins of 4° longitude × 2° latitude. The average speed of eddies rarely surpasses 10 cm s^{-1} as was shown by past studies (e.g., *Fu*, 2009; *Chelton et al.*, 2011), and corroborated in this thesis (section 4.4.2). An eddy displacing at 10 cm s^{-1} could travel up to 60 km before it shows up in the weekly mapped SSH′ field as a closed contour. Inherent errors in the mapped SSH′ fields also propagate into errors of the centroid locations. *Pascual et al.* (2006) showed an example of a cyclonic eddy in the Gulf Stream which captured a surface float. The absolute dynamic topography derived from two satellites fails to reproduce the centroid location, while the SSH field derived from four satellites is in better agreement. The error in the initial location does not affect the results presented in this chapter, which focus on the broad areas of high eddy generation. These regions are well-defined, non-overlapping areas separated from each other by several degrees in longitude.

Fig. 4.1a shows that the geographical distribution of eddy generation is highly heterogeneous, with regions of the Southern Ocean with no identifiable eddy generation (blank spaces north of 65°S) and regions of high eddy generation, with several regions surpassing 40 eddies per bin for the 21 years of the analysis. Three of these regions are located north of the ACC and are associated with boundary currents: (1) the Brazil Current, the Falkland/Malvinas Current and the Brazil-Malvinas Confluence region in the western South Atlantic (region labeled as BMC in Fig. 4.1), (2) the East Australia Current in the Western Pacific (EAC in Fig. 4.1), and (3) the Agulhas re-circulation region in the boundary between the Indian and Atlantic Ocean (ARR in Fig. 4.1). The remaining regions are located

within the boundaries of the ACC, and in the next section we will show that these areas of high eddy generation are associated with major topographic features of the Southern Ocean. These areas are robust and persist if the eddy amplitude threshold of 4 cm is lowered. However, with a lower threshold their boundaries are less distinguishable, and eddy generation is detected in regions with no generation of large eddies. This raises the interesting question of why eddies with relatively large amplitudes are constrained to isolated regions in the Southern Ocean.

The analysis of eddy trajectories shows that eddies generated within the areas of high eddy generation do not propagate far, and the majority decay in the vicinity of these areas. The mean distance travelled by eddies is 350 ± 340 km, the median distance is 250 km, and the e-folding scale for the lifetime distribution is 9 weeks as it will be shown in section 4.4b. Fig. 4.1b shows the final centroid locations of eddies, i.e. the positions where closed SSH$'$ contours are spotted for the last time, summed in bins of 4° longitude $\times$ 2° latitude. A striking resemblance of the high eddy generation and decay areas can be seen by comparing Fig. 4.1a and 4.1b. Our goal is to relate these areas to topographic features and dynamic processes. Thus a consistent way to define their boundaries is needed. Region boundaries could be defined in a number of ways, including for example, by the outer boundaries of the bins with 40 or mores eddies. Here we choose to estimate the probability density function (PDF) of eddy generation and decay using a multivariate kernel density estimation (KDE). KDE is a non-parametric method to estimate the PDF of a random variable (e.g., *Simonoff*, 1996). The two key components are the kernel function $K(\mathbf{x})$ and the bandwidth matrix $\mathbf{H}$. K is commonly defined as the normal distribution, and the degree of smoothing is controlled by $\mathbf{H}$. A comprehensive review of different KDE methods can be found in the literature (e.g., *Simonoff*, 1996). For this analysis, we choose an adaptive bi-variate KDE method based on the smoothing properties of a linear diffusion process. *Botev et al.* (2010) explain the details of the method and provide a link to the numeric algorithm implemented in MATLAB. The KDE function was fitted to the observed locations of eddy generation and decay to construct maps of probability of occurrence. The degree of smoothing was chosen so that probability contours roughly follow boundaries

of the binned cells. This corresponds to a decorrelation scale of 300 km in the zonal and meridional direction. Fig. 4.1 shows the isolines (black contours) of equal probability of the multi-peak Gaussian KDE chosen as the boundaries of these regions. The boundaries encompass the regions with bins with 40 or more identified events of eddy generation or decay. For the remainder of this chapter, we will refer to the areas encompassed by the KDE boundaries depicted in Fig. 4.1 as hotspots of eddy generation and decay.

4.3 The influence of topography on eddy generation hotspots and eddy tracks

The Southern Ocean contains several prominent topographic features (e.g., *Smith and Sandwell*, 1997). The interaction of these bathymetric obstacles with the strong ACC flow generates localized dynamics that are naturally not captured by a zonally or streamwise-averaged framework. A qualitative relation between prominent bathymetric features and the areas of high probability of eddy generation is shown in Fig. 4.2. The KDE contours, as defined in section 4.2, are overlaid on Southern Ocean topography from *Smith and Sandwell* (1997). The topography used in this study corresponds to the global topography version 17.1 available for public use (ftp://topex.ucsd.edu/pub/global_topo_1min/). Each of the five major hotspots south of 40°S are associated with a major topographic feature, and in each case the hotspot is located downstream, and in some cases on top, of the topographic feature. The site labeled as DP is located east of Drake Passage, a choke point for the ACC. Site WIR lies on the eastern border of the Western Indian Ridge. Site KP is bounded by the Kerguelen Plateau on the South, and the Western and Eastern Indian ridge on the western and eastern flanks. Site CP is west of the Macquarie Ridge and bounded by the Campbell Plateau to the north. Site EFZ is aligned with the axis of the Eltanin Fracture Zone. The climatological positions of the Polar Front (PF) and Subantartic Front (SAF) from *Orsi et al.* (1995) are shown in red. Both the PF and SAF cross all hotspots. The close proximity of the eddy hotspots to major topographic features and ACC jets sug-

gests that the interaction of the ACC with topography has a significant role in the enhanced eddy activity observed in these regions. Previous studies based on altimetric data, showed that the distribution of eddy kinetic energy (EKE) in the Southern Ocean is highly heterogeneous and enhanced on the lee side of major topographic features (e.g., *Le Traon and Morrow*, 2001). Our results suggest that a fraction of this elevated EKE activity is associated with semi-coherent vortices.

The analysis of the displacement of eddy centroids reveals that topography not only controls the preferred location of eddy generation, but it also constrains the overall region where eddies propagate away from the generation region. Fig. 4.3 shows the KDE contours associated with the regions of high probability of eddy generation (black) and the eddy tracks (red); very few eddies escape the boundaries of the KDE, even though their life-cycle can be several months or in some cases years, as shown in section 4.4. There is also a close relation between the boundaries of the hotspots and the f/H field, where f is the Coriolis frequency and H the total depth of the fluid. Fig. 4.3 overlays the f/H field with the KDE contours. For each region shown in Fig. 4.3, the KDE boundaries are mostly tangent to f/H contours, and they tend to be located in regions with strong gradients of f/H. This is particularly clear in the DP, KP and CP hotspots (Fig. 4.3a, c and d respectively). The only exception perhaps is the area associated with the EFZ site (Fig. 4.3e) where the southern boundary of the KDE lies on an f/H plateau.

Topographic steering of floats and surface drifters has been observed in the past (e.g., *Richardson*, 1981; *Rossby et al.*, 1983; *Lacasce*, 2000). Even though eddy tracks are strongly constrained by the hotspot boundaries, which follow f/H contours, it is not clear from Fig. 4.3 whether eddy tracks follow f/H contours as well. Under weak or no forcing, eddies would either follow f, i.e. propagate westward like non-linear Rossby waves, or f/H if eddies are deep enough to interact with bottom topography. However, if the system is strongly forced, by wind-stress curl for example, then neither f nor f/H is necessarily conserved and eddy displacement is harder to predict. A way to quantify the degree of steering by topography is to compute the dispersion of eddy tracks in geographical coordinates and in a rotated coordinate system locally aligned with f/H contours. The degree of

anisotropy of the dispersion of eddy tracks in each coordinate system gives an indication of the preferential direction of eddy tracks: i.e. an increased anisotropy of the dispersion in the rotated coordinate system, with respect to the geographical coordinate system, would suggest a preference for eddy tracks to follow f/H contours rather than to move zonally.

Dispersion estimates can be sensitive to topographic smoothing. Little or no smoothing of the H field results in a noisy f/H field, and the gradients obtained from differentiating the field are even noisier. An overly smooth f/H field results in along and across f/H dispersion values that tend to converge to the zonal and meridional dispersion values, a consequence of the overall zonal alignment of the f/H field. *Lacasce* (2000) provided a more in depth discussion of the effect of smoothing on the dispersion results, and *LaCasce and Speer* (1999) discussed error propagation. After experimenting with different degrees of smoothing, we chose a low-pass filter with a cut-off wavelength of 200 km to smooth the topography before computing f/H.

To estimate the eddy dispersion, we followed the methodology applied by *Lacasce* (2000) to compute float dispersion in the North Atlantic. The components of velocity directed along and across f/H contours were determined by projecting the meridional and zonal velocities into a coordinate system defined by contours of f/H. The net displacements along and across f/H contours were then computed by integrating in time the along and across f/H velocities. The dispersion (D_γ) and mean position (M_γ) of eddy tracks are defined by:

$$D_\gamma(t) = \frac{\sum_i \left(\gamma_i(t) - \gamma_i(0) - M_\gamma(t)\right)^2}{N(t) - 1} \left[1 \pm z\left(\frac{2}{N(t) - 1}\right)^{\frac{1}{2}}\right] \tag{4.1}$$

$$M_\gamma(t) = \frac{\sum_i \gamma_i(t) - \gamma_i(0)}{N(t)}, \tag{4.2}$$

where $\gamma(t)$ is the displacement of eddy tracks in km, $N(t)$ the number of available eddy tracks at time t, and z was set to 1.96 to compute the 95% confidence level (the eddy tracks are assumed to have a normal distribution). For practical purposes, the dispersion was computed assuming that the regions were stationary and that

all eddies were generated at the same time. It is common to invoke stationarity in Lagrangian ocean studies to achieve statistical significance (e.g., *Davis*, 1991). No spatial pattern or temporal pattern were detected in the eddy generation locations inside the hotspots, consistent with the assumption of stationarity.

Fig. 4.4 shows a comparison of the anisotropy of the dispersion for each hotspot (columns) and eddy sense of rotation (rows) in geographical and rotated coordinates (black solid and dashed lines respectively). The anisotropy is computed as the absolute difference of the zonal and meridional dispersion in geographical coordinates, and in the rotated coordinate system, it is the along-f/H minus cross-f/H dispersion. The dispersion along f/H (blue) and across f/H (red) contours is also shown. (For clarity the zonal and meridional dispersion were omitted.) For most of the regions, the zonal dispersion is greater than the meridional dispersion (not shown), consistent with the ACC being predominantly a zonal flow. The along-f/H dispersion is greater than the cross-f/H dispersion for most of the regions as well. When the along-f/H component is not dominant, as in the DP hotspot for CEs, then the along- and cross-f/H dispersion are statistically indistinguishable. Greater dispersion along f/H than across f/H contours does not necessarily indicate a tendency of eddies to follow f/H contours, since the f/H field is more or less aligned in the zonal direction. However if the anisotropy of the dispersion increases when the coordinate system is rotated to be locally align with the f/H field, then this would indicate that eddy tracks preferentially follow f/H contours rather than moving zonally. Evidence of topographic steering is supported by Fig. 4.4; however, results are not consistent throughout the hotspots. An increase in the anisotropy of the dispersion is evident for the DP, KP and CP hotspots in the rotated coordinate system, but no significant increase is observed for the WIR and EFZ hotspots. This is consistent with the overall topology of the f/H field. Hotspots that show an increased anisotropy when dispersion is computed along and across f/H contours are the ones located in the vicinity of strong f/H gradients (DP, KP and CP). In contrast the WIR and EFZ hotspots are located in regions of relatively weak f/H gradients and flanked by f/H plateaus.

The anisotropy of the dispersion also changes in time, with a tendency for

higher anisotropy for timescales longer than 6 to 12 weeks, depending on the site. This result suggests that eddies tend to follow f/H contours except perhaps during the first 2 to 3 months of their lifecycle. Eddies are generated with a more or less homogeneous spatial distribution at each site (as will be shown in the next section). The interior of each site has relatively weak f/H gradients (Fig. 4.3); we hypothesize that eddies generated over those plateaus will not show a strong preference to follow f/H until later in their lifecycle, when they are near the boundaries. To test this hypothesis, we computed the dispersion separately for eddies generated close to the boundaries and for eddies generated in the interior. A threshold of 100 km to 200 km, depending on the size of each site, was used to separate boundary and interior regions. For all sites, the dispersion calculated for interior eddies shows a decrease in anisotropy, or no anisotropy at all, supporting the hypothesis that eddies closer to the hotspot boundaries are the ones that preferentially follow f/H contours. The most significant change occurs for the EFZ. When all eddy tracks are used to compute the dispersion, eddies in the EFZ show no preference for following f/H contours. If interior eddies are removed (approximately 60% of the tracks), the anisotropy in the dispersion increases significantly (yellow lines in Fig. 4.4, EFZ site).

The results presented in this section suggest that in some regions, there is a preferential tendency for eddies to conserve f/H rather than f over the course of their lifetimes. This is consistent with barotropic circulation. However this is not, strictly speaking, proof of conservation of barotropic potential vorticity, approximated by f/H (e.g., *Vallis*, 2006). Nevertheless potential vorticity conservation is a plausible assumption in the regions of the Southern Ocean where to leading order the ACC acts as an equivalent barotropic current (e.g., *Killworth and Hughes*, 2002; *Firing et al.*, 2011). Caution should be taken though, as evidence of non-equivalent barotropic structure has been reported at localized areas of the ACC (*Phillips and Bindoff*, 2014).

4.4 Statistical properties of eddies

The focus of this section is the analysis of eddy trajectories, lifetimes and decay rates. These properties are dependent on the eddy polarity (i.e., the sense of rotation) (e.g., *Chelton et al.*, 2011). Previous studies have found several regions of the world ocean where eddies of one polarity are known to be generated preferentially (e.g., *Feron et al.*, 1992; *Pingree and Sinha*, 2001; *Saraceno and Provost*, 2012). In principle ACC jets could act as boundaries where a preferential polarity could be observed at either side of the jets. As meanders pinch off to form closed vortices, anticyclonic vorticity would be favored on the poleward side and cyclonic vorticity on the equatorward side. This formation mechanism has been previously observed in eastward currents (*Chelton et al.*, 2011). In the Southern Ocean, *Frenger et al.* (2015) found regions of preferential polarity, most notably a preference for cyclonic eddies (CEs) north of the ACC in the Indian and Pacific sectors and a preference for anticyclonic eddies (AEs) in the southern limb of the Pacific subtropical gyre. They attributed this polarity bias to larger formation numbers and lifetimes of one particular eddy type in those areas. Polarity also has an effect on the meridional displacement of the eddies (e.g., *Cushman-Roisin et al.*, 1990). As we will show, our results do not show evidence of a bias in eddy polarity inside the hotspots regions.

4.4.1 Trajectories and mean relative displacements

A summary of the eddy trajectories and relative displacements for the WIR site is shown in Fig. 4.5. The spatial distribution of the initial locations inside the WIR region shows no evident relation between the initial locations and eddy polarity: Fig. 4.5a for AEs and Fig. 4.5c for CEs. ACC jets meander in time in the meridional direction. This displacement might be responsible for the lack of a clear pattern of eddy polarity poleward and equatorward of the ACC. *Sokolov and Rintoul* (2009b) computed the probability distribution of the front locations and found the width of the meander envelope to be of about ± 1 degree of latitude. The eddy polarity spatial signal could be smeared out by the meridional ACC

migration. A more careful analysis following the jet migration is needed to answer this question thoroughly. This result is consistent with *Frenger et al.* (2015), who found no preferential eddy polarity for a narrow circumpolar region encompassing the SAF and PF. Their analysis however, was focused on preferential regions of polarity and not on polarity and eddy generation locations, so results cannot be compared directly. The eddy trajectories are mostly constrained within the region boundary for both AEs and CEs, and very few trajectories cross the boundary. As was discussed in section 4.2, the boundaries of the hotspots closely follow contours of f/H, and eddy trajectories seem to be topographically steered.

The relative displacements for AEs and CEs are illustrated in Fig. 4.5b and Fig. 4.5d respectively. Also shown is the mean relative displacement, defined as the average of all the individual eddy trajectories with initial locations inside the boundary defined by the KDE contour. The mean relative displacement is composed of at least 100 trajectories. When fewer than 100 trajectories are available, the mean trajectory paths are shown as dash-dot lines. Both AEs and CEs have a mean eastward displacement in the WIR region. Eddies have a self-induced westward motion, which can be attributed to the potential vorticity (PV) gradient (e.g., *Nof*, 1983). The eddy westward motion has been well documented by several observational studies (e.g., *Chelton et al.*, 2011). In the ACC however, the self-induced westward motion is countered by the advection of the ACC, and eddies have a net eastward displacement as shown by Fig. 4.5. Eddies also undergo a meridional drift, which is not as noticeable as the zonal drift. The mean relative displacement shows that AEs tend to drift poleward and CEs equatorward (black lines in Fig. 4.5b and Fig. 4.5d respectively). This meridional displacement opposes the drift reported in previous work for eddies outside the ACC (e.g., *Morrow et al.*, 2004b; *Chelton et al.*, 2011). A detailed explanation of the meridional drift for eastward propagating ACC eddies was discussed in Chapter 2.

Except for the DP region, the rest of the domains present results similar to those from the WIR site. The zonal displacement is eastward, and the meridional displacement is reversed relative to the prevailing midlatitude eddy meridional displacement. No evident relation between polarity and initial locations can be

identified. Trajectories are mostly constrained to the area defined by the KDE contours and rarely leave the area. This confirms the result presented in section 4.2: the hotspots of eddy generation and decay are defined by the same eddies (Fig. 4.1). Results are summarized by Fig. 4.6 (CP region), Fig. 4.7 (EFZ region) and Fig. 4.8 (KP region).

The DP region, illustrated in Fig. 4.9, has no preferential initial location for either CEs or AEs, with the initial locations covering most of the area defined by the KDE contour. Perhaps the exception is the region close to the southern boundary of the domain, where there appears to be a slight preference for CEs. As expected, both AEs and CEs have a mean eastward displacement due to advection by the ACC. The meridional displacement is equatorward for both AEs and CEs; this is also an effect of advection by the mean flow, since the ACC has a strong northeastward component throughout Drake Passage. However, the reverse meridional displacement is still evident, as CEs have a stronger equatorward component than AEs.

4.4.2 Eddy lifetime, polarity and mean translational speed

As with eddy trajectories and eddy relative displacements, the eddy lifetime and polarity distributions are similar in all the hotspots. To avoid repetition, only results for the average of all the regions are shown (Fig. 4.10), but the conclusions are valid for each separate region as well. The histogram of the number of eddies versus lifetime (Fig. 4.10a) shows that the eddy life expectancy distribution decays rapidly, with an e-folding scale of 9 weeks for both cyclonic and anticyclonic eddies. As was discussed in section 4.2, the detection methodology could misidentify meanders as coherent eddies, especially in regions with strong meandering jets like the ACC. Since meanders can evolve more rapidly in time than eddies (*Chelton et al.*, 2011), this could contaminate the number of observed eddies at the 4 to 15 week range. Hence the difference between the number of eddies with long lifetimes versus short lifetimes shown in Fig. 4.10a might be an overestimate.

Previous studies showed that when the global eddy population is considered, CEs dominate over AEs for lifetimes less than 60 weeks, and AEs are more preva-

lent for lifetimes over 80 weeks, while the intermediate time span (60 to 80 weeks) showed no predominance of CEs or AEs (*Chelton et al.*, 2011). In contrast, our results show that for all for all eddy lifetimes there are more CEs than AEs. This is more clear in the upper-tail cumulative histogram of eddy lifetimes (Fig. 4.10b) where the dash-dot line shows the difference between CEs and AEs. Although the histograms in Fig. 4.10a,b show the evolution of eddies up to 30 weeks, the dominance of CEs holds for the duration of all eddy lifetimes (150 weeks). The predominance of AE for relatively large amplitude eddies is expected from the gradient wind effect: the centrifugal force intensifies the low pressure at the center of CEs and weakens the high pressure at the center of the AEs. The dominance of CEs over AEs for all lifetimes is specific to the population of eddies generated inside the hotspots. When the eddy population of the whole Southern Ocean is considered (with no amplitude threshold), then our results are consistent with the analysis of the global eddy population of previous studies, with the caveat that the transition from cyclonic to anticylonic dominance happens around 50 weeks instead of 80 weeks.

Fig. 4.10c shows a scatter plot of the distance traveled as a function of lifetime. The distance traveled is defined as the cumulative sum of the great-circle distance between successive eddy centroid locations over the eddy lifetime. No differences between CEs and AEs can be identified. The distance is a linear function of eddy lifetime and no significant differences between cyclonic and anticylonic eddy speeds were found. The average speed for all sites is 4.9 ± 0.1 cm s^{-1} for CEs and 5.1 ± 0.1 cm s^{-1} for AEs. Mean translation speeds for each site and for CEs and AEs are shown in Table 4.1. The linear fit for each region yields similar values ranging from 4 to 6 cm s^{-1}. Fig. 4.10d shows a scatter plot of the range, defined as the great-circle distance between the final and initial eddy centroid locations, versus the eddy lifetime. No clear relation between range and eddy lifetime can be identified, a result consistent with the tendency of eddy trajectories to stay within the boundaries of the hotspots.

4.5 Eddy energy sources

The transport of energy associated with eddies is significant and plays a role in the global redistribution of energy in the ocean (e.g., *Xu et al.*, 2014). Baroclinic instability is a well known source of eddy generation and it has been documented in several studies (e.g., *Wright*, 1981; *Vallis*, 2006; *Tulloch et al.*, 2011). Barotropic instability is perhaps less common as an energy source for eddies (e.g., *Qiu and Chen*, 2004). To diagnose the main energy source in each of the hotspots, we use data from an eddy-permitting assimilating model, the Southern Ocean State Estimate (SOSE) (*Mazloff et al.*, 2010). The version of SOSE used in this analysis has a horizontal resolution of 1/6° and 42 vertical levels of varying thickness. Model output is available for the 2005-2010 time period. SOSE, which is public (http://sose.ucsd.edu), has been used to examine a wide range of ocean processes: for example, *Cerovečki and Mazloff* (2016) analyzed the formation and evolution of Subantartic Mode Water in the Southern Ocean, and *Firing et al.* (2011) analyzed the ACC velocity structure in Drake Passage. Here we use SOSE velocity and density fields, to estimate the shear and buoyancy production terms for the Southern Ocean.

4.5.1 Barotropic versus baroclinic instabilities

Under the Boussinesq approximation, an expression for the turbulent kinetic energy (TKE) of the flow per unit mass, $\bar{E} = \frac{1}{2}u_i^2$, can be obtained by multiplying the momentum equation of the turbulent flow,

$$\frac{\partial u_i}{\partial t} + U_j\frac{\partial u_i}{\partial x_j} + u_j\frac{\partial U_i}{\partial x_j} + u_j\frac{\partial u_i}{\partial x_j} - \frac{\partial\left(\overline{u_i u_j}\right)}{\partial x_j} = -\frac{1}{\rho_0}\frac{\partial p}{\partial x_i} - \frac{g\rho'}{\overline{\rho}}\delta_{i3} + \nu\frac{\partial^2 u_i}{\partial {x_j}^2}, \quad (4.3)$$

by the anomaly velocity field (u_i), and taking the time average (e.g., *Kundu et al.*, 2012):

$$\frac{D}{Dt}\overline{\left(\frac{1}{2}u_i^2\right)} = -\frac{\partial}{\partial x_j}\left(\frac{1}{\rho_0}\overline{pu_j} + \frac{1}{2}\overline{{u_i}^2 u_j} - 2\nu\overline{u_i e_{ij}}\right) \underbrace{-\overline{u_i u_j}\frac{\partial U_i}{\partial x_j}}_{\text{shear production}}$$
$$-2\nu\overline{e_{ij}e_{ij}} \underbrace{-\frac{g\overline{u_3\rho'}}{\bar{\rho}}}_{\text{buoyancy production}}, \qquad (4.4)$$

where e_{ij}, the fluctuating strain rate is defined by:

$$e_{ij} \equiv \frac{1}{2}\left(\frac{\partial u_i}{\partial x_j} + \frac{\partial u_j}{\partial x_i}\right). \qquad (4.5)$$

Equations 4.3 to 4.5 are in tensor notation and the time average operator is denoted by $\overline{(\ )}$. The remaining variables appearing in expressions 4.3 to 4.5 are the mean flow (U_i), kinematic viscosity (ν), reference density (ρ_0), density fluctuations (ρ'), pressure fluctuations (p) and gravity (g).

The first three terms on the right-hand side of (4.4) are associated with transport of TKE by pressure, viscous stresses, and Reynolds stresses respectively. The fifth term is associated with the direct viscous dissipation of TKE via its conversion into heat. These terms either re-distribute TKE over the domain or directly dissipate energy and are not associated with eddy energy sources. The relevant terms of (4.4) for this study are the terms that exchange energy with the mean potential energy (PE) and the mean kinetic energy (MKE) fields. The fourth term on the right-hand side of (4.4), which also appears in the MKE budget with opposite sign, represents the rate at which kinetic energy is lost by the turbulent flow and gained by the mean flow. This term is commonly called the shear-production term. The last term on the right-hand side of (4.4) is the buoyancy production of turbulent kinetic energy. It transfers energy between the PE field and the TKE field. The energy source of eddies could be associated with one or both of these terms. To evaluate the relative roles of baroclinic and barotropic instabilities in generating eddies, we compare the magnitudes of the shear and buoyancy production terms.

Fig. 4.11a shows the vertically integrated shear production for the Southern Ocean. Shear production ranges from -7 to +7 $\times$ 10^{-5} m^3 s^{-3}. Relatively

higher absolute values of shear production tend to coincide with the eddy generation hotspots identified with satellite altimetry (denoted by the black contours in Fig. 4.11). However the pattern in Fig. 4.11 is patchy with blobs of positive and negative values within the hotspots boundaries. This indicates transfer of energy from the turbulent field to the mean field (positive values denoted by red) and vice versa (negative values denoted by blue).

The vertical buoyancy production term is shown in Fig. 4.11b. As with the shear production terms, higher values are confined within the hotspot boundaries. Vertically-integrated buoyancy production ranges from -1 to $+1 \times 10^{-3}$ m^3 s^{-3}, one order of magnitude larger than the shear production term. Values are predominantly positive, consistent with the transfer of energy being mainly from the PE field to the TKE field. This result is consistent with the eddies generated inside the hotspots resulting from baroclinic instabilities.

More representative values of the shear and buoyancy production terms were estimated for each hotspot site by spatially averaging an ensemble of 24 realizations, each of 3-months duration. These estimates span the full 2005-2010 time period available from SOSE. Table 4.2 shows the spatial mean and standard error of the vertically integrated buoyancy and shear production for each hotspot. As suggested visually by Fig. 4.11a, the shear production term oscillates around zero in most cases, and has mean values of both signs. The buoyancy production is positive in sites, indicating transfer of energy from the PE field to the TKE field. The WIR site has a mean value of 4.4×10^{-6} m^3 s^{-3}, with a standard error of $\pm$ 4.1×10^{-6} m^3 s^{-3}, at least one magnitude smaller than the rest of the sites and close to zero. A possible explanation is that SOSE does not reproduce well the eddy field seen by altimetry in this particular region, specifically in the southern region of the WIR site where virtually no eddies are in SOSE's SSH$'$ field. This is not surprising since SOSE's 1/6° resolution is coarser than the Rossby deformation radius at high latitudes. A second estimation of the WIR site was computed using only the northern section of the WIR site. By removing the southern portion of the site, the average value is one order of magnitude bigger (indicated as WIR* in Table 4.2), and the standard error is no longer near zero.

4.5.2 Potential energy as seen from Argo floats

The estimation of the shear and buoyancy production terms shows that within SOSE the main source of energy of the eddies generated within the hotspots comes from the PE field. To corroborate this result, we analyzed the PE from an independent data set to support the argument for baroclinic instabilities as the main generation mechanism for Southern Ocean eddies. Argo profiles for the region south of 30°S were retrieved from the U.S. Global Ocean Data Assimilation Experiment Global Data Assembly Center (USGODAE GDAC) for the period from January 2001 to December 2014. Only delayed-mode profiles were retained since real-time profiles, i.e. data available within 24 hours of the float reaching the surface, are not corrected for sensor drifts or offsets (*Wong et al.*, 2015). In addition data were omitted if the pressure, salinity, temperature, float location or date measurements did not pass the quality control routine for delayed-mode data (quality flag not set to 1). See *Wong et al.* (2015) for details about the quality control process. After the quality control, the total number of Argo profiles was roughly 220,000. Observations were interpolated to regular interval pressure levels from the surface to 2000 db. Interpolated fields were objectively mapped following *Davis* (1985) with spatially varying decorrelation scales ranging from 100 to 200 km (*Zajaczkovski*, 2017). The potential density σ_θ was estimated from the interpolated fields of Conservative Temperature (Θ) and Absolute Salinity (S_A), and γ surfaces were fit to the Argo profiles using the routines developed by *Jackett and McDougall* (1997).

Fig. 4.12 shows a zonally averaged meridional section of γ surfaces estimated from Argo floats. Only longitudes that cross the hotspots are included in the average process. The meridional section illustrates the well-known vertical structure of the potential density field in the Southern Ocean (e.g. *Marshall and Speer*, 2012). Except for the isopycnals near the surface (pressure levels < 300 db), most isopycnals are flat north of 35°S. However south of that latitude isopycnals rise toward the surface, outcropping at different latitudes, with the deeper isopycnals outcropping further south than the shallower ones. The meridional boundaries of the hotposts span a wide range of latitudes: as far north as 40°S for KP, and

as far south as 65°S for EFZ. This latitude range is consistent with the latitude range where the slope of isopycnals is steeper in the meridional section shown in Fig. 4.12. The overlapping latitude range suggests a relationship between hotspot locations and availability of PE.

To further explore the relationship between the potential density field and the hotspot locations, in Fig. 4.13 we show meridional sections of the 27.3 kg m^{-3} γ surface (denoted as a solid red line in Fig. 4.12) for different longitudes crossing the hotspots. For each hotspot (color-coded), a western and eastern section are shown. For clarity, sections are shifted in the vertical axis to avoid overlapping. As a reference, the pressure levels of the northern and southern tips of each meridional section are labeled in Fig. 4.13. As suggested by the zonally-averaged meridional section (Fig. 4.12), for each section shown in Fig. 4.13 no flat isopycnals are found within the boundaries of the hotspots. Further inspection suggests that steep isopycnal slopes can be found inside and outside the hotspots; The clearest example of this argument is the eastern section of KP (60°E): at the northern end of the section the isopycnal is flat, it starts to shoal at about 38°S, which roughly coincides with the hotspot boundary, located at 40°S at this longitude. A steep slope can be seen throughout the latitude range where the hotspot is located (40°S to 47°S). South of the southern boundary of the hotspot the isopycnal flattens again. The analysis of the Argo-derived density field, and its relation to the altimeter-derived hotspot boundaries, provides further independent evidence that baroclinic instability is the main mechanism of eddy generation inside the hotspots. A circumpolar path crossing all hotspots, showing γ, the buoyancy production, and the rest of the variables discussed in this chapter is analyzed in the next section.

4.6 An integrated view along a circumpolar path

A simple model of the ACC assumes the system to be adiabatic in the interior. In this framework, a relationship between the isopycnal slope (s), the surface wind stress (τ_w) and κ, a parametrization of the eddy fluxes in terms of the

mean flow, can be derived from the zonal momentum equation (e.g., *Vallis*, 2006):

$$\tau_w = \kappa \; f \; s. \tag{4.6}$$

This idealized adiabatic model implies that the net residual overturning is zero, an assumption that does not hold in the ACC (e.g., *Vallis*, 2006). However, (4.6) can be interpreted as a first-order balance between wind-driven and eddy overturning cells, instead of an exact equality. The dynamics of this approximate balance were studied by *Meredith and Hogg* (2006), who found that an intensification of τ_w was followed by an enhancement of EKE activity with a 2- to 3-year lag. This lag was interpreted as the timescale associated with buoyancy production. The excess of energy imparted by the wind is initially stored as potential energy (PE). This excess of PE in turn increases eddy activity which slowly transfers momentum downwards through interfacial form stress. Eventually the energy is released via baroclinic instability until the excess of PE is consumed.

The analysis performed by *Meredith and Hogg* (2006) focused on three different areas, roughly encompassing the Atlantic, Indian and Pacific Ocean sectors of the Southern Ocean. *Thompson and Garabato* (2014) showed that the equilibration process outlined by *Meredith and Hogg* (2006) was localized, and they attributed the downward transfer of momentum to standing meanders, a mechanism previously identified in simplified models of the ACC (*Treguier and McWilliams*, 1990). These standing meanders, localized downstream of topographic features, are all contained within the hotspot regions identified here. With the exception of the EFZ where no standing meanders were found. Standing meanders, as elucidated by *Thompson and Garabato* (2014), react to an increase in wind stress forcing by changing their curvature which leads to enhanced baroclinicity. This enhanced baroclinicity could in turn lead to baroclinic instabilities and generation of eddies. Hence the overlapping areas of meanders identified by *Thompson and Garabato* (2014) and eddy hotspots identified in this work are not coincidental.

Fig. 4.14 shows a circumpolar average of the properties analyzed in the previous sections. The circumpolar path, shown in Fig. 4.2, roughly follows the SAF. The results are independent of the specific path chosen, provided that the path

crosses all the hotspots of eddy activity and associated topographic features. The red and blue colors in the background of Fig. 4.14 indicate when the circumpolar path is inside or outside a hotspot respectively. Fig. 4.14a shows a circumpolar average of the buoyancy production. As was shown in section 4.5, buoyancy production peaks inside the hotspots (red shaded sections), and very little buoyancy production is observed outside the hotspots (blue shaded sections). Another way to visualize the buoyancy production activity is by looking at the cumulative circumpolar integral of buoyancy production along the path (Fig. 4.14b). The slope, proportional to the buoyancy production, steepens inside hotspots, which indicate high buoyancy production, and flattens outside the hotspots.

The comparison of Fig. 4.14b and 4.14c suggests that the areas of enhanced eddy activity and the steepness of the isopycnal slope are closely connected. The slopes of the 27.2 kg m^{-3} and 27.8 kg m^{-3} γ surfaces are shown in Fig. 4.14c. Inside all hotspots (red shaded sections) the slope of γ is significant, indicating availability of PE. In contrast, outside the hotspots (blue shaded sections) the slope is found to be flat (between CP and EFZ, and between EFZ and DP) or step (between KP and CP). This implies that there are regions, outside the hotspots, with available PE but no enhanced eddy activity. These regions however are not located near major topographic features. Fig. 4.14d shows the bathymetry along the path: all hotspots are associated with a major topographic feature (red shaded sections), while outside those regions the bathymetry tends to be relatively flat. As *Meredith and Hogg* (2006) suggested, the balance in (4.6) is maintained by generating eddies to compensate the excess of energy imparted by the wind, hence compensating for changes in s. This is also supported by observational evidence that suggests that there were no significant changes in the isopycnal slope of the ACC over the last 50 years (*Böning et al.*, 2008). Our results are consistent with these findings.

Fig. 4.14e shows the wind stress curl ($\nabla \times \tau$) along the circumpolar path. $\nabla \times \tau$ inside the hotspots is slightly larger in magnitude than outside the hotspots, except for the KP and DP sites where it is significantly larger. It has been shown that winds can have a dampening effect in ocean motions (e.g., *Dewar*, 1987). The effect can be quantified by taking into account the relative motion between

the atmosphere and the surface of the ocean when estimating the wind stress (commonly called the relative wind stress effect). The dampening effect of the relative wind stress has been suggested to operate primarily on mesoscale eddies (e.g., *Duhaut and Straub*, 2006; *Hughes and Wilson*, 2008). *Xu et al.* (2016) showed that the dampening effect is particularly strong in the western boundary currents and the Southern Ocean. This could explain why eddies generated inside the hotspots tend to decay without leaving the area of generation (see section 4.2).

The relationship between EKE and wind stress time variability in the Southern Ocean has been examined by multiple studies. In particular, *Meredith and Hogg* (2006) found a 3-year lag between EKE activity and the Southern Annular Mode (SAM). Further evidence of this lag was provided by global eddy-permitting ocean models (*Screen et al.*, 2009). *Morrow et al.* (2010) showed that El Niño Southern Oscillation (ENSO) impacts EKE activity: enhanced EKE activity occurs when La Niña periods overlap with strong positive SAM events, while a more moderate EKE response is associated to El Niño periods overlapping strong SAM events. A more recent study showed that EKE and wind stress variability are correlated in the Pacific and Indian sectors of the Southern Ocean, with no evidence of correlation in the Atlantic Ocean (*Hogg et al.*, 2015). The excess of wind work imparted by the wind stress is initially stored as PE and subsequently transformed to EKE via baroclinic instabilities (e.g., *Thompson*, 2008). For the eddies detected in this study, no significant inter-annual variability was observed during the study period (1992-2012). This suggests that the enhanced EKE activity during strong SAM events reported by previous studies (*Meredith and Hogg*, 2006) is not associated with semi-coherent vortices. Meredith and Hogg's (2006) 3-year lag suggests that events from 2002-2007 should have influenced the SOSE time period considered in this chapter (2005-2010). However, there were no strong SAM or La Niña events during 2002-2007 (e.g., *Morrow et al.*, 2010), suggesting that the buoyancy production estimates presented here might be representative of the lower end of the wind forcing range. No significant time variability was found during 2005-2010, also consistent with no significant changes of the SAM during 2002-2007. The SAM has a relative maximum during 1999-2000 which overlaps with a strong La Niña

event (e.g., *Morrow et al.*, 2010); an analysis of the buoyancy production during those years might be more representative of the time variability associated with baroclinic instabilities. The details of the correlation between EKE activity and the strength of the SAM are still a subject of open debate (*Meredith and Hogg*, 2006; *Hogg et al.*, 2015). This subject requires further attention, but it is beyond the scope of this study. In summary, the high eddy activity observed as hotspots along the Southern Ocean can be explained by the combined effect of prominent topographic features, which enhanced baroclinic instability (e.g., *Chen and Kamenkovich*, 2013; *Abernathey and Cessi*, 2014), and the presence of available PE to generate eddies via baroclinic instabilities.

4.7 Conclusions

Eddies in the Southern Ocean were identified and tracked using altimeter data. We have shown that the generation of relatively large amplitude eddies ($>$ 4 cm) is not ubiquitous throughout the Southern Ocean but rather a phenomenon that is constrained to isolated, well-defined regions. The five hotspots of high probability of eddy generation are located downstream and on top of major topographic features with their boundaries closely following f/H contours. The eddies generated in these locations do not propagate far, and the vast majority decay within the boundaries of the generation area. A comparison of the degree of anisotropy of the dispersion of eddy tracks in geographical coordinates versus a rotated coordinates system aligned with f/H contours showed that in some hotspots (DP, KP and CP) eddies tend to follow f/H contours rather than f. Maps of buoyancy and shear production terms computed from a state estimate show enhanced values of both conversion terms inside the hotspots, with the former one order of magnitude larger than the latter. This result is consistent with eddy generation via baroclinic instability. The mean potential density field estimated from Argo floats shows that inside the hotspots isopycnal slopes are steep, indicating availability of potential energy and providing further evidence of the main generation mechanism. The hotspots identified in this chapter overlap with previously identified regions of

standing meanders. The hotspot locations can be explained by the combined effect of prominent topographic features, standing meanders, which enhance baroclinic instability, and availability of potental energy to generate eddies via baroclinic instabilities.

4.8 Acknowledgments

This work was supported by NASA Headquarters under the NASA Earth and Space Science Fellowship Program - Grant NNX11AL55H. Additional support was provided by NSF awards PLR-1425989 and OCE-1234473, and by NASA award NNX13AE85G. Computational resources for the SOSE were provided by NSF XSEDE resource grant OCE130007 and NSF grant PLR-1425989. SOSE was produced using the Extreme Science and Engineering Discovery Environment (XSEDE), which is supported by National Science Foundation grant number MCA06N007. The altimeter products were produced by SSALTO/Duacs and distributed by Aviso, with support from CNES. Argo data were collected and made freely available by the International Argo Program and the national programs that contribute to it. (http://www.argo.ucsd.edu, http://argo.jcommops.org). The Argo Program is part of the Global Ocean Observing System.

Chapter 4, in full, has been submitted for publication of the material as it may appear in Journal of Physical Oceanography, 2017. Zajaczkovski, U.; Gille, Sarah T.; Mazloff, Matthew R. The dissertation author was the primary investigator and author of this paper.

Table 4.1: Velocity of CE and AE estimated from a linear fit of traveled distance versus lifetime for each location.

Site	AE Velocity (cm s^{-1})	CE Velocity (cm s^{-1})
DP	5.9 ($\pm$ 0.2)	6.1 ($\pm$ 0.2)
WIR	4.2 ($\pm$ 0.2)	4.2 ($\pm$ 0.2)
KP	5.3 ($\pm$ 0.1)	5.0 ($\pm$ 0.1)
CP	5.1 ($\pm$ 0.1)	4.9 ($\pm$ 0.1)
EFZ	4.8 ($\pm$ 0.2)	4.5 ($\pm$ 0.1)

Table 4.2: Mean and standard error of vertically integrated buoyancy and shear production for each location. WIR* shows the averaged values estimated over the north section of the WIR region.

Site	Buoyancy Production (m^3s^{-3})	Shear Production (m^3s^{-3})
DP	9.0×10^{-5} ($\pm$ 3.4×10^{-6})	7.7×10^{-7} ($\pm$ 1.9×10^{-7})
WIR	4.4×10^{-6} ($\pm$ 4.1×10^{-6})	1.5×10^{-6} ($\pm$ 2.1×10^{-7})
WIR*	3.6×10^{-5} ($\pm$ 7.0×10^{-6})	2.6×10^{-6} ($\pm$ 4.0×10^{-7})
KP	6.9×10^{-5} ($\pm$ 3.6×10^{-6})	2.2×10^{-6} ($\pm$ 1.7×10^{-7})
CP	3.1×10^{-4} ($\pm$ 1.4×10^{-5})	-2.4×10^{-6} ($\pm$ 4.5×10^{-7})
EFZ	6.6×10^{-5} ($\pm$ 3.8×10^{-6})	5.6×10^{-7} ($\pm$ 1.2×10^{-7})

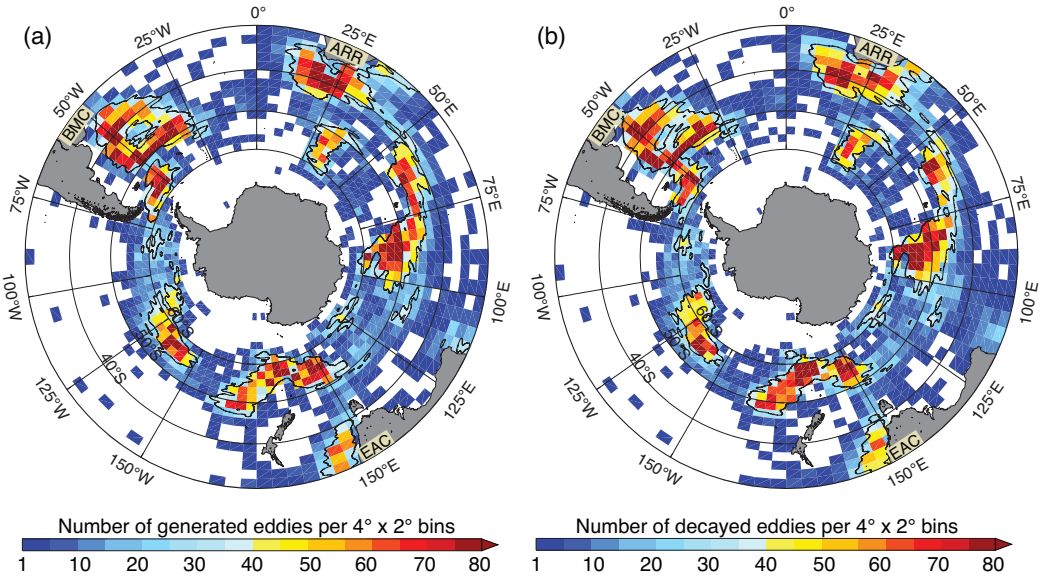

Figure 4.1: Locations of eddy generation (a) and decay (b) in 4°× 2° bins for eddies that surpass 4 cm in amplitude at any given stage of their life-cycle. Black contours denote isolines of equal probability of a multi-peak Gaussian kernel density function fitted to the binned data.

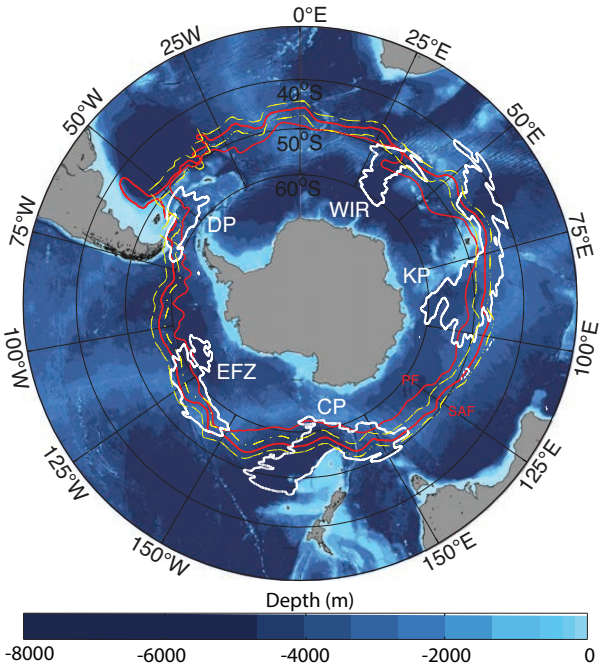

Figure 4.2: Topography and sites of high probability of eddy generation (white contours) south of 40°S. Each site is identified by the major topographic feature associated with it: Drake Passage (DP), Western Indian Ridge (WIR), Kerguelen Plateau (KP), Campbell Plateau (CP) and Eltanin Fracture Zone (EFZ). The climatological positions of the Subantarctic Front (SAF) and Polar Front (PF) as defined by *Orsi et al.* (1995) are denoted by red lines. Boundaries of the circumpolar average discussed in Section 4.6 (Fig. 4.14) are denoted by the dash-dot yellow lines.

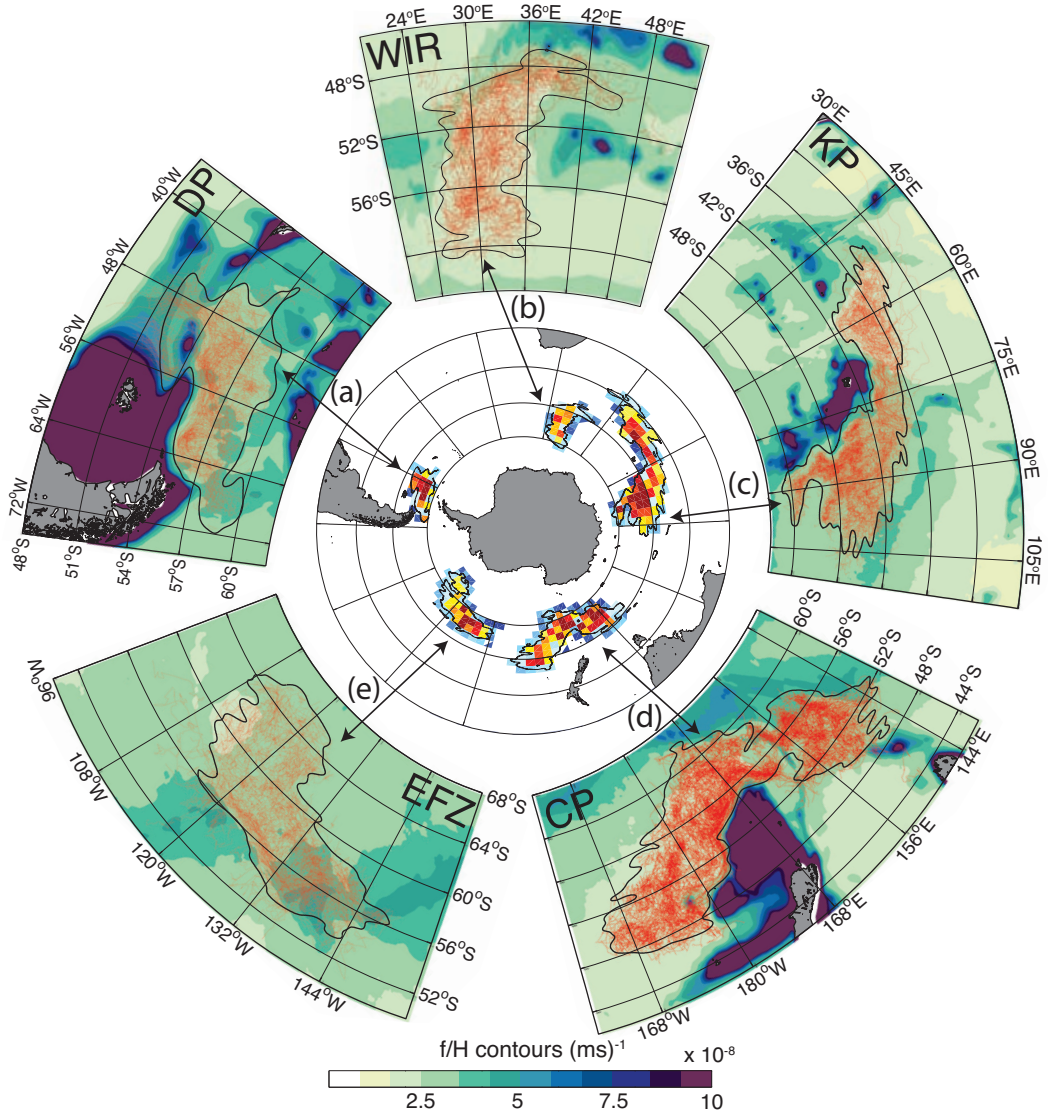

Figure 4.3: Smoothed f/H field for sites of high probability of eddy generation: (a) East of Drake Passage (DP), (b) Western Indian Ridge (WIR), (c) Kerguelen Plateau and Eastern Indian Ridge (KP), (d) Macquarie Ridge and Campbell Plateau (CP) and (e) Eltanin Fracture Zone (EFZ). Kernel density estimate contours are denoted in black and tracks of eddies generated inside each site are denoted in red.

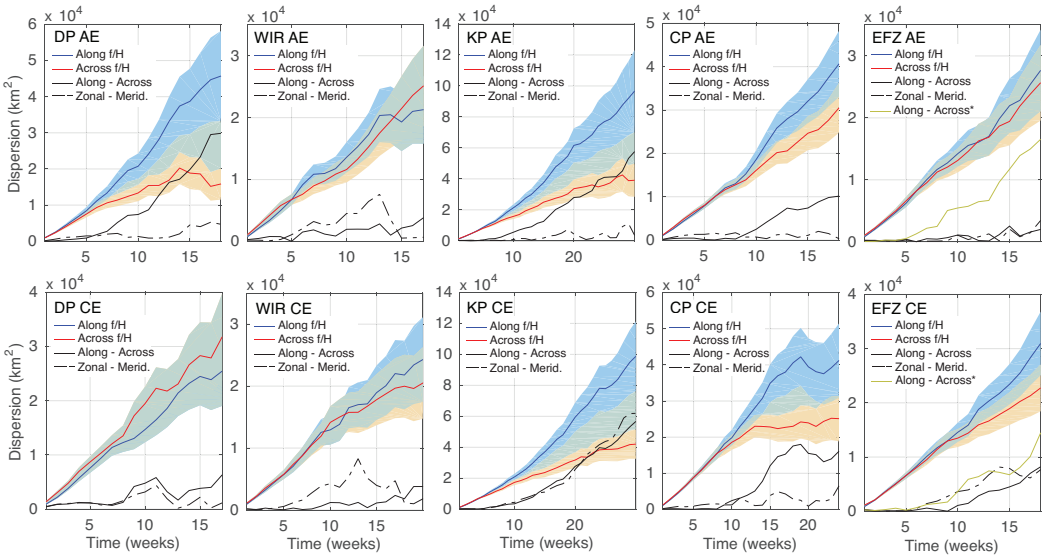

Figure 4.4: Dispersion of eddy tracks for AEs (top row) and CEs (bottom row) for each hotspot (from left to right: DP, WIR, KP, CP and EFZ). The dispersion along-f/H contours (blue) and cross-f/H contours (red) is shown for each hotspot, shaded areas represent the 95% confidence limits. The anisotropy of the dispersion in the coordinate system locally aligned with f/H contours (black solid line) and the anisotropy in the geographical coordinate system (black dashed line) is shown for comparison. Yellow lines in the EFZ hotspot indicate the anisotropy of the reduced set (boundary tracks only, see discussion in section 4.3). Results are composed of at least 100 eddy trajectories.

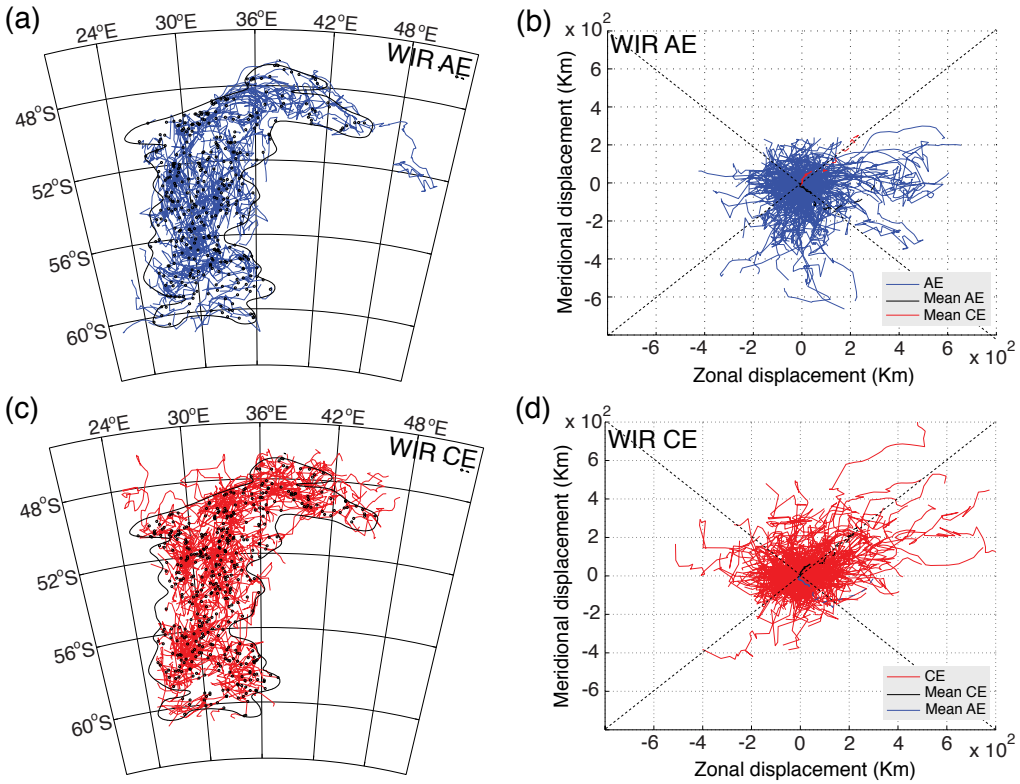

Figure 4.5: Eddy tracks for Western Indian Ridge site: (a) Tracks of anticyclonic eddies (AEs) (blue), locations of generation (black circles) and contour of kernel density estimate (KDE) (black). (b) Relative displacement of AEs (blue), mean relative displacement of AEs (black) and cyclonic eddies (CEs) (red). (c) Tracks of CEs (red), locations of generation (black circles) and contour of KDE (black). (d) Relative displacement of CEs (red), mean relative displacement of CEs (black) and AEs (blue). Mean displacements are denoted with solid lines if 100 or more eddies are available, and dash-dot lines if less than 100 eddy tracks are available to average.

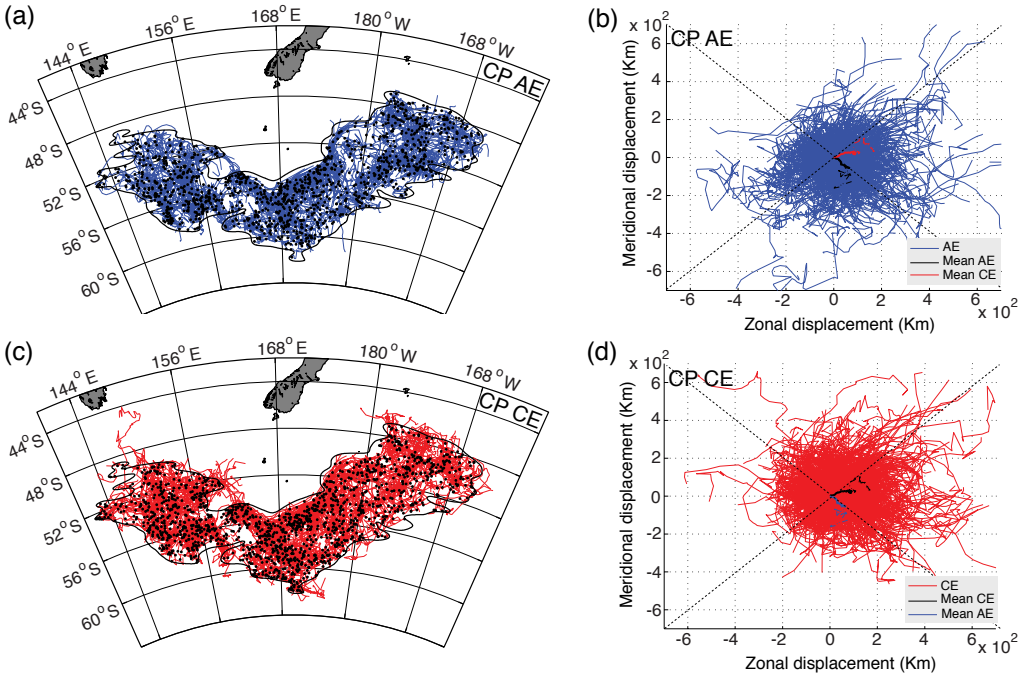

Figure 4.6: As in Fig. 4.5 but for Campbell Plateau site.

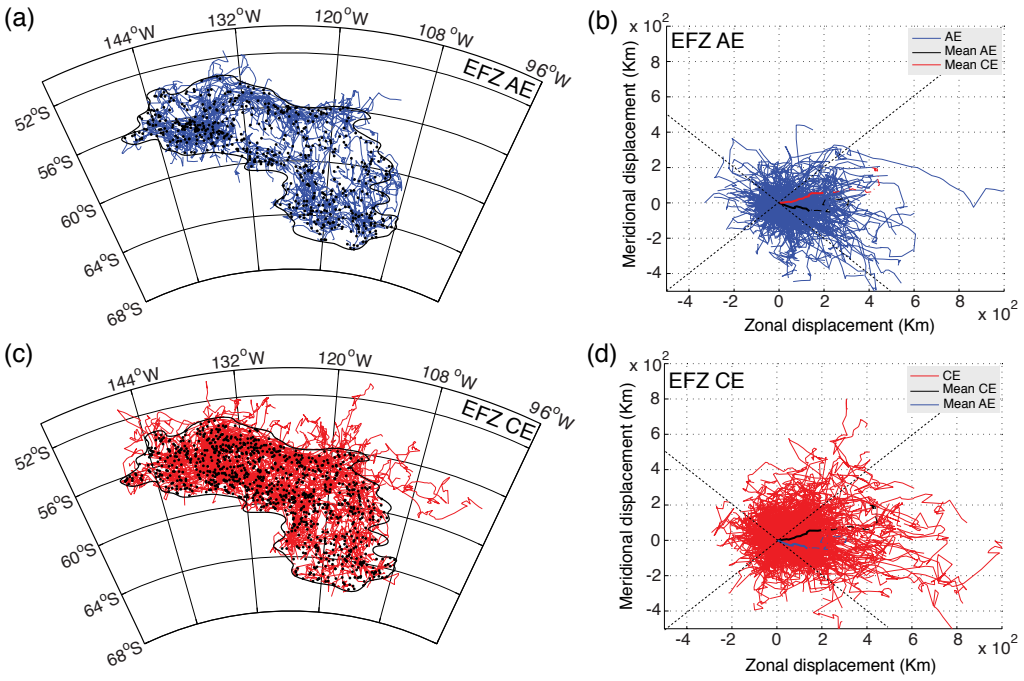

Figure 4.7: As in Fig. 4.5 but for Eltanin Fracture Zone site.

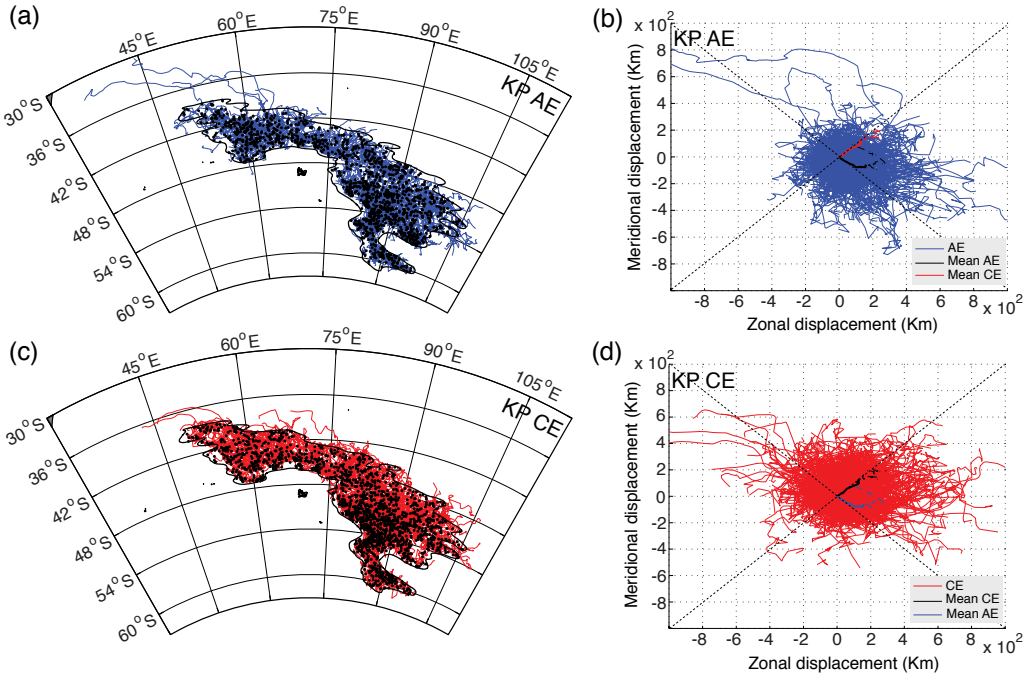

Figure 4.8: As in Fig. 4.5 but for Kerguelen Plateau site.

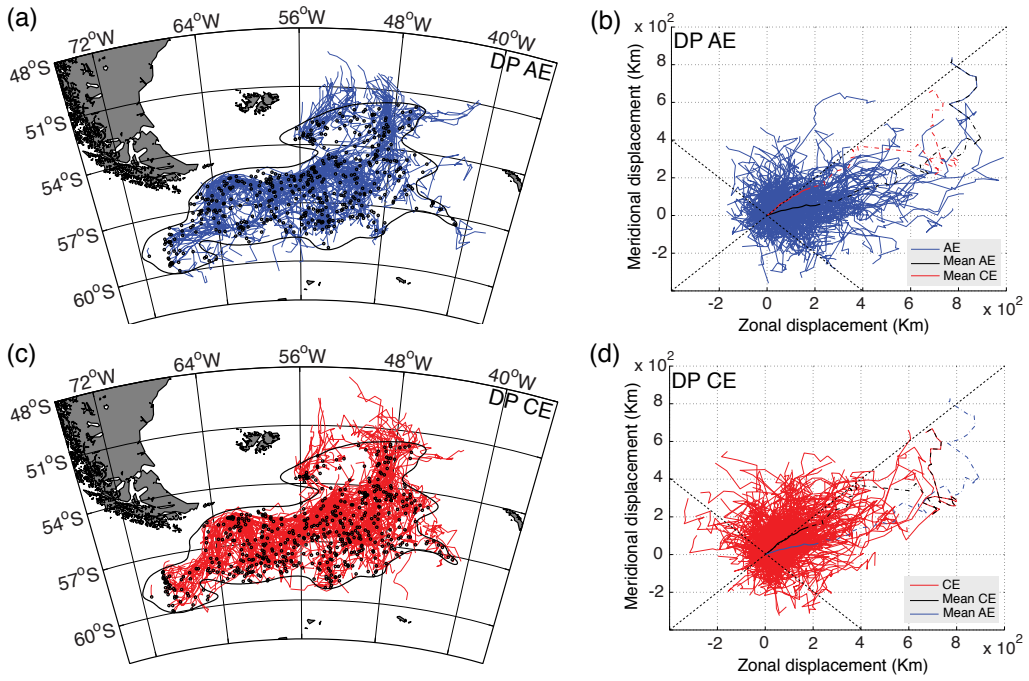

Figure 4.9: As in Fig. 4.5 but for Drake Passage site.

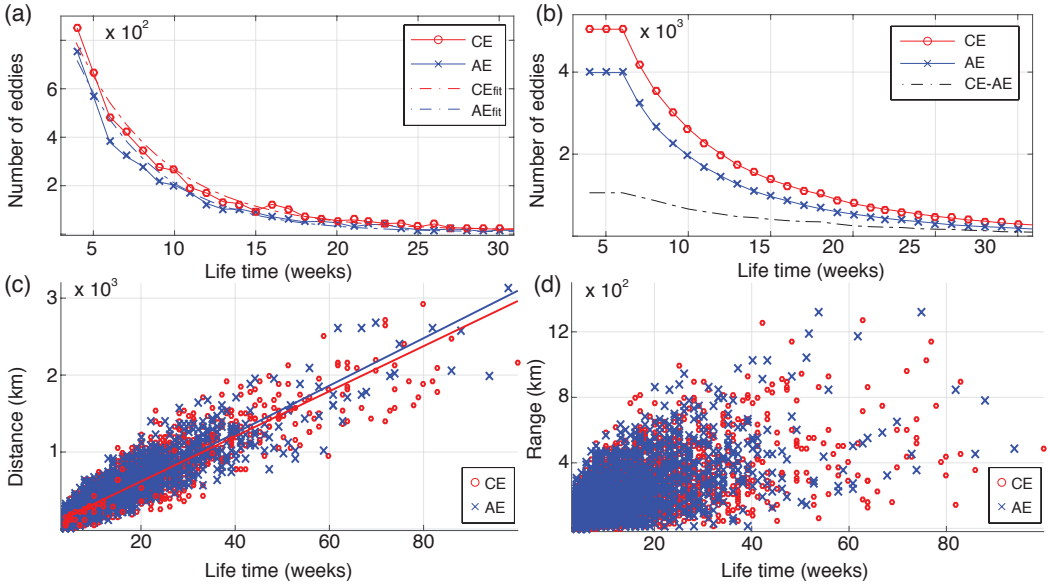

Figure 4.10: Average eddy statistics for all sites: (a) Histogram of number of eddies versus eddy life time. (b) Upper-tail cumulative histogram of number of eddies versus eddy life time. The difference between cyclonic eddies (CEs) and anticyclonic eddies (AEs) is indicated by the black dash-dot line. (c) Scatter plot of total distance covered versus eddy lifetime. Linear fits indicate the average speed for CEs (4.9 ± 0.1 cm s^{-1}) and AEs (5.1 ± 0.1 cm s^{-1}). (d) Scatter plot of distance between initial and final location versus eddy lifetime. In all cases red circles indicate CEs and blue crosses AEs.

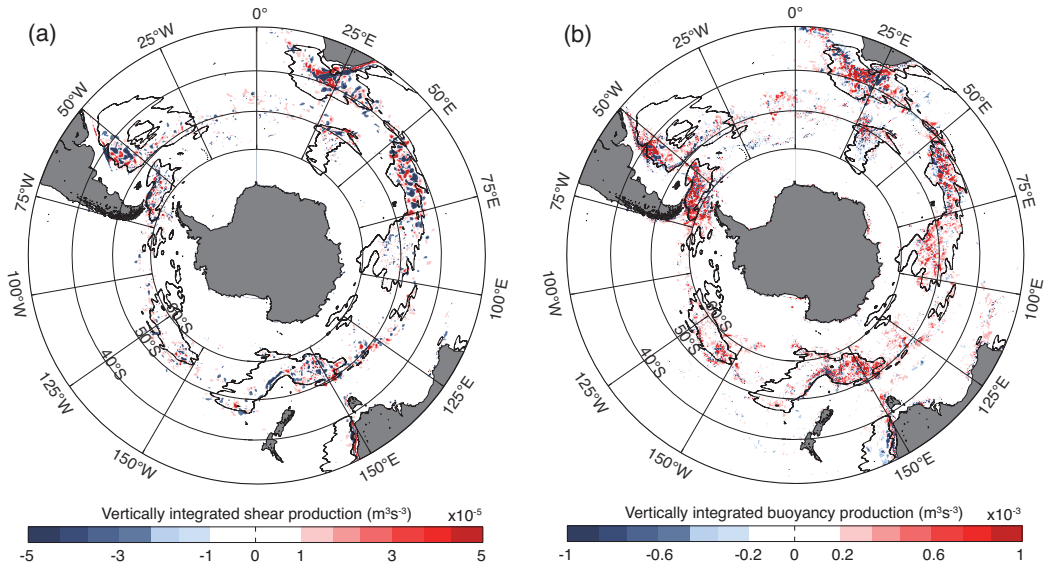

Figure 4.11: Vertically integrated shear production (a) and buoyancy production (b). Black contours denote isolines of equal probabilty of the multi-peak Gaussian kernel density function.

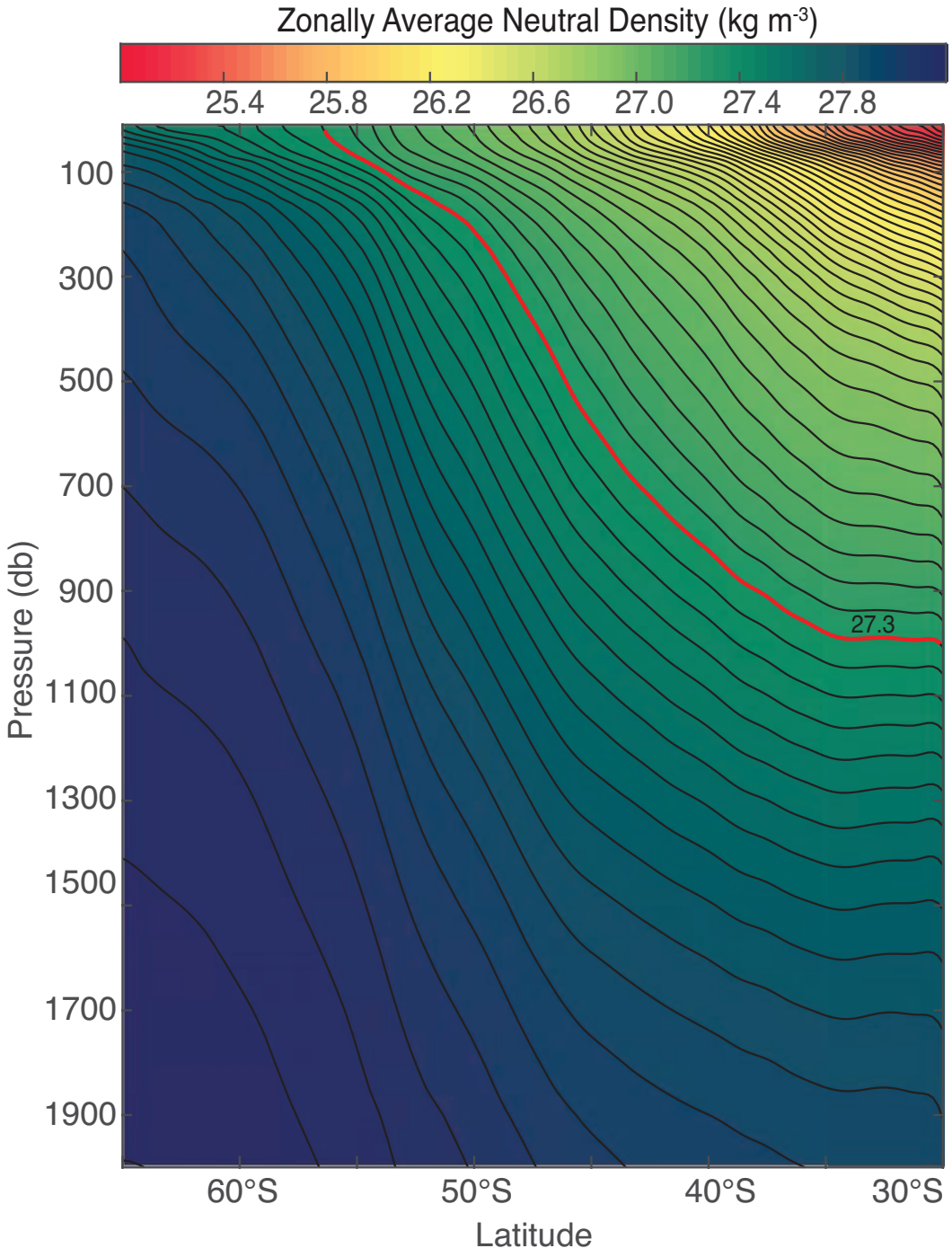

Figure 4.12: Zonally averaged meridional section of neutral density surfaces estimated from Argo floats. Only longitudes that cross the hotspots are used in the average.

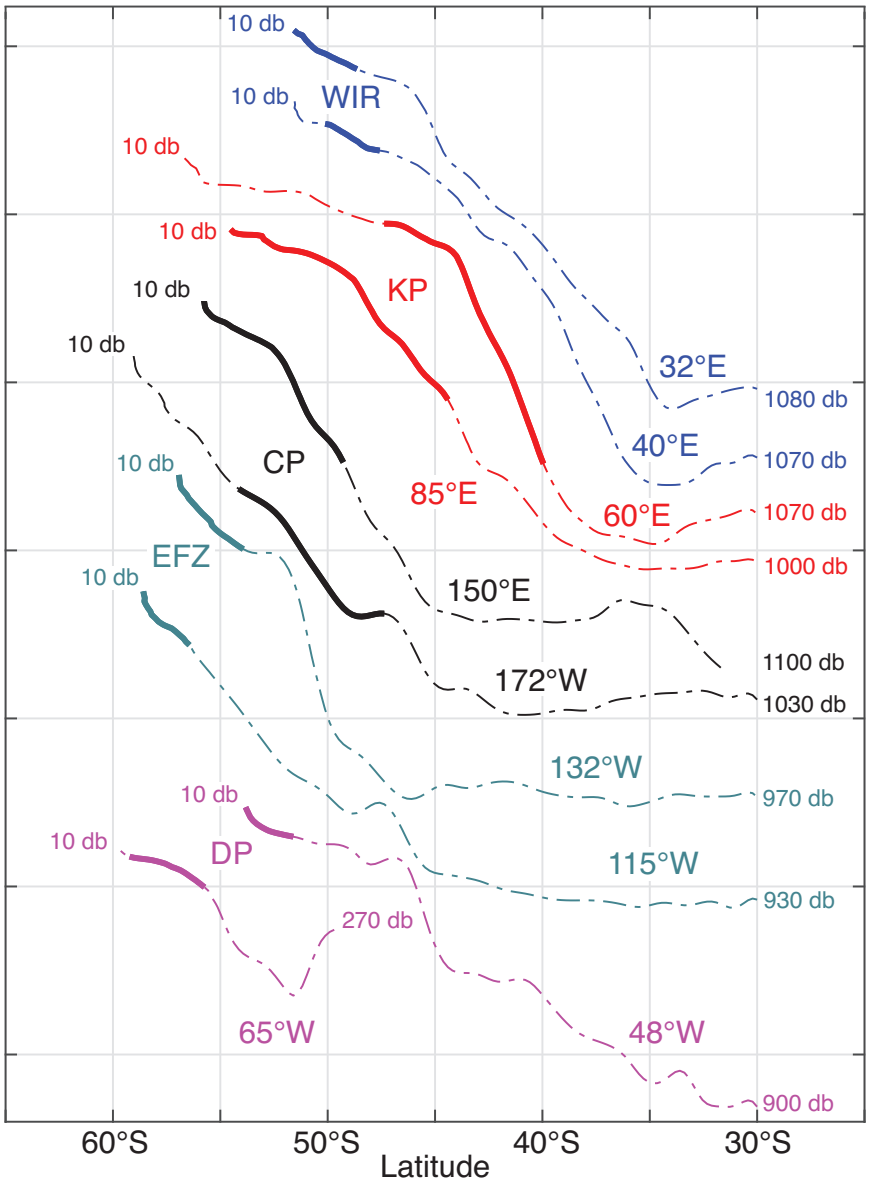

Figure 4.13: Meridional sections of the 27.3 kg m^{-3} neutral density surface (γ) at 10 different longitudes crossing the eddy generation hotspots. Neutral density surfaces are depicted as solid lines when they are within the boundaries of the corresponding hotspot, and as dashed-dot lines when are outside the hotspot. For clarity purposes sections are shifted in the vertical axis. Longitudes and pressure levels at the northern and southern end points are indicated for each section.

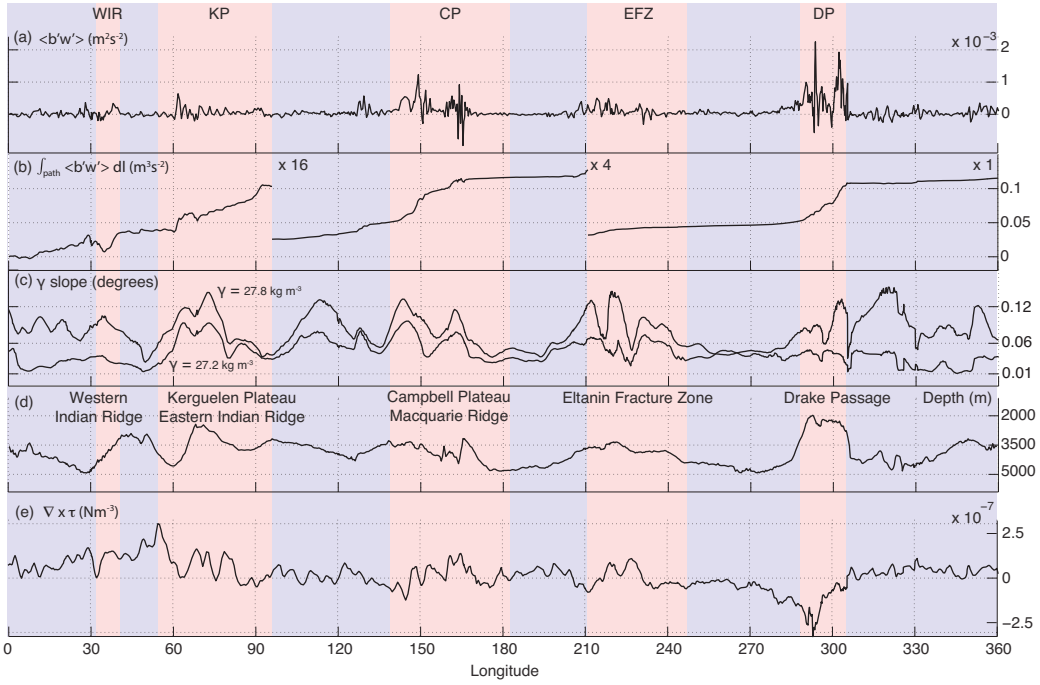

Figure 4.14: Circumpolar path of (a) Buoyancy production, (b) Accumulated buoyancy production, (c) Slope of 27.2 kg m^{-3} and 27.8 kg m^{-3} neutral density surfaces, (d) Water depth and (e) Wind stress curl. The boundaries of the circumpolar average are shown in Fig. 4.2 as dash-dot yellow lines. Red and blue areas denote when the circumpolar average is inside (red) or outside (blue) the eddy generation hotspots as defined by the kernel density function (KDE) in section 4.2 and shown in Fig. 4.2.

Chapter 5

Bibliography

Abernathey, R. and Cessi, P. (2014). Topographic enhancement of eddy efficiency in baroclinic equilibration. *J. Phys. Oceanogr.*, 44(8):2107–2126.

Abernathey, R., Marshall, J., Mazloff, M., and Shuckburgh, E. (2010). Enhancement of mesoscale eddy stirring at steering levels in the Southern Ocean. *J. Phys. Oceanogr.*, 40(1):170–184.

Aguilar, D. A. and Sutherland, B. R. (2006). Internal wave generation from rough topography. *Phys. Fluids*, 18(066603).

Armi, L. and Stommel, H. (1983). Four views of a portion of the North Atlantic subtropical gyre. *J. Phys. Oceanogr.*, 13:828–857.

Beron-Vera, F., Olascoaga, M., and Goni, G. (2008). Oceanic mesoscale eddies as revealed by Lagrangian coherent structures. *Geophys. Res. Lett.*, 35(12).

Beron-Vera, F. J., Wang, Y., Olascoaga, M. J., Goni, G. J., and Haller, G. (2013). Objective detection of oceanic eddies and the agulhas leakage. *J. Phys. Oceanogr.*, 43(7):1426–1438.

Boebel, O., Lutjeharms, J., Schmid, C., Zenk, W., Rossby, T., and Barron, C. (2003). The Cape Cauldron: a regime of turbulent inter-ocean exchange. *Deep-Sea Res. II*, 50(1):57–86.

Böning, C. W., Dispert, A., Visbeck, M., Rintoul, S. R., and Schwarzkopf, F. (2008). Response of the Antarctic Circumpolar Current to recent climate change. *Nature Geosci.*, 1:864–869.

Botev, Z. I., Grotowski, J. F., and Kroese, D. P. (2010). Kernel density estimation via diffusion. *Ann. Statist.*, 38(5):2916–2957.

Bremer, P.-T., Gruber, A., Bennett, J., Gyulassy, A., Kolla, H., Chen, J., and Grout, R. (2015). Identifying turbulent structures through topological segmentation. *Comm. App. Math. and Comp. Sci.*, 11(1):37–53.

Bretherton, F., Davis, R., and Frandry, C. B. (1976). A technique for objective analysis and design of oceanographic experiments applied to MODE-73. *Deep Sea Res.*, 23:559–582.

Cerovečki, I. and Mazloff, M. R. (2016). The Spatiotemporal Structure of Diabatic Processes Governing the Evolution of Subantarctic Mode Water in the Southern Ocean. *J. Phys. Oceanogr.*

Cerovečki, I., Talley, L. D., and Mazloff, M. R. (2011). A Comparison of Southern Ocean Air-Sea Buoyancy Flux from an Ocean State Estimate with Five Other Products. *J. Climate*, 24(24):6283–6306.

Chaigneau, A. and Pizarro, O. (2005). Eddy characteristics in the eastern South Pacific. *J. Geophys. Res. Oceans*, 110(C06005).

Chapman, D. C. and Haidvogel, D. B. (1993). Generation of internal lee waves trapped over a tall isolated seamount. *Geophysical & Astrophysical Fluid Dynamics*, 69:33–54.

Chassignet, E. P. and Cushman-Roisin, B. (1991). On the influence of a lower layer on the propagation of nonlinear oceanic eddies. *J. Phys. Oceanogr.*, 21(7):939–957.

Chelton, D. B. and Schlax, M. G. (1996). Global observations of oceanic Rossby waves. *Science*, 272(5259):234–238.

Chelton, D. B., Schlax, M. G., and Samelson, R. M. (2011). Global observations of nonlinear mesoscale eddies. *Prog. Oceanogr.*, 91(2):167 – 216.

Chelton, D. B., Schlax, M. G., Samelson, R. M., and de Szoeke, R. A. (2007). Global observations of large oceanic eddies. *Geophys. Res. Lett.*, 34:L15606.

Chen, C. and Kamenkovich, I. (2013). Effects of topography on baroclinic instability. *J. Phys. Oceanogr.*, 43(4):790–804.

Cormen, T. H., Leiserson, C. E., Rivest, R. L., and Stein, C. (2009). *Introduction to algorithms*. The MIT Press, 3rd edition.

Cubillos, J., Wright, S., Nash, G., Salas, M., Griffiths, B., B. Tilbrook, B., Poisson, A., and Hallegraeff, G. (2007). Calcification morpho types of the coccolithophorid Emiliania huxleyi in the Southern Ocean: changes in 2001 to 2006 compared to historical data. *Mar. Ecol. Prog. Ser.*, 248:47–54.

Cushman-Roisin, B., Tang, B., and Chassignet, E. P. (1990). Westward motion of mesoscale eddies. *J. Phys. Oceanogr.*, 20(5):758–768.

Davis, R. (1985). Objective mapping by least squares fitting. *J. Geophys. Res. Oceans*, 90(C3):4773–4777.

Davis, R. (1998). Preliminary results from directly measuring mid-depth circulation in the tropical and South Pacific. *J. Geophys. Res. Oceans*, 103:24619–24639.

Davis, R. E. (1991). Lagrangian ocean studies. *Annu. Rev. Fluid Mech.*, 23(1):43–64.

De Boor, C. (2001). *A practical guide to splines (Revised Edition)*, volume 27 of *Applied mathematical sciences*. Springer.

de Szoeke, R. A. and Levine, M. D. (1981). The advective flux of heat by mean geostrophic motions in the Southern Ocean. *Deep Sea Research Part A. Oceanographic Research Papers*, 28(10):1057 – 1085.

Dean, R. S. (1983). *The Radon Transform and some of its applications*. John Wiley and Sons.

Dewar, W. K. (1987). Ventilating Warm Rings: Theory and Energetics. *J. Phys. Oceanogr.*, 17(12):2219–2231.

Dong, S., Sprintall, J., and Gille, S. T. (2006). Location of the Antarctic Polar Front from AMSR-E Satellite Sea Surface Temperature Measurements. *J. Phys. Oceanogr.*, 36:2075–2089.

Donohue, K. A., Tracey, K. L., Watts, D. R., Chidichimo, M. P., and Chereskin, T. K. (2016). Mean Antarctic Circumpolar Current transport measured in Drake Passage. *Geophys. Res. Lett.*, 43(22):11,760–11,767. 2016GL070319.

Downes, S., Budnick, A. S., Sarmiento, J. L., and Farneti, R. (2011). Impacts of wind stress on the Antarctic Circumpolar Current fronts and associated subduction. *Geophys. Res. Lett.*, 38:L11605.

Draper, N. and Smith, H. (2006). *Applied regression analysis*. Wiley Series in Probability and Statistics. Wiley, 3 edition.

Ducet, N., Traon, P.-Y. L., and Reverdin, G. (2000). Global high resolution mapping of ocean circulation from TOPEX/Poseidon and ERS-1/2. *J. Geophys. Res. Oceans*, 105:19477–19498.

Duhaut, T. H. A. and Straub, D. N. (2006). Wind stress dependence on ocean surface velocity: Implications for mechanical energy input to ocean circulation. *J. Phys. Oceanogr.*, 36(2):202–211.

Early, J. J., Samelson, R. M., and Chelton, D. B. (2011). The evolution and propagation of quasigeostrophic ocean eddies. *J. Phys. Oceanogr.*, 41(8):1535–1555.

Feron, R. C., De Ruijter, W. P., and Oskam, D. (1992). Ring shedding in the Agulhas Current system. *J. Geophys. Res. Oceans*, 97(C6):9467–9477.

Ferrari, R. and Nikurashin, M. (2010). Suppression of eddy diffusivity across jets in the Southern Ocean. *J. Phys. Oceanogr.*, 40(7):1501–1519.

Firing, Y. L., Chereskin, T. K., and Mazloff, M. R. (2011). Vertical structure and transport of the Antarctic Circumpolar Current in Drake Passage from direct velocity observations. *J. Geophys. Res. Oceans*, 116(C8).

Flierl, G. R. (1984). Rossby wave radiation from a strongly nonlinear warm eddy. *J. Phys. Oceanogr.*, 14(1):47–58.

Frenger, I., Münnich, M., Gruber, N., and Knutti, R. (2015). Southern Ocean eddy phenomenology. *J. Geophys. Res. Oceans*, 120(11):7413–7449.

Frölicher, T. L., Sarmiento, J. L., Paynter, D. J., Dunne, J. P., Krasting, J. P., and Winton, M. (2015). Dominance of the Southern Ocean in anthropogenic carbon and heat uptake in CMIP5 models. *J. Climate*, 28(2):862–886.

Fu, L.-L. (2006). Pathways of eddies in the South Atlantic ocean revealed from satellite altimeter observations. *Geophys. Res. Lett.*, 33(14). L14610.

Fu, L.-L. (2009). Pattern and velocity of propagation of the global ocean eddy variability. *J. Geophys. Res. Oceans*, 114(C11).

Gandin, L. (1965). *Objective analysis of meteorological fields*. Israel Program for Scientific Publications.

Gill, A., Green, J., and Simmons, A. (1974). Energy partition in the large-scale ocean circulation and the production of mid-ocean eddies. *Deep-Sea Res.*, 21(7):499–528.

Gille, S. T. (2002). Warming of the Southern Ocean since the 1950s. *Science*, 295:1275–1277.

Gille, S. T. (2003a). Float Observations of the Southern Ocean. Part I: Estimating mean fields, bottom velocities, and topographic steering. *J. Phys. Oceanogr.*, 33:1167–1182.

Gille, S. T. (2003b). Float observations of the Southern Ocean. Part II: Eddy Fluxes. *J. Phys. Oceanogr.*, 33(6):1182–1196.

Gille, S. T. (2008). Decadal-scale temperature trends in the Southern Hemisphere Ocean. *J. Climate*, 21:4749–4765.

Gille, S. T. (2014). Meridional displacement of the Antarctic Circumpolar Current. *Phil. Trans. R. Soc. A*, 372:20130273.

Gille, S. T. and Kelly, K. A. (1996). Scales of spatial and temporal variability in the Southern Ocean. *J. Geophys. Res. Oceans*, 101(C4):8759–8773.

Gilson, J., Roemmich, D., Cornuelle, B., and Fu, L.-L. (1998). Relationship of TOPEX/Poseidon altimetric height to steric height and circulation in the North Pacific. *J. Geophys. Res. Oceans*, 103(C12):27947–27965.

Gordon, A., Molinelli, E., and Baker, T. (1978). Large-scale relative dynamic topography of the Southern Ocean. *J. Geophys. Res. Oceans*, 83(C6):3023–3032.

Gouretski, V. V. and Koltermann, K. P. (2004). WOCE global hydrographic climatology. Tech. rep. 35, Berichte des Bundesamt für Seeschifffart und Hydrographie, Hamburg und Rostock, Germany.

Graham, R. M., de Boer, A. M., Heywood, K. J., Chapman, M. R., and Stevens, D. P. (2012). Southern Ocean fronts: Controlled by wind or topography? *J. Geophys. Res. Oceans*, 117(C08018).

Hallberg, R. and Gnanadesikan, A. (2006). The role of eddies in determining the structure and response of the wind-driven southern hemisphere overturning: Results from the Modeling Eddies in the Southern Ocean (MESO) project. *J. Phys. Oceanogr.*, 36(12):2232–2252.

Haller, G. (2005). An objective definition of a vortex. *J. Fluid Mech.*, 525:1–26.

Haller, G. and Yuan, G. (2000). Lagrangian coherent structures and mixing in two-dimensional turbulence. *Physica D*, 147(3):352–370.

Hogg, A. M., Meredith, M. P., Chambers, D. P., Abrahamsen, E. P., Hughes, C. W., and Morrison, A. K. (2015). Recent trends in the Southern Ocean eddy field. *J. Geophys. Res. Oceans*, 120(1):257–267.

Hughes, C., Jones, M., and Carnochan, S. (1998). Use of transient features to identify eastward currents in the Southern Ocean. *J. Geophys. Res. Oceans*, 103(C2):2929–2943.

Hughes, C. W. and Wilson, C. (2008). Wind work on the geostrophic ocean circulation: An observational study of the effect of small scales in the wind stress. *J. Geophys. Res. Oceans*, 113(C2):n/a–n/a. C02016.

IOC, SCOR, and IAPSO (2010). *The international thermodynamic equation of seawater - 2010: Calculation and use of thermodynamic properties.*

Isern-Fontanet, J., García-Ladona, E., and Font, J. (2003). Identification of marine eddies from altimetric maps. *J. Atmos. Oceanic Technol.*, 20(5):772–778.

Ito, T., Woloszyn, M., and Mazloff, M. (2010). Anthropogenic carbon dioxide transport in the Southern Ocean driven by Ekman flow. *Nature*, 463(7277):80–83.

Ivchenko, V. and Richards, K. (1996). The dynamics of the Antarctic Circumpolar Current. *J. Phys. Oceanogr.*, 26:753–774.

Jackett, D. and McDougall, T. (1997). A Neutral Density Variable for the World's Oceans. *J. Phys. Oceanogr.*, 27:237–263.

Jacobs, S. S. (2006). Observations of change in the Southern Ocean. *Phil. Trans. R. Soc. A*, 364:1657–1681.

Keffer, T. and Holloway, G. (1988). Estimating Southern Ocean eddy flux of heat and salt from satellite altimetry. *Nature*, 332.

Killworth, P. and Hughes, C. (2002). The Antarctic Circumpolar Current as a free equivalent-barotropic jet. *J. Mar. Res.*, 60:19–45.

Klocker, A. and Abernathey, R. (2014). Global patterns of mesoscale eddy properties and diffusivities. *J. Phys. Oceanogr.*, 44(3):1030–1046.

Klocker, A., Ferrari, R., and LaCasce, J. H. (2012). Estimating suppression of eddy mixing by mean flows. *J. Phys. Oceanogr.*, 42(9):1566–1576.

Klocker, A. and Marshall, D. P. (2014). Advection of baroclinic eddies by depth mean flow. *Geophys. Res. Lett.*, 41(10):3517–3521.

Kundu, P., Cohen, I., and Dowling, D. R. (2012). *Fluid mechanics*. Elsevier Academic Press, 5th edition.

Lacasce, J. H. (2000). Floats and f/H. *J. Mar. Res.*, 58(1):61–95.

LaCasce, J. H. and Speer, K. G. (1999). Lagrangian statistics in unforced barotropic flows. *J. Mar. Res.*, 57(2):245–274.

Le Traon, P. (1990). A method for optimal analysis of fields with spatially variable mean. *J. Geophys. Res. Oceans*, 95(C8):13543–13547.

Le Traon, P. and Morrow, R. (2001). Ocean Currents and Eddies. In Fu, L. and Cazenave, A., editors, *Satellite Altimetry and Earth Sciences. A Handbook of Techniques and Applications*, volume 69 of *International Geophysics Series*, chapter 3, pages 171–xi. Associated Press.

Lecointre, A., Penduff, T., Cipollini, P., Tailleux, R., and Barnier, B. (2007). Depth dependence of westward-propagating North Atlantic features diagnosed from altimetry and a numerical 1/6° model. *Ocean Sci.*, 4(6):817–853.

Levitus, S., Antonov, J., and Boyer, T. (2005). Warming of the world ocean, 1955-2003. *Geophys. Res. Lett.*, 32(L02604).

Lu, J. and Speer, K. (2010). Topography, jets, and eddy mixing in the Southern Ocean. *J. Mar. Res.*, 68(3-4):479–502.

Lutjeharms, J. and Baker, D. (1980). A statistical analysis of the meso-scale dynamics of the Southern Ocean. *Deep-Sea Res.*, 27A(2):145 – 159.

Marinov, I., Gnanadesikan, A., Toggweiler, J. R., and Sarmiento, J. L. (2006). The Southern Ocean biogeochemical divide. *Nature*, 441(7096):964–967.

Marshall, G. J. (2003). Trends in the Southern Annular Mode from observations and reanalyses. *J. Climate*, 16:4134–4143.

Marshall, J. and Plumb, A. (2008). *Atmosphere, Ocean and Climate Dynamics: An Introductory Text*, volume 93 of *International Geophysics Series*. Elsevier, 1st edition.

Marshall, J. and Radko, T. (2003). Residual-mean solutions for the Antarctic Circumpolar Current and its associated overturning circulation. *J. Phys. Oceanogr.*, 33(11):2341–2354.

Marshall, J. and Speer, K. (2012). Closure of the meridional overturning circulation through Southern Ocean upwelling. *Nature Geosci.*, 5(3):171–180.

Masich, J., Chereskin, T. K., and Mazloff, M. R. (2015). Topographic form stress in the Southern Ocean State Estimate. *J. Geophys. Res. Oceans*, 120(12):7919–7933.

Mazloff, M., Heimbach, P., and Wunsch, C. (2010). An Eddy-Permitting Southern Ocean State Estimate. *J. Phys. Oceanogr.*, 40:880–899.

McWilliams, J. C. and Flierl, G. R. (1979). On the evolution of isolated, nonlinear vortices. *J. Phys. Oceanogr.*, 9(6):1155–1182.

Meijers, A. J. S., Bindoff, N. L., and Rintoul, S. R. (2011a). Estimating the four-fimensional structure of the Southern Ocean using satellite altimetry. *J. Atmos. Oceanic Technol.*, 28:548–568.

Meijers, A. J. S., Bindoff, N. L., and Rintoul, S. R. (2011b). Frontal movements and property fluxes: Contributions to heat and freshwater trends in the Southern Ocean. *J. Geophys. Res. Oceans*, 116(C08024).

Meredith, M. P. and Hogg, A. M. (2006). Circumpolar response of Southern Ocean eddy activity to a change in the Southern Annular Mode. *Geophys. Res. Lett.*, 33:L16608.

Morrow, R., Birol, F., Griffin, D., and Sudre, J. (2004a). Divergent pathways of cyclonic and anti-cyclonic ocean eddies. *Geophys. Res. Lett.*, 31(24).

Morrow, R., Donguy, J.-R., Chaigneau, A., and Rintoul, S. R. (2004b). Cold-core anomalies at the subantarctic front, south of Tasmania. *Deep-Sea Res. I*, 51(11):1417–1440.

Morrow, R., Ward, M. L., Hogg, A. M., and Pasquet, S. (2010). Eddy response to Southern Ocean climate modes. *J. Geophys. Res. Oceans*, 115(C10). C10030.

Munk, W. H. and Palmén, E. (1951). Note on the dynamics of the Antarctic Circumpolar Current. *Tellus*, 3(1):53–55.

Naveira Garabato, A., Polzin, K. L., King, B. A., Heywood, K. J., and Visbeck, M. (2004). Widespread intense turbulent mixing in the Southern Ocean. *Science*, 303:210–213.

Nikurashin, M. and Vallis, G. (2011). A theory of deep stratification and overturning circulation in the ocean. *J. Phys. Oceanogr.*, 41(3):485–502.

Nikurashin, M. and Vallis, G. (2012). A theory of the interhemispheric meridional overturning circulation and associated stratification. *J. Phys. Oceanogr.*, 42(10):1652–1667.

Nof, D. (1983). On the migration of isolated eddies with application to Gulf Stream rings. *J. Mar. Res.*, 41(3):399–425.

Nowlin, W. D. and Klinck, J. M. (1986). The physics of the Antarctic Circumpolar Current. *Rev. Geophys.*, 24(3):469–491.

Olbers, D. and Visbeck, M. (2005). A model of the zonally averaged stratification and overturning in the Southern Ocean. *J. Phys. Oceanogr.*, 35(7):1190–1205.

Orsi, A., III, T. W., and Jr., W. N. (1995). On the meridional extent and fronts of the Antarctic Circumpolar Current. *Deep-Sea Res. I*, 42(5):641–673.

Pascual, A., Faugère, Y., Larnicol, G., and Traon, P. Y. L. (2006). Improved description of the ocean mesoscale variability by combining four satellite altimeters. *Geophys. Res. Lett.*, 33(L02611).

Phillips, H. and Rintoul, S. (2000). Eddy variability and energetics from direct current measurements in the Antarctic Circumpolar Current south of Australia. *J. Phys. Oceanogr.*, 30:3050–3076.

Phillips, H. E. and Bindoff, N. L. (2014). On the nonequivalent barotropic structure of the Antarctic Circumpolar Current: An observational perspective. *J. Geophys. Res. Oceans*, 119(8):5221–5243.

Pingree, R. and Sinha, B. (2001). Westward moving waves or eddies (storms) on the subtropical/Azores front near 32.5°N? interpretation of the Eulerian currents and temperature records at moorings 155 (35.5°W) and 156 (34.4°W). *J. Mar. Sys.*, 29(1):239–276.

Polito, P. S. and Cornillon, P. (1997). Long baroclinic Rossby waves detected by TOPEX/POSEIDON. *J. Geophys. Res. Oceans*, 102(C2):3215–3235.

Purkey, S. G. and Johnson, G. C. (2010). Warming of global abyssal and deep Southern Ocean waters between the 1990s and 2000s: Contributions to global heat and sea level rise budgets. *J. Climate*, 23:6336–6351.

Qiu, B. and Chen, S. (2004). Seasonal modulations in the eddy field of the South Pacific Ocean. *J. Phys. Oceanogr.*, 34(7):1515–1527.

Radon, J. (1917). Über die bestimmung von funktionen durch ihre integralwertel längs gewisser mannigfaltigkeiten. *Ber. Sächsische Akad der Wissenschaften*, 69:262–267.

Richardson, P. L. (1981). Gulf stream trajectories measured with free-drifting buoys. *J. Phys. Oceanogr.*, 11(7):999–1010.

Ridgway, K., Dunn, J., and Wilkin, J. (2002). Ocean interpolation by four-dimensional weighted least squares - Application to the waters around Australasia. *J. Atmos. Oceanic Technol.*, 19(9):1357–1375.

Roemmich, D., Belbéoch, M., Freeland, H., Garzoli, S., Gould, W. J., Grant, F., Ignaszewski, M., King, B., Klein, B., Traon, P. L., Mork, K. A., Owens, W. B., Pouliquen, S., Ravichandran, M., Sterl, A., Suga, T., Suk, M., Sutton, P., V.Thierry, Vélez-Belchí, P. J., Wijffels, S., and Xu, J. (2009). Argo: The challenge of continuing 10 years of progress. *Oceanography*, 22(3):26–35.

Roemmich, D. and Gilson, J. (2009). The 2004-2008 mean and annual cycle of temperature, salinity, and steric height in the global ocean from the argo program. *Prog. Oceanogr.*, 82(2):81 – 100.

Rossby, H., Riser, S., and Mariano, A. (1983). The western North Atlantic – A Lagrangian viewpoint. In Robinson, A. R., editor, *Eddies in Marine Science*, Topics in Atmospheric and Oceanographic Sciences, chapter 4, pages 66–91. Springer.

Rudnick, D. L. and Martin, J. (2002). On the horizontal density ratio in the upper ocean. *Dyn. Atmos. Oceans*, 36:3–21.

Samelson, R. (1992). Fluid exchange across a meandering jet. *J. Phys. Oceanogr.*, 22:431–440.

Saraceno, M. and Provost, C. (2012). On eddy polarity distribution in the south-western atlantic. *Deep-Sea Res. I*, 69:62 – 69.

Sciremammano, F. (1980). The nature of the poleward heat flux due to low-frequency current fluctuations in Drake Passage. *J. Phys. Oceanogr.*, 10(6):843–852.

Screen, J. A., Gillett, N. P., Stevens, D. P., Marshall, G. J., and Roscoe, H. K. (2009). The role of eddies in the Southern Ocean temperature response to the Southern Annular Mode. *J. Climate*, 22(3):806–818.

Siedler, G., Griffies, S. M., Gould, W. J., and Church, J., editors (2013). *Ocean circulation and climate: A 21st century perspective*. Amsterdam: Academic Press, 2nd edition.

Simonoff, J. S. (1996). *Smoothing methods in statistics*. Springer Series in Statistics. Springer-Verlag, New York.

Sloyan, B. M. and Rintoul, S. R. (2000). Estimates of area-averaged diapycnal fluxes from basin-scale budgets. *J. Phys. Oceanogr.*, 30(9):2320–2341.

Sloyan, B. M., Talley, L. D., Chereskin, T. K., Fine, R., and Holte, J. (2010). Antarctic Intermediate Water and Subantarctic Mode Water formation in the Southeast Pacific: The role of turbulent mixing. *J. Phys. Oceanogr.*, 40:1558–1574.

Smith, W. H. F. and Sandwell, D. T. (1997). Global sea floor topography from satellite altimetry and ship depth soundings. *Science*, 277(5334):1956–1962.

Sokolov, S. and Rintoul, S. R. (2007). On the relationship between fronts of the Antarctic Circumpolar Current and surface chlorophyll concentrations in the Southern Ocean. *J. Geophys. Res. Oceans*, 112(C7).

Sokolov, S. and Rintoul, S. R. (2009a). Circumpolar structure and distribution of the Antarctic Circumpolar Current fronts: 1. Mean circumpolar paths. *J. Geophys. Res. Oceans*, 114(C11018).

Sokolov, S. and Rintoul, S. R. (2009b). Circumpolar structure and distribution of the Antarctic Circumpolar Current fronts: 2. Variability and relationship to sea surface height. *J. Geophys. Res. Oceans*, 114(C11019).

Ssalto/Duacs (2011). Ssalto/Duacs user handbook: (M)SLA and (M)ADT near-real time and delayed time products. techreport 2rev6, CNES.

St. Laurent, L., Naveira Garabato, A. C., Ledwell, J. R., Thurnherr, A. M., Toole, J. M., and Watson, A. J. (2012). Turbulence and diapycnal mixing in Drake Passage. *J. Phys. Oceanogr.*, 42(12):2143–2152.

Stammer, D. (1998). On eddy characteristics, eddy transports, and mean flow properties. *J. Phys. Oceanogr.*, 28(4):727–739.

Talley, L. (2008). Freshwater transport estimates and the global overturning circulation: Shallow, deep and throughflow components. *Prog. Oceanogr.*, 78:257–303.

Thompson, A. F. (2008). The atmospheric ocean: eddies and jets in the Antarctic Circumpolar Current. *Phil. Trans. R. Soc. A*, 366(1885):4529–4541.

Thompson, A. F. and Garabato, A. C. N. (2014). Equilibration of the Antarctic Circumpolar Current by Standing Meanders. *J. Phys. Oceanogr.*, 44(7):1811–1828.

Thompson, A. F. and Richards, K. J. (2011). Low frequency variability of Southern Ocean jets. *J. Geophys. Res. Oceans*, 116(C9):n/a–n/a. C09022.

Thompson, A. F. and Salle, J.-B. (2012). Jets and Topography: Jet Transitions and the Impact on Transport in the Antarctic Circumpolar Current. *J. Phys. Oceanogr.*, 42(6):956–972.

Toggweiler, J. and Samuels, B. (1995). Effect of Drake Passage on the global thermohaline circulation. *Deep-Sea Res. I*, 42(4):477–500.

Treguier, A. M., England, M. H., Rintoul, S. R., Madec, G., Le Sommer, J., and Molines, J.-M. (2007). Southern Ocean overturning across streamlines in an eddying simulation of the Antarctic Circumpolar Current. *Ocean Sci.*, 3(4):491–507.

Treguier, A. M. and McWilliams, J. C. (1990). Topographic Influences on Wind-Driven, Stratified Flow in a β-Plane Channel: An Idealized Model for the Antarctic Circumpolar Current. *J. Phys. Oceanogr.*, 20(3):321–343.

Tulloch, R., Marshall, J., Hill, C., and Smith, K. S. (2011). Scales, growth rates, and spectral fluxes of baroclinic instability in the ocean. *J. Phys. Oceanogr.*, 41(6):1057–1076.

Vallis, G. K. (2006). *Atmospheric and oceanic fluid dynamics: fundamentals and large-scale circulation*. Cambridge University Press.

Volkov, D. L., Fu, L.-L., and Lee, T. (2010). Mechanisms of the meridional heat transport in the Southern Ocean. *Ocean Dyn.*, 60(4):791–801.

Whalen, C. B., Talley, L. D., and MacKinnon, J. A. (2012). Spatial and temporal variability of global ocean mixing inferred from Argo profiles. *Geophys. Res. Lett.*, 39(L18612).

Willis, J. K. and Fu, L.-L. (2008). Combining altimeter and subsurface float data to estimate the time-averaged circulation in the upper ocean. *J. Geophys. Res. Oceans*, 113(C12). C12017.

Willis, J. K., Roemmich, D., and Cornuelle, B. (2004). Interannual variability in upper ocean heat content, temperature, and thermosteric expansion on global scales. *J. Geophys. Res. Oceans*, 109:C12036.

Wong, A., Keeley, R., Carval, T., and The Argo Data Management Team (2015). Argo Quality Control Manual for CTD and Trajectory Data. techreport.

Wright, D. G. (1981). Baroclinic Instability in Drake Passage. *J. Phys. Oceanogr.*, 11(2):231–246.

Wunsch, C. (2013). Baroclinic motions and energetics as measured by altimeters. *J. Atmos. Oceanic Technol.*, 30(1):140–150.

Xu, C., Shang, X.-D., and Huang, R. X. (2014). Horizontal eddy energy flux in the world oceans diagnosed from altimetry data. *Scientific Reports*, 4.

Xu, C., Zhai, X., and Shang, X.-D. (2016). Work done by atmospheric winds on mesoscale ocean eddies. *Geophys. Res. Lett.*, 43(23):12,174–12,180. 2016GL071275.

Zajaczkovski, U. (2017). *A study of the Southern Ocean: Mean state, eddy genesis & demise, and energy pathways*. PhD thesis, University of California San Diego.

Zlotnicki, V., Fu, L.-L., and Patzert, W. (1989). Seasonal Variability in Global Sea Level Observed With Geosat Altimetry. *J. Geophys. Res. Oceans*, 94(C12):17959–17969.